Title
Non-contact biopotential sensing

Permalink
https://escholarship.org/uc/item/4z4898fb

Author
Chi, Yu Mike

Publication Date
2011

Peer reviewed|Thesis/dissertation

UNIVERSITY OF CALIFORNIA, SAN DIEGO

Non-contact Biopotential Sensing

A dissertation submitted in partial satisfaction of the
requirements for the degree
Doctor of Philosophy

in

Electrical Engineering (Electronic Circuits and Systems)

by

Yu Mike Chi

Committee in charge:

Professor Gert Cauwenberghs, Chair
Professor Peter Asbeck
Professor Lawrence Larson
Professor Eduardo Macagno
Professor Ramesh Rao

2011

The dissertation of Yu Mike Chi is approved, and it is acceptable in quality and form for publication on microfilm and electronically:

Chair

University of California, San Diego

2011

DEDICATION

Dedicated to my parents: Lei Chi and Hong Xiao. My younger brothers: David Chi, Benjamin Chi and little Eugene Chi. And to my other half: Yuchen Cao.

EPIGRAPH

Remember there are no shortcuts, son. Quick buck artists come and go with every bull market, but the steady players make it through the bear market. You're a part of something here, Bud. The money you make for people creates science and research jobs. Don't sell that out.

—Wall Street, 1987

TABLE OF CONTENTS

LIST OF FIGURES

LIST OF TABLES

ACKNOWLEDGEMENTS

No effort stands alone, not even one as personally involved as Ph.D. thesis. This work would have never been possible without the help of so many people and I am perpetually in their debt.

This work is the result of years of ceaseless support from my advisor, Professor Gert Cauwenberghs. It was Gert that recognized and pushed me to achieve my full potential, and none of these accomplishments were possible without his guidance. I could not have asked for a better thesis advisor. It has been a long way since 520.492 class at Johns Hopkins.

I also thank my thesis committee, Professor Peter Asbeck, Professor Ramesh Rao and Professor Lawrence Larson for their patience and constructive advice during the exams. A special thanks is owed to Professor Eduardo for his support and encouragement in my studies. His vision of applying mobile technology towards healthcare is something that personally inspires me and I sincerely hope that I am able to contribute towards that goal.

Without the rest of the Cauwenberghs lab, my grad school years would have been undoubtedly much lonelier. Thanks to Teddy Yu, Steve Deiss, Siddharth Joshi, Jongkil Park, Dr, Fredreic Broccard, Dr. Massoud Khraiche and Sohmyun Ha, there was rarely a dull moment whenever I stepped into Room 306. Special thanks to Dr. Christoph Maier who helped me immensely with the details of IC design and engineering in general. Starting from the quiet days in Bonner Hall, this was a great lab to be a part of. I also must thank the rest of the people I've had a chance to work with here in San Diego: Patrick Ng, Kevin Liu, Neil Gandhi, Charles Khe, Kevin Young and my long-time friend, Stephen Chen.

Validating the sensors for EEG/BCI would not have been possible without the help from Dr. Tzyy-Ping Jung, Dr. Yijun Wang and Yu-Te Wang. They gave me the critical support in validating the performance of the sensors and I thank their patience during the extensive experiments. I am glad to have the opportunity to collaborate with them.

It was an honor working with Lelin Zhang, Dr. Eve Edelstein, Dr. Jurgen Schulze, Dr. Klaus Gramann and Cory Stevenson. I wish the best of successes to the ongoing projects and hope that I may still be able to support it.

I would also like to thank Prof. Patrick Chiang, Joe Crop and everyone else from OSU that worked with Christoph and me on the wireless sensor project. I wish the best of success to our ongoing efforts.

I owe a special debt of gratitude to Prof. Ralph Etienne-Cummings, who took me, then a clueless sophomore at Johns Hopkins, into his charge and gave me a chance to succeed in the academic world. None of this would have been possible without the support I received from Matt Clapp, Ralf Philipp, Dimitri Loizos, Prof. Paul Sotiriadis, Beatriz Olleta and everyone else at Hopkins who taught me so much about research and engineering. I remember countless days and nights spent at Stieff hall soldering, programming or testing circuit boards. Sunny skies of La Jolla aside, the time spent at his lab during my undergraduate years were some of the best in my life.

This work would not have been possible without the generous support from the National Science Foundation, National Semiconductor, the US Army Telemedicine and Advanced Technology Research Center (TATRC), the UCSD Institute of Engineering in Medicine and CalIT^2.

I owe my family the greatest thanks of all. I remember the first Radioshack 30-in-1 electronics kit (quickly replaced with the 300-in-1) that my father bought for me. Tinkering with LEDs, noise makers and crystal radios was the best education in electrical engineering that I could ever hope for. The prototyping, troubleshooting and circuit design skills developed when I was 10 years old gave me an immense advantage later on in life. If my father developed my love of electronics, then my mother was responsible for developing my love of science. She helped me with all those early science fair projects, testing soaps and growing bacteria, leading to a few elementary school awards. It was their ceaseless hard work for my brothers and myself that made my education possible. And last, but most certainly not least, I owe my success to Yuchen Cao. Without her support day and night, I could not have completed this degree.

Chapter One is largely a reprint of material that appeared in the 2010 IEEE Reviews of Biomedical Engineering Paper: Y. M. Chi, Tzyy-Ping Jung and Gert Cauwenberghs, “Dry and Non-contact Biopotential Electrodes,” *IEEE Reviews in Biomedical Engineering*, 2010. The author was the primary author and investigator of this work.

Chapter Two is largely a reprint of material published in the 2011 IEEE Body Sensor Networks Conference: N. Gandhi, C. Khe, D. Chung, Y. M. Chi and G. Cauwenberghs, “Properties of Dry and Non-contact Electrodes for Body Sensor Networks,” *IEEE Body Sensor Networks*, 2011. The author is the primary author and investigator of this work.

Chapter Three is largely a reprint of the 2009 IEEE Body Sensor Networks paper: Y. M. Chi, S. R. Deiss, and G. Cauwenberghs, “Non-contact Low Power EEG/ECG Electrode for High Density Wearable Biopotential Sensor Networks,” *IEEE Body Sensor Networks*, 2009. The author was the primary author and investigator of this work.

Chapter Four is largely a reprint of material submitted to the ACM Transactions on Embedded Computing Systems: Y. M. Chi, P. Ng and G. Cauwenberghs, “Wireless Non-contact ECG and EEG Biopotential Sensors,” *ACM Transactions on Embedded Computing Systems*, (submitted). The author was the primary author and investigator of this work.

Chapter Five is an amalgamation of material submitted to the 2011 IEEE Circuits and Systems - Forum on Emerging and Selected Topics Workshop and the IEEE 2011 IEEE European Solid-State Circuits Conference plus significant additional text. Y. M. Chi, C. Maier and G. Cauwenberghs, “Integrated Ultra-High Impedance Front-end for Non-contact Biopotential Sensing,” *IEEE European Solid State Circuits Conference* (Submitted). Y. M. Chi, C. Maier and G. Cauwenberghs, “An Integrated, Low-noise, High-Input Impedance Front-end for Capacitive Non-contact Physiological and BCI Sensor Systems,” *IEEE Circuits and Systems-Forum on Emerging and Selected Topics*, May 2011. The author is the primary author and investigator of this work.

Chapter Six is an expansion of material published in the 2010 IEEE European Solid-State Circuits Conference: Y. M. Chi and G. Cauwenberghs, “Auto-ranging Incremental Delta Sigma ADC,” *IEEE European Solid State Circuits Conference*, September 2010. The author is the primary author and investigator of this work.

Chapter Seven is largely a reprint of material published in the 2010 IEEE Engineering in Medicine and Biology Conference: L. Zhang, Y.M. Chi, E. Edelstein, J. Schulze, K. Gramann, A. Velasquez, G. Cauwenberghs, and E. Macagno, “Wireless Physiological Monitoring and Ocular Tracking: 3D Calibration in a Fully-Immersive

Virtual Health Care Environment," *IEEE Int. Engineering in Medicine and Biology Conference*, 2010. The author is one of the primary investigators of this work.

Chapter Eight is largely a reprint of material submitted to the IEEE Transactions on Neural Systems and Rehabilitation Engineering Journal. The author is the primary author and investigator of this work. Y. M. Chi, Y.T. Wang, Y. Wang, C. Maier, T.P. Jung and G. Cauwenberghs, "Dry and Non-contact EEG Sensors for Mobile Brain-Computer Interfaces," *IEEE Transactions on Neural Systems and Rehabilitation Engineering* (Submitted).

Appendix A is largely a reprint of material published in the 2009 Public Library of Science PLoS One Journal: Y. M. Chi, R. Etienne-Cummings and G. Cauwenberghs, "Focal-Plane Change Triggered Video Compression for Low-Power Vision Sensor Systems," *PLoS One*, 2009. The author was the primary author and investigator of this work.

Appendix B is largely a reprint of material published in the 2010 IEEE International Symposium on Circuits and Systems Conference: Y. M. Chi, G. Carhart, M.A. Voronstov and G. Cauwenberghs, "Intensity Histogram Imager for Adaptive Optics," *IEEE International Symposium on Circuits and Systems*, 2010. The author was the primary author and investigator of this work.

VITA AND PUBLICATIONS

2004-2007	Undergraduate Research Assistant, The Johns Hopkins University
2007	B. S. in Electrical Engineering, The Johns Hopkins University
2007-2011	Graduate Research Assistant, University of California, San Diego
2009	M. S. in Electrical Engineering, University of California, San Diego
2010	Founder and Chief Technology Officer, Cognionics, Inc.
2011	Ph. D. in Electrical Engineering, University of California, San Diego

Y. M. Chi, U. Mallik, M. A. Clapp, E. Choi, G. Cauwenberghs and R. Etienne-Cummings, "CMOS Pixel ADC with Change Detection," *IEEE International Symposium on Circuits and Systems*, 2006

Y. M. Chi, P. Carpenter, K. Colling, G. Cauwenberghs and R. Etienne-Cummings, "Video Sensor Node for Ad-hoc Wireless Networks," *IEEE Conference on Information Sciences and Systems*, 2007

Y. M. Chi, U. Mallik, M. A. Clapp, E. Choi, G. Cauwenberghs and R. Etienne-Cummings, "CMOS Pixel ADC with Change Detection," *IEEE Journal of Solid State Circuits*, Oct. 2007

Y. M. Chi, T. Tran and R. Etienne-Cummings, "Optical Flow Approximation of Sub-Pixel Accurate Block Matching for Video Coding," *IEEE International Conference on Acoustics, Speech and Signal Processing*, 2007

Y. M. Chi, R. Etienne-Cummings, G. Cauwenberghs, "Image Sensor with Focal Plane Change Event Driven Video Compression," *IEEE International Symposium on Circuits and Systems*, 2008

Y. M. Chi, A. Abbas, S. Chakrabartty, and G. Cauwenberghs, "An Active Pixel CMOS Separable Transform Image Sensor," *IEEE International Symposium on Circuits and Systems*, 2009

Y. M. Chi, S. R. Deiss, and G. Cauwenberghs, "Non-contact Low Power EEG/ECG Electrode for High Density Wearable Biopotential Sensor Networks," *IEEE Body Sensor Networks*, 2009

Y. M. Chi and G. Cauwenberghs, “Micropower Non-contact EEG Electrode with Active Common-Mode Noise Suppression and Input Capacitance Cancellation,” *IEEE Engineering in Medicine and Biology Conference*, 2009

Y. M. Chi, G. Carhart, M.A. Voronstov and G. Cauwenberghs, “Intensity Histogram Imager for Adaptive Optics,” *IEEE International Symposium on Circuits and Systems*, 2010

Y. M. Chi and G. Cauwenberghs, “Wireless Non-contact Biopotential Electrode,” *IEEE Body Sensor Networks*, June, 2010

Y. M. Chi and G. Cauwenberghs, “Auto-ranging Incremental Delta Sigma ADC,” *IEEE European Solid State Circuits Conference*, September 2010

L. Zhang, Y.M. Chi, E. Edelstein, J. Schulze, K. Gramann, A. Velasquez, G. Cauwenberghs, and E. Macagno, “Wireless Physiological Monitoring and Ocular Tracking: 3D Calibration in a Fully-Immersive Virtual Health Care Environment,” *IEEE Int. Engineering in Medicine and Biology Conference*, 2010.

Y. M. Chi, E. Kang, J. Kang, J. Fang and G. Cauwenberghs, “Wireless Non-contact Cardiac and Brain Monitoring,” *Wireless Health Conference*, 2010

Y. M. Chi, Tzyy-Ping Jung and Gert Cauwenberghs, “Dry and Non-contact Biopotential Electrodes,” *IEEE Reviews in Biomedical Engineering*, 2010

N. Gandhi, C. Khe, D. Chung, Y. M. Chi and G. Cauwenberghs, “Properties of Dry and Non-contact Electrodes for Body Sensor Networks,” *IEEE Body Sensor Networks*, 2011

Y. M. Chi, Christoph Maier and Gert Cauwenberghs, “An Integrated, Low-noise, High-Input Impedance Front-end for Non-contact BCI and BSN Physiological Monitoring Systems,” *IEEE Circuits and Systems - Forum on Emerging and Selected Topics*, 2011

ABSTRACT OF THE DISSERTATION

Non-contact Biopotential Sensing

by

Yu Mike Chi

Doctor of Philosophy in Electrical Engineering (Electronic Circuits and Systems)

University of California, San Diego, 2011

Professor Gert Cauwenberghs, Chair

Ubiquitous physiological monitoring will be a key driving force in the upcoming wireless health revolution. Cardiac and brain signals in the form of ECG and EEG are two critical health indicators that directly benefit from long-term monitoring. Despite advancements in wireless technology and electronics miniaturization, however, the use of wireless home ECG/EEG monitoring is still limited by the inconvenience and discomfort of wet, contact electrodes. This research focuses on the development of non-contact electrodes, which do not require direct electrical skin contact as a patient-friendly alternative and begins with a review of the field. Early attempts at building non-contact sensors using off-the-shelf commercial components demonstrated the feasibility of building low-cost, wireless, wearable ECG and EEG monitoring systems. As part of this early work, it was discovered that the interface noise from the insulating medium between body and sensor was often dominant, contributing significant new knowledge in this field. Further research revealed that discrete amplifiers contained many limitations, especially regarding frequency response and noise that were difficult to surmount. Previous implementations known in the literature required extensive manual tuning and calibration in order to boost the input impedance of discrete amplifiers, an imperfect and tedious process. To overcome the challenges with using discrete components, a fully custom analog sensor front-end was developed, achieving input impedances and frequency responses far exceeding than what was previously possible, all completely without the need for manual adjustment. Validation of this sensor in ECG applications show that it easily meets medical grade frequency response specifications and attains closer signal correlation to adhesive wet electrodes. Neural applications of this sensor were also explored and validated within an EEG (stead state visual evoked potential) brain-computer interface and benchmarked against dry and wet sensors. Successful real-time control of a computer, to a degree never before demonstrated with non-contact sensors, was achieved with the electrodes placed on top of hair, completely without gels or skin preparation. Additional sensor applications including EOG eye tracking and low-power integrated, focal-plane video compression are also discussed.

Chapter 1

A Review of Biopotential Electrodes

1.1 Introduction

Biopotential recordings in the form of electrocardiograms (ECG), electroencephalograms (EEG), Electrooculograms (EOG) and electromyograms (EMG) are indispensable and vital tools for both medical and research use. These well-proven signal modalities provide a wealth of physiological information, which by virtue of modern bioinstumentation technology, can be harnessed non-invasively and inexpensively for the emerging global health applications of clinical physiological monitoring and medical treatment [1, 2].

Traditionally, Ag/AgCl electrodes with wet conductive gels are used for biopotential recordings. The standard Ag/AgCl electrode has been well-characterized and studied over many decades [3, 4, 5]. Most of its properties are well understood [6], and sufficient empirical data exists for mechanism that not, such as low-frequency noise and drift [4]. Nevertheless, with proper preparation, the signal is excellent.

The basic principles behind gel-less electrodes are also well known. Despite decades of research in alternative biopotential sensor technology [7, 8, 9, 10] for ECG and EEG applications, the standard wet Ag/AgCl electrode is still almost universally used for clinical and research applications. Each year billions of disposable adhesive ECG clinical electrodes are produced, while dry electrodes are limited to niche, non-medical/scientific, applications like fitness monitoring and toys.

The usefulness and performance of dry and non-contact electrodes can be divided in to two categories. The first relate the to the signal quality of the device in terms of noise and motion sensitivity. Second, because electrodes interface to the skin either in contact or close proximity to the body, the specific electrode must also be evaluated for comfort and utility at the system level. This paper aims to critically address the latest developments in dry and non-contact electrodes accounting for both of these considerations. One chief advantage of the standard clinical wet electrode is the fact that it adheres very well to skin. While problematic from a patient comfort standpoint in long-term use, adhesive wet electrodes stay fixed to specific, clinical-standard locations on the body. Dry and non-contact electrodes address the comfort issues with the adhesive wet electrode, but are much more difficult to secure against the patient. Thus for these technologies to be clinically useful, mechanical solutions must be devised to place the electrodes in the proper position (such as the 12-lead ECG) or an alternative application niche must be found. It is for these reasons, that dry and non-contact electrodes are unlikely to replace the standard hospital ECG or EEG electrode.

The literature around dry electrode technology is quite vast, but dispersed across multiple, semi-isolated, research groups and publications. In addition, the amount of information is compounded by all of the possible applications (ECG, EEG, etc). With that in mind, this paper reviews the latest developments in dry/non-contact electrodes while providing a historical context and a discussion of the challenges and future directions for this field. In 2000, Searle et. al [3] published a detailed comparison between standard wet Ag/AgCl and their specific implementation of a dry and insulating electrodes from an impedance, interference motion artifact rejection perspective. In contrast to conventional wisdom, their paper demonstrated that dry and insulate electrodes (if buffered and shielded) can perform as well, if not better than standard wet Ag/AgCl electrodes in each of these respects. However, the intrinsic noise properties of the electrode were not discussed and the paper was limited to only two, specific dry and insulated electrode implementations.

This paper presents a systematic comparison between the various contact and non-contact electrode technologies with a focus on quantifying the noise performance and motion sensitivity as a function of physical and electrical parameters, as well as their unobtrusiveness and ease for clinical use. The following section presents a general

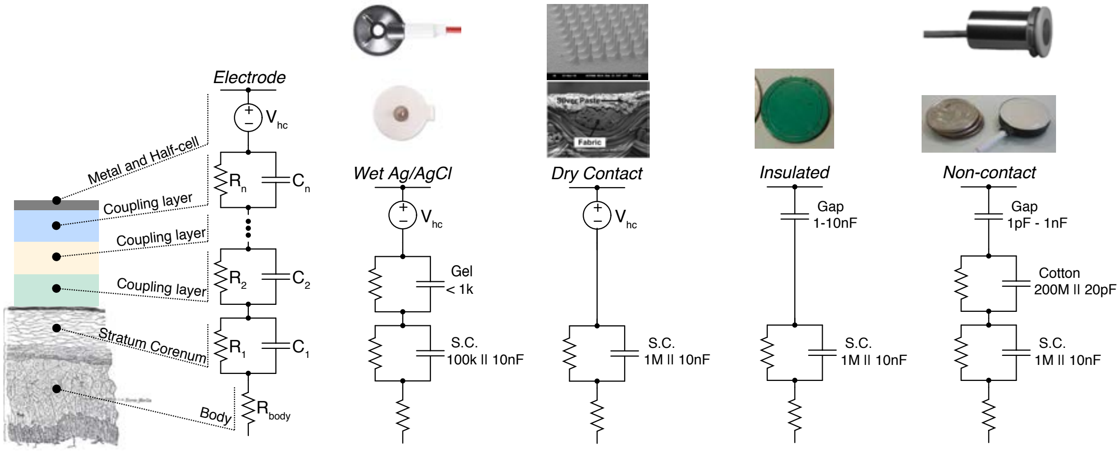

Figure 1.1: Electrical coupling of the skin-electrode interface for various electrode topologies, including wet-contact gel-based Ag/AgCl, dry-contact MEMS and metal plate, thin-film insulated metal plate, and non-contact metal plate coupling through hair or clothing such as cotton. The insets show examples of practical electrodes for each category as described in Section 3.

model of the electrode interface, described and characterized with measurements from an electrical perspective. This establishes the fundamental principles for dry and non-contact electrodes and describes the fundamental signal quality limits. The different electrode technologies and their properties are surveyed next, and the paper concludes with a discussion of the latest developments in the literature along with future directions and challenges.

1.2 Skin-Electrode Interface

The concept of “electrode” is rooted in the study of electrochemical cells where electrical transport is governed by oxidation and reduction reactions taking place at the interface between a metal and an electrolyte. A conventional wet-contact electrode fits this description, since the metal conductor of the electrode is bathed in an electrolyte gel or solution that buffers the electrolytic composition through the outer and inner layers of the skin. Therefore a wet-contact electrode is well characterized by a half-cell potential, a double layer capacitance, and parallel and series resistances as shown in Figure 1.1. For a dry-contact or non-contact electrode, however, the interface is more complex and other processes enter the electrical interactions in skin-electrode coupling.

In general, the coupling between skin and electrode can be described as a layered conductive and capacitive structure, with series combinations of parallel RC elements. The type of electrode and skin coupling result in several such structures, as shown in Figure 1.1, with different conductance and capacitance values. For each of these electrode types, typically one of the RC sections dominates and the electrical coupling may be represented as a single element with conductance g_c in parallel with capacitance C_c, or a simplified coupling admittance $Y_c(j\omega) = g_c + j\omega C_c$.

It is important to realize that both conductance and capacitance are important in characterizing electrode performance. In what follows we will show that the conventional notion that low resistance (high conductance) is essential for good electrode performance could be misleading, and that maximizing resistance (minimizing conductance) in electrode-skin coupling is actually beneficial in certain important limiting cases. This unconventional and seemingly counter-intuitive observation derives from simple circuit theory validated by experimental data, which we offer here for the benefit of the reader who may have missed this important point from previous literature coverage on electrode interfaces. Thereby we hope to rectify misunderstandings in the role of coupling conductance on noise performance and sensitivity to guide better and more informed decisions in the design of the electrode and the skin coupling medium.

1.2.1 Electrical Model

To accurately model the effect of the skin-electrode coupling admittance $Y_c(j\omega)$ on the quality and robustness of the received signal, it is necessary to account for the electrical coupling between the skin and the amplifier connected to the electrode to acquire the signal. We consider the general, actively shielded amplifier topology shown in Figure 1.2 (left), chosen for its relative immunity to interference from other sources and line noise [3]. This topology conforms to many of the published amplifier circuits for dry-contact and non-contact electrodes, *e.g.,* [11, 12, 13]. A particularly simple low-power and compact realization, which is used in the experimental data presented in this survey, is illustrated in Figure 1.2 (right).

We define the following electrical signals and parameters in reference to the circuit topology in Figure 1.2 (left) and its noise model in Figure 1.3 (left):

$v_s(j\omega)$: signal source on skin surface;
$v_o(j\omega)$: signal recorded at amplifier output;
$v_{i,n}(j\omega)$: input referred amplifier voltage noise;
$i_{i,n}(j\omega)$: net current noise at amplifier input;
$Y_c(j\omega)$: $g_c + j\omega C_c$, skin-electrode coupling admittance;
$Y_i(j\omega)$: $g_i + j\omega C_i$, amplifier input admittance;
C_s: active shield to electrode capacitance;
A_v: amplifier voltage gain.

The resulting received output signal v_o can be written as

$$v_o = G(j\omega)\,(v_s + v_{s,n}) \tag{1.1}$$

with a source-to-output signal voltage gain

$$\begin{aligned} G(j\omega) &= A_v \frac{Y_c(j\omega)}{Y_c(j\omega) + Y_i(j\omega) + j\omega(1 - A_v)C_s} \\ &= A_v \frac{g_c + j\omega C_c}{g_c + g_i + j\omega(C_c + C_i + (1 - A_v)C_s)} \end{aligned} \tag{1.2}$$

and source input-referred voltage noise

$$\begin{aligned} v_{s,n} &= \frac{Y_c(j\omega) + Y_i(j\omega) + j\omega C_s}{Y_c(j\omega)} v_{i,n} + \frac{i_{i,n}}{Y_c(j\omega)} \\ &= \frac{g_c + g_i + j\omega(C_c + C_i + C_s)}{g_c + j\omega C_c} v_{i,n} + \frac{i_{i,n}}{g_c + j\omega C_c} \end{aligned} \tag{1.3}$$

These expressions give a quantitative means to analyze the noise performance as well as the motion and friction sensitivity of various electrode topologies in terms of physical and electrical circuit parameters, presented next.

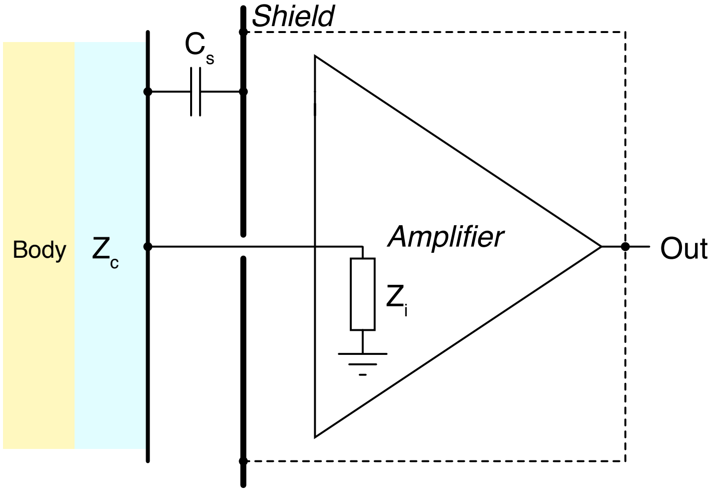

Figure 1.2: Simplified topology and circuit model of a general, actively shielded biopotential amplifier [11]. The active shield guards the high-impedance input from interference by other sources, and implies capacitive coupling between the source and the amplifier output.

1.2.2 Noise

The source input-referred noise power density follows directly from (1.3):

$$
\begin{aligned}
v_{s,rms}^2 &= \frac{|Y_c(j\omega)+Y_i(j\omega)+Y_s(j\omega)|^2}{|Y_c(j\omega)|^2} v_{i,rms}^2 \\
&\quad + \frac{i_{i,rms}^2}{|Y_c(j\omega)|^2} \qquad (1.4) \\
&= \frac{(g_c+g_i)^2+\omega^2(C_c+C_i+C_s)^2}{g_c^2+\omega^2C_c^2} v_{i,rms}^2 \\
&\quad + \frac{i_{i,rms}^2}{g_c^2+\omega^2C_c^2}. \qquad (1.5)
\end{aligned}
$$

The relative contributions of the two noise components are illustrated in Figure 1.3. The first noise component, proportional to the amplifier voltage input noise $v_{i,rms}^2$, is scaled by a factor inversely proportional to the electrode coupling efficiency. For low-impedance contact sensors, this voltage noise component reduces to the amplifier noise floor, while for high-impedance contact sensors such as non-contact geometries, the amplifier voltage noise floor is amplified by a factor $1+(C_i+C_s)/C_c$. This noise amplification could be

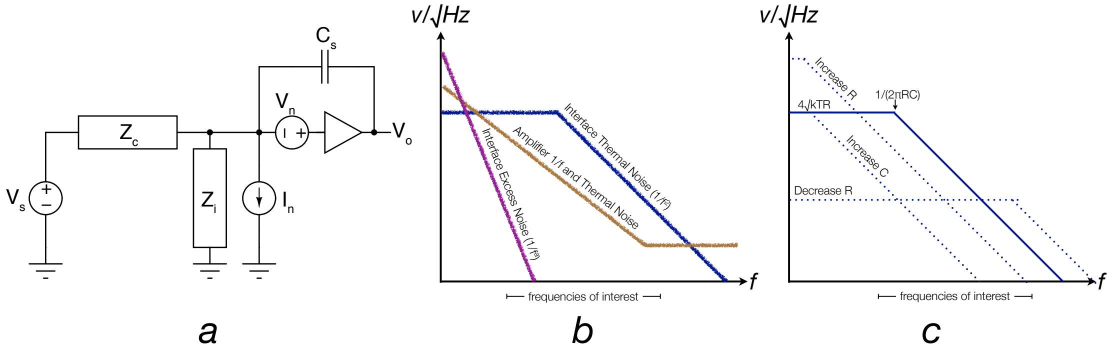

Figure 1.3: Dry/non-contact amplifier circuit noise model along (a) with a simplified plot of the frequency behavior of the various noise sources (b). For each RC layer, the in-band noise contribution can be decreased by either drastically increasing the resistance towards infinity, increasing the capacitance or reducing the resistance towards zero (c).

reduced by minimizing the active shield capacitance as well as amplifier input capacitance. However, as shown in Figure 1.3, this first noise contribution does typically not dominate at frequencies of interest, except for non-contact electrodes at large distance with poor electrode coupling. The second, and typically more significant noise component is proportional to the net current noise $i^2_{i,rms}$ into the coupling impedance. This net current noise combines thermal noise contributed from the skin-electrode coupling conductance g_c and amplifier input conductance g_i, besides amplifier input current noise $i^2_{i,n}$. This noise component is fundamental to the skin-electrode coupling interface which typically dominates contributions from the amplifier. In the limit of a perfect noiseless, infinite input impedance amplifier, the source input-referred noise power density (1.5) reduces to

$$v^2_{s,rms} \approx \frac{4kT\,g_c}{|Y_c(j\omega)|^2} = \frac{4kT}{g_c + \omega^2 C_c^2/g_c}. \tag{1.6}$$

Paradoxically, (1.6) shows that fundamentally the source input-referred noise can be reduced to zero in two limits of particular interest: either infinite coupling conductance (low-resistance contact sensing), or infinite coupling impedance (capacitive non-contact sensing). This presents a rather interesting dichotomy– either of the two extreme cases of zero resistance and infinite resistance of skin-electrode contact are actually optimal for low-noise signal reception.

Table 1.1: Measured Electrode Impedances

Wet Ag/AgCl	350k ‖ 25nF
Metal Plate	1.3M ‖ 12nF
Thin Film	550M ‖ 220pF
Cotton	305M ‖ 34pF
MEMS	650k ‖ ‖

Measured data on noise obtained from the differential signal between two closely spaced electrodes on the forearm at rest are given in Figure 1.4, showing general agreement with the noise model (1.6) with measured values of coupling resistance and capacitance (Table I). As expected, the instrumentation noise floor of the amplifier (Figure 1.2) is dominated by the measured data, confirming that the conditions for the limit model (1.6) are satisfied. Interestingly, the only electrode type with consistently higher observed noise than the predicted thermal noise from the skin-electrode coupling noise model are the wet-contact Ag/AgCl electrodes at lower frequencies. Elevated $1/f$-like low-frequency drifts of the Ag/AgCl offset (half potential mismatch) voltage were confirmed in extended (1-hour) recordings, and are consistent with observations in Huigen et al [4].

One interesting result from this experiment is that for "capacitive" non-contact electrodes operating through clothing [14] [15], the noise performance and electrode coupling is actually dominated by the *resistive* component of the cotton layer rather than a capacitance. In many cases, dry contact electrodes are much more capacitively dominated than non-contact electrodes through clothing. Although difficult to imagine, cotton actually acts as a poorly conductive electrode ($>200\,\text{M}\Omega$), and is especially harmful for biopotential measurements. The impedance of cotton is such that the coupling is mostly resistive in the frequencies of interest, and amounts to adding a large and noisy series resistor in the signal path. Had the resistance been higher (ie. very dry), or the shirt been thinner (increased capacitance), the noise floor would have been lower. However, the increased noise did not prevent some acceptable ECG measurements.

Sample ECG data recorded from the same system with metal-plate electrodes mounted on the chest is shown in Figure 1.5, showing reasonably accurate correspondence between the dry-contact as well as non-contact electrodes against a wet Ag/AgCl electrode reference, even for electrodes placed over a shirt. The capability to continuously record ECG without direct skin contact opens the door to long-term clinical home diagnosis and care applications.

1.2.3 Motion and Friction

Relative motion of electrodes with respect to the body, as well as friction of electrodes against the body surface, give rise to artifacts in the received signals that are one of the main impediments against the acceptance of dry-electrode and non-contact biopotential sensors in mobile clinical settings. These artifacts, however, are not unique to electrodes with poor resistive contact, and arise in low-resistance wet-contact electrodes as well. They can be reduced, but not eliminated, by partly containing the relative motion to careful mechanical design, although at some expense in the comfort, size and weight of the mounted sensors.

The effect of motion and friction on the signal reception can be readily identified, to first order, from the electrical model (1.1), (1.2) and (1.3). We distinguish between two sources of error that are induced by motion of the electrode relative to the body surface: transversal motion, and lateral motion and friction.

Transversal motion primarily gives rise to instantaneous changes in the skin-electrode coupling impedance, changes which can be discontinuous for contact-based sensors in the absence of a gel bath between skin and electrode. The effect of these impedance changes are similar to the signal arising due to membrane deflections in a microphone, and need to be carefully mitigated in the circuit design to avoid vibration and other mechanical deflection sensitivity. According to (1.2), the effect of changes in coupling admittance $Y_c(j\omega)$ are nulled out when the following impedance balancing condition is met:

$$Y_i(j\omega) = j\omega(A_v - 1)C_s \tag{1.7}$$

or, equivalently:

$$\begin{aligned} g_i &= 0 && (1.8) \\ C_i &= (A_v - 1)C_s. && (1.9) \end{aligned}$$

The zero input conductance condition (1.8) is readily implemented with a CMOS or other high-impedance amplifier. The balanced capacitance condition (1.9) is more difficult to implement since input impedance depends on circuit non-idealities that may vary with signal level, such as amplifier protection diodes. The most common approach taken for precise tuning of the capacitive balance is to provide a variable voltage gain A_v or trimmed capacitance active shield C_c, although repeated adjustments may be necessary and are costly to implement. A simple alternative approach, also extensively used, is to provide unity gain active shielding $A_v \approx 1$, along with minimizing the input capacitance C_i. This approach is taken in the active electrode of Fig. 1.2, with a unity gain connected LMP7702 with 5 pF input capacitance.

Lateral motion in contact may induce friction when the electrode is in direct contact with the skin or with a partially solid coupling medium, a source of error due to possible induction of triboelectric charge onto the electrode surface. No satisfying quantitative models exist to generally describe this effect, but to first order we may consider continuous friction to induce a triboelectric current adding to the net current noise into the amplifier input, resulting in an additional voltage noise component

$$v_{t,rms}^2 \approx \frac{i_{t,rms}^2}{|Y_c(j\omega)|^2} = \frac{i_{t,rms}^2}{g_c^2 + \omega^2 C_c^2}. \qquad (1.10)$$

which shows that low skin-electrode impedance (either in terms of low coupling resistance, or high coupling capacitance) directly reduces the effect of friction.

Figure 1.6 qualitatively illustrates the effect of walking and running body activity, inducing motion and friction in random directions, on the ECG signal recorded using non-contact electrodes over a cotton shirt, in comparison to wet contact sensors simultaneously mounted on the skin under the shirt. A tight vest around the waist assisted in mechanically containing the relative motion, and a wireless interface provided mobility while avoiding common-mode noise and line noise pick-up [14]. The wet contact sensors showed reduced, but not completely eliminated, signal artifacts during activity relative to the non-contact sensors. The R wave of the ECG however remained clearly visible both for the wet and non-contact sensors. Practical issues with motion and friction are further discussed in Section 1.2.4, and more particularly for non-contact sensors in Section 1.3.2.

1.2.4 Practical Design Considerations

Broadly speaking, two approaches have been taken to resolve the issue of electrode-skin contact impedance for low-noise, low-artifact biopotential sensing. The traditional solution has been to simply abrade the skin to obtain a very low contact resistance (5-10 $\mathrm{k\Omega}$). At the other extreme, one common practice has been to employ an amplifier with such high input impedance that the skin-electrode impedance becomes negligible. For wet electrodes, neither extreme is necessary, but the problem of contact impedance becomes a much more pressing problem for dry and non-contact sensors, for which maximizing input impedance is the only viable alternative.

Achieving truly non-conductive, non-contact sensing, however, is difficult in practice. Fully accounting for the electrical coupling between the skin and the electrode, and its effect on noise (1.4), is generally quite complex, because of the different layers of coupling involved through skin and the coupling medium (Figure 1.1). Low resistance layers generate no appreciable thermal noise. High resistivity layers may generate large thermal noise voltages, but these voltages get shunted away as long as the impedance of the parallel capacitance is sufficiently low over the frequencies of interest. At the most basic level, the coupling impedance can be described as a single resistance in series with a parallel conductance-capacitance combination (center in Figure 1.1). In practice, we find (Figure 1.4) that all electrode types couple signals both resistively and capacitively in the frequencies of interest for biopotential signals. The interplay between electrode conductance and capacitance is one of the critical factors determining the limits on noise performance.

Also, the success in reducing noise by increasing coupling resistance depends on the impedance level of the coupling capacitance, which strongly depends on frequency. For low capacitive coupling (at large distance), higher electrode resistances translate directly into increased noise levels, both intrinsically due to thermal noise and induced by motion and friction artifacts. According to (1.6), increasing the coupling resistance only lowers noise for values of resistance R_c larger than $1/\omega C_c$. This value becomes exceedingly large for increasing electrode distances. For this reason, the most demanding applications where close proximity to the skin cannot be warranted, like research EEG over haired skull, still require wet electrodes.

In summary, nearly all aspects of the performance of an electrode are critically limited by the physical properties of the interface between skin and the electrode, rather than amplifier goodness criteria (even though these still need to be met).

1.3 Electrode Technologies

1.3.1 Dry Electrodes

In contrast to wet Ag/AgCl electrodes, dry electrodes are designed to operate without an explicit electrolyte. Instead, it is usually supplied by moisture on the skin (ie. sweat). Numerous variations of dry electrodes exist ranging from simple stainless steel discs to micro-fabricated silicon structures with built-in amplifier circuitry. Employing dry contact sensors somewhat more challenging in practice than traditional techniques largely due to the increased skin-electrode impedance, although the impedance can be quite comparable to wet electrodes after a few minutes due to sweat and moisture buildup [16]. Successful designs use either an active electrode circuit to buffer the signal before driving any cabling or alternatively penetrate the skin to achieve a low contact impedance.

In its simplest form, a dry electrode can be built from any conductive material in contact with the skin, such as a flat metal disc (Fig. 1.2) and is well-known in the literature [16]. As an example, Valchinov et. al presents a modern variation of this design in 2004. Performance and signal quality of these simple electrodes can as good as wet electrodes, especially if an amplifier [17] is onboard. Dry electrodes work well for quick measurements (such as exercise machines), but suffer from usability problems for normal clinical applications. Standard wet electrodes usually include an adhesive material to fix the electrode in proper locations, and a hydrogel or wet-foam to both lower the skin impedance, and buffer the electrode against mechanical motion. Adding an adhesive material to place these dry electrode in the proper clinical locations for continuous use eliminates many of its comfort/convenience advantages. Nevertheless, the simplicity and durability of metal dry electrodes make it highly useful for applications like ECG event monitors where short, infrequent use over long periods of time is expected.

Flexible versions of the dry electrode based on rubber [18], fabric [19] [20] [21] or foam are also possible and more appealing from both a comfort and usability standpoint. Softer materials have the advantage of conforming easily against the skin, increasing comfort and contact area. Gruetzmann et. al demonstrated a foam electrode [22], which exhibited excellent stability with increased resistance to motion artifact versus the wet and rigid dry Ag/AgCl electrode.

The high-resistance layer of the skin, the Stratum Corneum, is typically abraded or hydrated to achieve a lower resistance and better electrode contact. It is also possible to penetrate the 10-40 μm layer with microfabricated needles [23] [24]. Bypassing the Stratum Corneum can achieve a contact as good as, if not better, than a standard Ag/AgCl electrode [23] without the need for any skin preparation or gel. To date, preliminary data has been available for EEG applications of this electrode. However, long-term studies on the hygiene, comfort and safety of this technology is unavailable. The authors have observed irritation and slight pain when using these electrodes. It is certainly conceivable that they must be single use, and necessarily be packaged pre-sterilized.

For EEG, recording signals reliably through thick layers of hair remains one of the key challenges. One technique, using dry sensors that do not require scalp preparation, involve the use of thin fingers that can penetrate through hair, first described in a patent by Gevins et al. in 1990 [25]. Several research groups have demonstrated this technique successfully. Matthews et al. [15] presents one well characterized version of this sensor, and show that the EEG signal obtained can be largely comparable to wet electrodes, for stationary subjects. However, the high skin-contact impedance results in a much larger motion artifact with the dry sensors. Fiedler et. al. published a TiN based fingered dry electrode that reported an impedance of 14-55 kΩ/finger vs around 10 MΩ/finger [15])

The final type of dry electrode, first demonstrated by Richardson in 1968 [8], does not require ohmic contact at all [10]. In Richardson's original design, a simple Aluminum disc was anodized to form a large blocking capacitor in series with the skin. Signals were capacitively coupled to the input of an FET buffer amplifier and subsequently connected to standard instrumentation.

Taheri et al. expanded on this design by fabricating an insulated electrode on a silicon substrate which integrated a buffer amplifier [26]. It was also designed to have multiple, redundant sensing sites along with a simple algorithm to select the channels that are most likely to have a good contact.

The combination of a good dielectric material combined with physical skin contact means that the coupling capacitance for insulated electrodes is relatively large, from 300 pF [26] to several nanofarads. As a result, designing a bias network with low noise and frequency response for clinical grade signals is very feasible with a standard high-impedance input FET amplifier.

In most respects, the usage and performance of insulated electrodes is quite similar to dry electrodes in practice. Some limited data exists that suggest capacitively coupled electrodes suffer from less skin-motion artifact noise than dry electrodes [3]. More detailed studies need to be conducted to determine what advantage, if any, can be achieved by inserting a layer of insulation between the skin and electrode. From an electrical perspective, the high capacitance of the thin insulation layer is an effective short at signal frequencies and have no effect on the signal quality vis-a-vis dry electrodes. One obvious downside, however, is that the insulated nature of the electrode precludes a frequency response down to DC, which may be important for certain applications.

1.3.2 Non-contact, Capacitive Electrodes

Wet and dry electrodes both require direct physical skin contact to operate. The final type of sensor, the non-contact electrode, can sense signals with an explicit gap between the sensor and body. This enables the sensor to operate without a special dielectric layer and through insulation like hair, clothing or air. Non-contact electrodes have been typically described simply as coupling signals through a small capacitance (10's pF) [11] [12] [27]. In reality, however, there is typically an important resistive element ($>100\,\mathrm{M\Omega}$) as well, since the typical insulation (ie, fabric) will also have a non-neglible resistance [28]. As shown previously, signal coupling through non-contact electrodes can be actually dominated by the resistive part of the source impedance which can cause a large input voltage noise.

Designing an amplifier to acquire signals from such a high source impedance is quite challenging. Typical design problems include achieving a high enough input impedance and a stable bias network that does introduce excessive noise. Finally, very high impedance nodes are susceptible to any stray interference and motion induced artifacts.

Nevertheless, in 1994 Prance et al. demonstrated a working non-contact system with an array of 25 ECG senors [29] that was designed to acquire signals with a 3mm spacing from the body. A low-leakage biasing circuit using a bootstrapped reverse diode, combined with positive feedback to neutralize the parasitic input capacitance was used to achieve an extremely high impedance, reported at ($10^{16}\Omega$, $10^{-17}F$). However it is not clear how these measurements were made or over what bandwidth. In addition, the effective input impedance with neutralization is a complex function of both the coupling capacitance and frequency.

In 2000, Prance et al. published an improved version based on the INA116 electrometer instrumentation amplifier from Burr-Brown (Texas Instruments) with a lower noise floor [30]. It again utilizes positive feedback to for neutralization of the input capacitance. While the specifics were not published, it can be inferred that process is far from perfect, as it requires manual calibration and different devices do not match well [31]. Detailed descriptions of bootstrapping and neutralization techniques, however, can be found in unrelated fields [32] as well as a very old publication [33] based on vacuum tubes, but the principles are fully applicable to modern amplifiers. It is not clear as to what advantages of attempting to maintain such a high input impedance, as many other papers show excellent results with much simpler circuits.

The ability to sense biopotential signals through insulation has resulted in ingenious implementations ranging from sensors mounted on beds [28] [21], chairs [34] and even toilet seats [35]. In general, the signal quality ranges from poor to quite good, as long as proper shielding and subject grounding techniques are utilized [36].

Kim et al makes an important contribution in this field by extending the analysis for the driven-right-leg scheme for capacitive applications [36]. In particular, he shows that an active ground, even capacitively coupled, is highly effective at reducing line noise. It is worthwhile to note that the active ground connection can be capacitive as well for a system that is truly non-contact. A few other key publications in this field have mentioned the need for least dry contact [27] [13] to ensure proper operation. This extra degree of common-mode rejection is especially useful in light of the input impedance problem.

Unfortunately, specific key circuit and construction details for non-contact sensors have generally not been available in the literature. In particular, the critical information relating to input biasing, input capacitance neutralization and circuit reference/grounding that allow someone to duplicate the sensor and experiments have been scarce. A complete design for a non-contact, wireless ECG/EEG system can be found in [14], which improves and summarizes upon their previous designs [37, 38, 27, 12]. These non-contact sensor designs are very simple and robust, manufactured completely on a standard PCB with inexpensive and commonly available components (chip resistors, capacitors and the National LMP7723 and LMP2232). The critical input node was left floating and it was found that the input can reliably self-bias purely through the device's internal ESD protection structure. Since no extra conductive devices were added to the input, the circuit achieved the optimal noise performance of the amplifier. The DC offset was simply removed with a passive high-pass filter before the second, differential gain stage. The sensor performed well in laboratory environments and 60 Hz noise was virtually absent through the use proper shielding, an active ground and a fully isolated, wireless system. These papers can serve as a useful starting point and timesaver for researchers who wish to develop and experiment with their own non-contact sensors.

One key drawback with capacitive, non-contact sensors, as explained in Section 1.2.3, is their susceptibility to motion artifacts. Several authors have demonstrated performance comparable to clinical adhesive electrodes [13] [14], through a t-shirt, with a moving subject for ECG. The caveat, however, was that this required a tight vest and chest band to secure the non-contact electrodes in place [14]. This highlights the key, unresolved, problem with non-contact electrodes - susceptibility to motion induced artifacts. For non-contact electrodes, artifacts tend to be dominated by three sources. First, the high-impedance, capacitively-coupled, input node of the electrode exhibits a large time settling time constant. Second, displacements in the electrode-to-skin distance can cause artifacts [39]. Finally, friction between the electrode and insulation (fabric, hair, etc.) can cause large voltage excursion at the sensitive input.

Typically non-contact electrodes exhibit poor settling times due to the high-pass characteristic at the electrode. Figure 1.7 shows the settling for a non-contact ECG sensor with a low-frequency response that extends down to 0.05 Hz prescribed for ECG. Recovery times of upwards of 10 seconds can be seen, and are exacerbated by the non-contact electrode's susceptibility to movement induced overloads and artifacts. Faster recovery is possible by shifting the corner frequency of the high-pass filter, but at a cost of distorting the signal waveform. Achieving a good frequency response without the settling time problem remains an unsolved challenge.

All known non-contact sensor designs deliberately limit the high-pass corner frequency to at least around 0.5 Hz to 1 Hz, which introduces appreciable distortion in the ECG waveform. The clinical usefulness of this distorted ECG versus the standard trace is not known by the authors and needs further consideration.

Simple models have been devised to model and solve the displacement artifact for capacitive ECG sensors [39], proposed by Ottenbacher et al., but rely on precise knowledge of the coupling capacitance. Thus while effective in simulations and controlled bench experiments, it has yet to be reliably demonstrated on actual live recordings. On the other hand, there is no know solution to friction-induced artifacts.

As it stands, there is no real impediment to building fully functional non-contact sensors from standard off-the-shelf amplifiers, and the actual implementation can be as simple as a dry electrode, with proper component selection. For actual usage, the non-contact electrode's susceptibility to motion artifacts, friction and thermal noise are problematic.

1.4 Systems

The relative utility of dry-contact and non-contact electrodes, in contrast with the more established and widespread wet-contact electrodes, is inextricably tied to novel systems applications or tools that it can enable. In this section we discuss such enabling systems application domains for two main clinical needs: cardiac and neurological monitoring. Examples of systems in their applications environments for clinical ECG and EEG use are illustrated in Figure 1.8.

1.4.1 ECG

It is unlikely that dry electrodes will ever replace the adhesive, wet Ag/AgCl for in-hospital use. Standard electrodes adhere well to the body, are robust, inexpensive and simple. Properly used, wet electrodes provide an excellent signal. Dry or non-contact electrodes offer little advantages for the majority of hospital applications, while adding cost and complexity (such as the for active electrode circuitry). It is worth noting, however, that for situations where patients with extremely sensitive skin (ie. burn units [45], neonatal care [46] [47]), dry and non-contact electrodes may be desirable.

At a basic level, the Polar Heart Rate monitor is one well-known example, although non-clinical, of a dry electrode based system for cardiac monitoring. The basic theme of a wearable, dry-contact chest strap/harness has been demonstrated by several authors [13] [40] and at least one known medical device company (Monebo). They provide a very easy way to continuously obtain a 1-lead ECG. Given the right analysis and wireless clinical infrastructure, dry-contact chest straps may prove to be a viable tool for long-term cardiac monitoring. With non-contact sensors, it is also possible to build a strap/harness that can be worn on top of a t-shirt [14], with electrodes placed in approximate positions to provide a derived 12-lead ECG [14]. Motion artifacts and chest tightness, however, remain a difficulty with wearable, non-contact systems.

Small bandage-like patches are even more convenient than chest straps for long-term, mobile monitoring. Recent advancements in microelectronics electronics have made it possible to integrate an entire ECG monitoring systems within a small patch. Yoo et. al presents a inductively powered ECG chest patch [20, 48, 49] based on a single integrated circuit mounted on a fabric substrate. A few commercial offerings are also now on the market, in a somewhat larger form-factor (Corventis, iRythm, Proteus). Unfortunately the short electrode-to-electrode distance makes it impossible to obtain the same waveform as even a standard 1-lead ECG, although the QRS complex is readily visible in the most cases. These devices have potential to be highly useful for basic long-term cardiac monitoring, such as arrhythmia detection.

Besides mobile wearable devices, non-contact electrodes have been used for rapidly obtaining chest body surface potential maps (BSPM). In fact the, first demonstration of non-contact electrodes [29] was for a chest array. Newer versions have been developed, mounted on a standard tablet PC [50]. Non-contact electrodes have a distinct advantage since it can be taken through clothing without any preparation. However, it is not clear what the clinical advantages are for non-contact BSPMs, especially in light of the noise and frequency responses of non-contact electrodes. A contact version, perhaps embedded within a tight garment, could prove useful, provided the extra information over a 12-lead ECG is clinically relevant.

Clinical ECG monitoring devices have traditionally required patients to wear a device on the body. With the exception of an implantable monitor, all of these systems require some degree of patient intervention and compliance. The advent of non-contact electrode technology has made it possible to integrate cardiac monitoring devices unobtrusively in the environment. Several attempts have been made to integrate electrodes in beds [28], chairs [34] [42] [51] and even bathtubs [52] and toilets [35]. Obtaining signs of cardiac activity through an air gap (40 cm) is also possible [53]. Unfortunately, signal quality from these devices is typically quite poor and riddled with motion artifact, noise and interference problems. At present, nothing has progressed beyond a basic proof-of-concept. More detailed clinical studies are required to find out if the degree of monitoring provided by beds and chairs is clinically useful.

1.4.2 EEG

Unlike ECG, which has a long and established clinical practice of outpatient monitoring systems, the difficulty in preparing a patient and data interpretation has largely limited brain monitoring to in hospital settings. With the exception of an EEG counter part to the 24/48-hour ECG Holter device, mobile clinical EEG devices are still rarely used today. However, there does exist a strong need and interest for EEG monitoring for medical conditions such as sleep apnea, epilepsy and traumatic brain energy. Thus, a novel applications and uses are even more critical for the success of dry electrode technology for EEG. Thus, it is expected that these wireless, outpatient EEG-based neural monitoring systems will become much more commonplace in the near future. A robust and patient-friendly dry electrode system will be a significant contribution to this field.

At this time, there exists no clinical dry/non-contact EEG device on the market.

Several commercial offerings have been made mostly with a consumer focus for entertainment (Neurosky), sleep/wellness (Zeo) and marketing (Emsense). However, there has been significant activity with using dry EEG systems for research use [54, 43, 15].

Sullivan et al. presented an architecture for high-density, dry-electrode EEG based around the concept of integrating the entire signal processing (amplification, filtering, digitizing) chain on top of a dry MEMS electrode [43] . This enables electrodes to be easily daisy-chained and expanded with only one common-wire, significantly reducing the clutter associated with a conventional EEG system. It is easily wearable and provides access to the forehead locations without gels or other preparation.

Monitoring of user attention or alertness is another area that has been explored as a candidate for dry-contact EEG. Several headsets have been developed with this in mind [44, 15]. In 2009 Tsai et al. presented a detailed study of using dry-contact EEG sensors to monitor for driver drowsiness [44].

At present, dry-contact EEG systems are limited to only reliably acquiring forehead signals, due to the vastly varying thickness of human hair. Thus, for clinical applications to be truly viable, clinical procedures and validation must be established for this limited set of EEG signals first.

1.5 Discussion

From an electronics perspective, nearly almost all of the circuit design issues are now well understood and well described in literature, from achieving high common-mode rejection to building micropower circuitry. In essence, a modern FET-input amplifier configured in unity-gain will be more than sufficient to buffer signals from virtually any electrode. Achieving a sufficiently high input impedance is not a problem for the majority of cases. Input offsets are problematic, but DC-coupled instrumentation with very low gains (0 dB) and high-resolution ADCs (24-bit) can tolerate large electrode offsets. Except for esoteric applications, such as ECG sensing through a large air-gap, it is unlikely any circuit innovation directly at the electrode will be highly useful. It goes without saying, however, that there is much room for circuit/electronics innovation at the system level for building integrated, wearable and wireless biopotential sensors.

Resolving the difficulties with motion artifacts remains the unsolved challenge in mobile, wearable ECG/EEG sensor systems. Unlike circuit characterization which involves standard, easily simulated and readily measured parameters like noise, gain and power consumption, motion artifacts are ill-defined and subject to human variability. In addition, different types of electrodes suffer from artifacts from distinct sources. The lack of quantifiable merits compounded with the difficulty in obtaining measurements has resulted in less attention in this area.

In addition, fully understanding and characterizing the origin of skin-electrode noise is another under addressed area in this field. It is well known that that the noise level, while strongly correlated with skin impedance, far exceeds the amount predicted by thermal noise at low frequencies [4]. It has been theorized that the redox reaction at the electrode accounts for the $1/f$ characteristic with wet Ag/AgCl electrodes. It has not been established that electrochemical noise contributes to capacitively coupled non-contact sensors, since redox reactions do not take place across the interface. Our theory and experimental observations have shown that for non-contact electrodes, the thermal noise model is more accurate, and provides some clear guidelines for design considerations in the electrode interface. Again the lack of standard measurement methods combined with human variability makes an objective comparison scarce and difficult. An establishment of a clear measurement protocol followed by detail, objective, comparisons of the noise behavior of all electrode types will be highly illuminating.

Overall, there also needs to be a greater emphasis on the materials, packaging, signal processing and systems level. The ultimate solution will likely be a combination of some circuit design, but even more a matter of innovative mechanical construction and signal processing. Efforts directed in that direction are expected to yield significant returns for this field.

Chapter One is largely a reprint of material that appeared in the 2010 IEEE Reviews of Biomedical Engineering Paper: Y. M. Chi, Tzyy-Ping Jung and Gert Cauwenberghs, “Dry and Non-contact Biopotential Electrodes,” *IEEE Reviews in Biomedical Engineering*, 2010. The author was the primary author and investigator of this work.

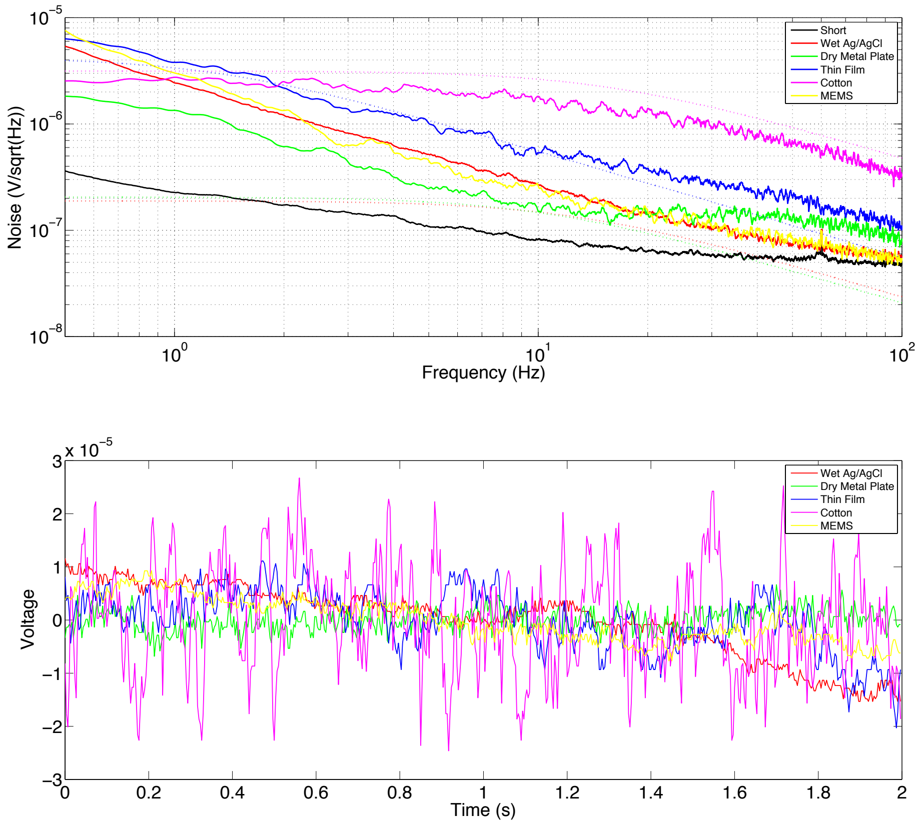

Figure 1.4: Measured noise spectrum of various electrode types, placed at close proximity on the forearm at rest, along with the predicted (dotted lines) thermal noise limits (1.6) from measured skin-electrode coupling impedance data. (Top) The instrumentation noise floor of the amplifier (Figure 1.2) is also shown for reference. The time-domain noise plots are also shown (Bottom).

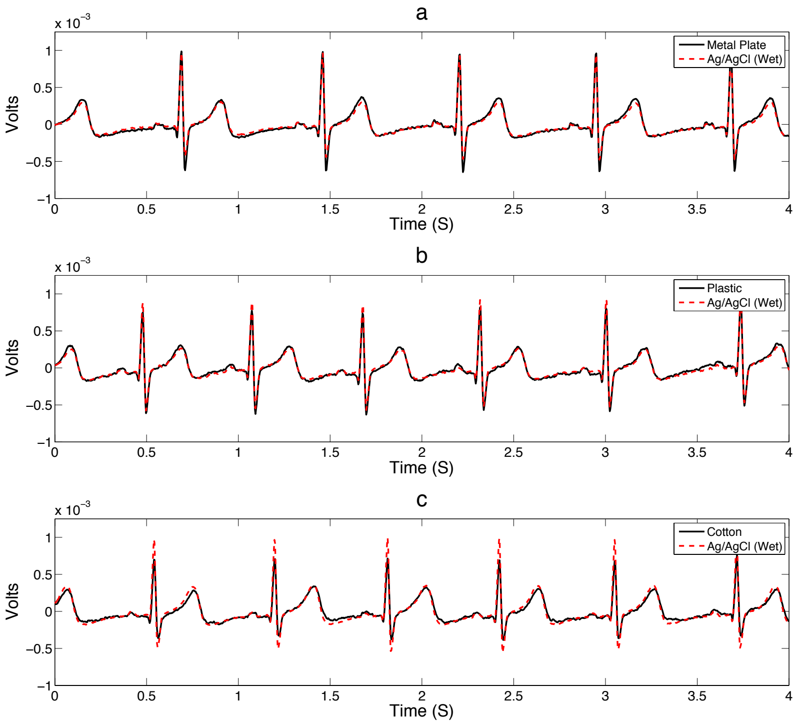

Figure 1.5: ECG samples taken from the various dry-contact and non-contact test electrodes (metal contact, thin film insulation, cotton non-contact), plotted against the signal taken simultaneously from a wet Ag/AgCl electrode. The data is shown from a .7 Hz to 100 Hz bandwidth without a 50/60 Hz notch. The increased noise floor of the plastic and cotton electrodes are not readily visible at ECG scales. Signal distortion can be seen on the R-wave for the cotton electrode due to the increased source impedance.

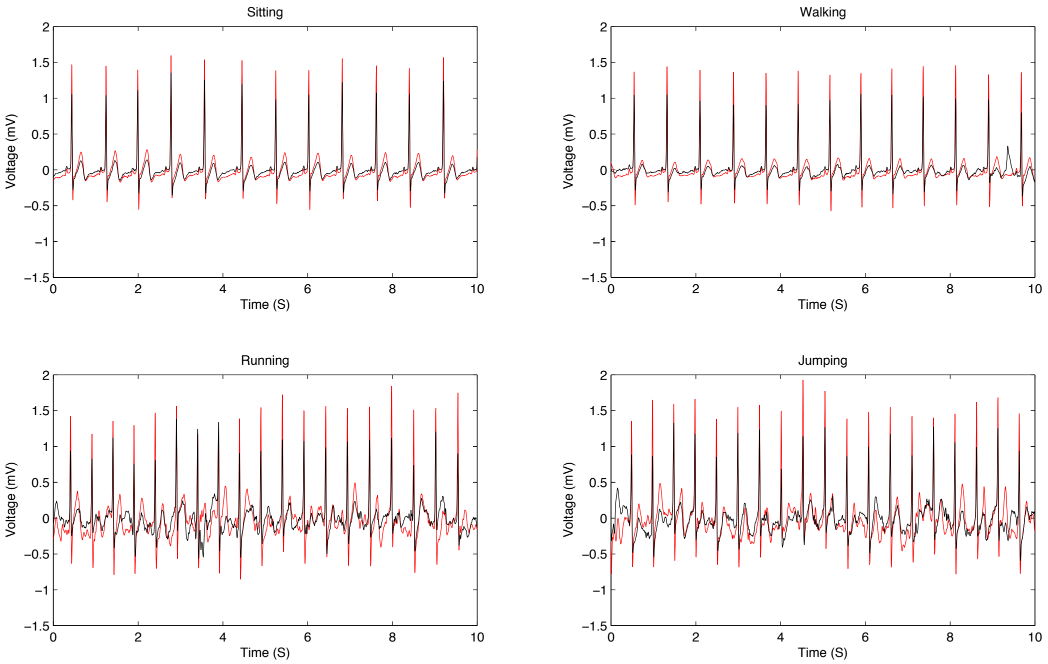

Figure 1.6: A 10-second comparison of noise and drift from wet Ag/AgCl (red trace) versus non-contact electrodes (black trace) during various activities, inducing motion and friction. The non-contact electrodes were fixed in a tight wireless chest band on top of a cotton shirt [14].

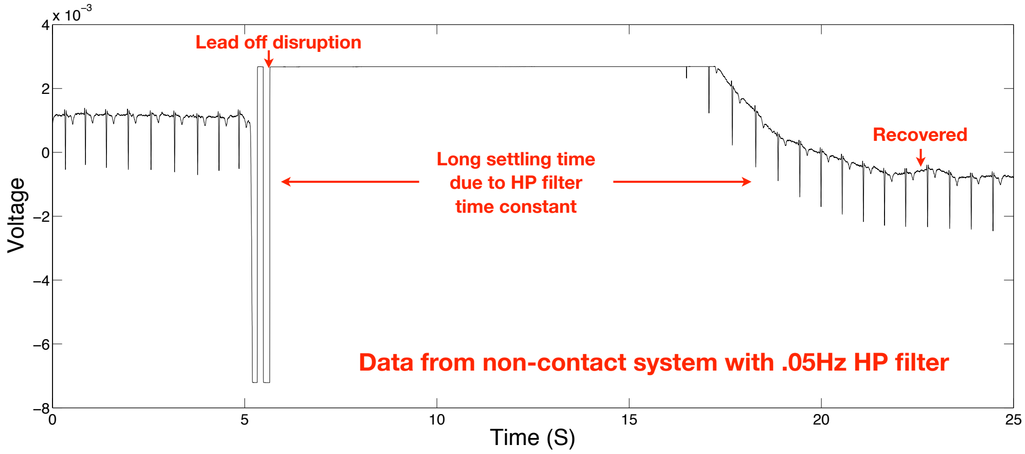

Figure 1.7: High impedance input node settling time. The lead was disrupted at t=5 sec. It takes more than 15 seconds for the trace to recover, showing the problem with recovery time for AC coupled instrumentation. The input was designed to have a cutoff of 0.05 Hz in line with ECG standards.

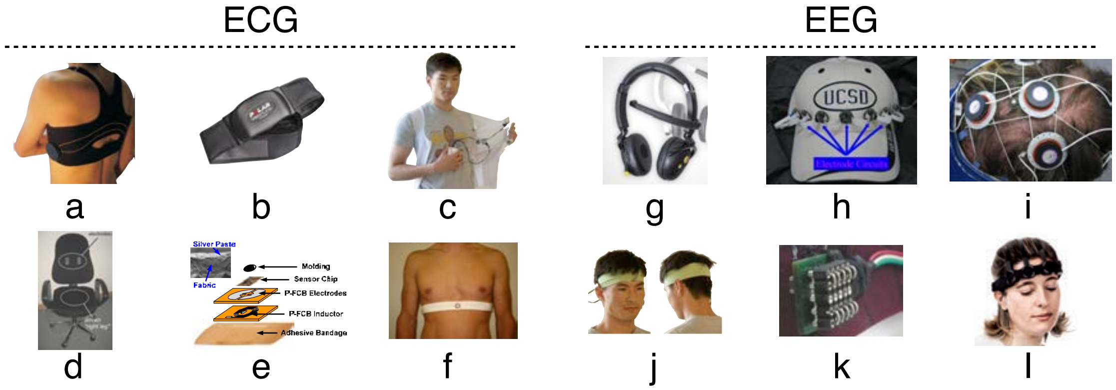

Figure 1.8: Dry and non-contact electrode systems. ECG - (a) chest harness [40], (b) Polar Heart Strap, (c) non-contact vest [14], (d) chair [41] [42], (e) wireless band-aid [20] and (e) dry chest strap [15]. EEG - (g) Neurosky single channel headset, (h) dry MEMs cap [43], (i) fingered dry EEG harness [15], (j) Dry/non-contact EEG headband [14], (k) Dry active electrode [44] and (l) ENOBIO wireless dry sensor.

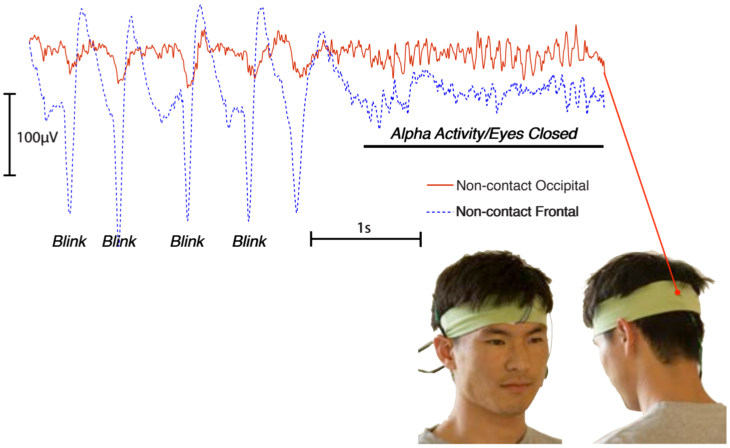

Figure 1.9: Non-contact EEG headband and data from both frontal and occipital electrodes [14].

Chapter 2

Properties of Dry and Non-contact Electrode Interfaces

2.1 Introduction

Wearable physiological sensors will become a key component of body sensor networks and wireless health systems. Brain and cardiac biopotential signals in the form of EEG and ECG are two critical health indicators that are directly suited for long-term monitoring using body sensor networks. Yet despite advancements in wireless technology and electronics miniaturization, the use of EEG/ECG has still been largely limited by the inconvenience and discomfort of conventional wet contact electrodes.

Extensive research efforts to date have been directed at building dry electrodes [20] [18] [22] [55] [3], insulated electrodes [8] [10] and non-contact electrodes [56] [14] [12] [13] [11]. These sensors do not require adhesives or gels, are more comfortable on the skin, and suitable for long-term monitoring.

In our experience, the nature of the electrode interface has by far, the greatest influence on both the signal quality and usefulness of the biopotential instrumentation system, more so than the electronics. While a good instrumentation circuit design is a necessary prerequisite, electrode behavior quickly becomes the limiting factor. Unfortunately, efforts to date have not sufficiently addressed the influence of the electrode material on the quality of signals from body sensor ECG/EEG devices [12] [11] [13].

Most characterizations of dry and non-contact systems have modeled the electrodes as simple circuit elements (eg. ideal capacitor [12]) which do not adequately predict the signal quality in actual use. In addition this may have lead to excessive efforts in optimizing at the circuit level, when in fact, it is the electrode interface that is the real limiting factor on dry/non-contact electrode systems.

To date, there has not been any systematic comparison of various dry electrode materials. In this paper, we analyze the noise characteristics of several common metallic, weakly conducting and insulating materials, including lead-free hot air surface leveled (HASL) PCB finish, silver cloth, latex, cotton, and soldermask. These materials represent a combination of readily available and skin friendly candidates to implement electrodes for BSNs. The HASL PCB finish and solder mask are two particularly convenient and inexpensive choices since they are a standard part of an electronics product. The soldermask, in particular, is a protected surface that should not degrade with usage. We characterize the electrical and noise properties of these electrodes and demonstrate that there are multiple options for non-adhesive and non-gel electrodes.

2.2 Skin-Electrode Modeling

The noise properties of biopotential electrodes are complex and the result of multiple different mechanisms [57]. It is the sum of the intrinsic thermal noise, excess noise from chemical reactions at the interface, biological noise from the body, and external noise from movement artifacts. In addition, the properties of the electrode and front-end electronics have a strong influence on how well a system can reject external interference such as 50/60 Hz noise. While literature exists on the noise properties of electrodes [4] [3] [58], especially for standard wet Ag/AgCl types, there is not any unified model that can fully predict the performance of the interface.

A model of a generic skin-electrode interface is shown in Figure 2.1. Electrically, it can be thought of as a series connection of parallel RC, each element representing a specific layer in the interface. Typically one high-impedance layer dominates the noise properties of the electrode (eg. dry skin, fabric) and influences its overall properties from electrode offset to immunity to long-term drift.

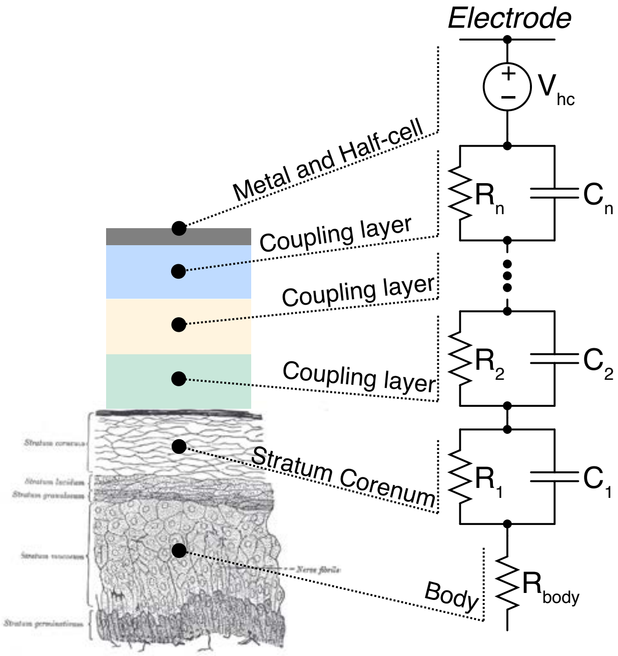

Figure 2.1: Electrode-skin model [59]. Electrical activity from within the body is coupled via different layers (eg. skin, hydrogel, Ag/AgCl), each with an associated resistance and capacitance (R_n,C_n) to the input of an amplifier. Typically the properties of one layer will dominate the behavior of the interface, including noise and offset (V_{hc}).

Figure 2.2 shows the equivalent circuit diagram with the noise generating sources for the electrode. The model is simplified by assuming that the skin-electrode interface is represented by a single R-C element representing the dominant layer [59].

The total overall noise noise in the model can be written as,

$$v_n^2(\omega) = v_{na}^2 + (i_{na}^2 + \frac{4kT}{R_s})(\frac{R_s^2}{1+\omega^2 R_s^2 C_s^2}) + v_{nb}^2 + v_{ni}^2 \tag{2.1}$$

where v_{na} is the amplifier's voltage noise, i_{na} is the amplifier's current noise, v_{nb} is the biological noise in the body, v_{ni} is the electrochemical noise at the interface, and i_{ne} is the thermal noise current of the electrode (for a slightly simpler expression than representing it as a voltage). This model assumes that an amplifier has infinite input impedance. For a typical CMOS input amplifier (R_{in} >1 TΩ), it is a safe assumption as even insulating electrodes have resistances of only a few gigaohms. The amplifier's input capacitance may also have an effect on the noise of electrodes with coupling capacitances that are of

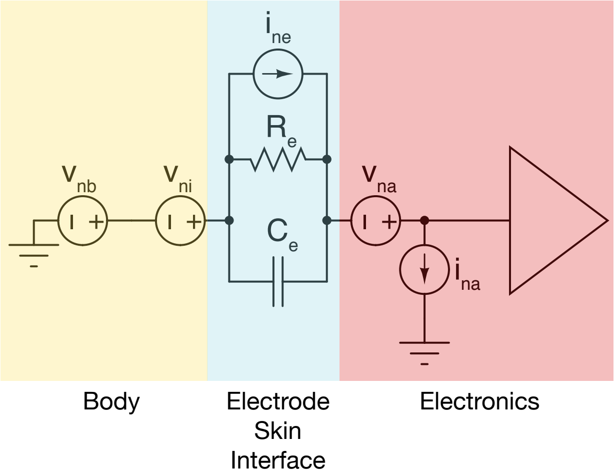

Figure 2.2: Electrode noise model, with the biological noise from the body v_{nb}, electrochemical interface noise v_{ni}, electrode thermal noise from the dominant layer i_{ne}, amplifier input voltage (v_{na}), and current (i_{na}) noise.

the same order [27], but the materials used in this paper were not affected.

The thermal noise aspect of the electrode is the most straight forward source to understand and compute. Unfortunately at the frequencies of interest for the typical biopotential, it is not usually the dominant mechanism. Electrochemical and biological noise is a large contributor at low frequencies, with a spectra that follows between $1/f$ and $1/f^2$ [57]. In addition, it is likely that excess noise is correlated with the resistance of the electrode.

Two things are important to note from this model. First, the layer contributes zero thermal noise if its resistivity is zero, as expected. Counter to intuition, however, the layer also contributes zero noise if the resistance is infinite (a perfect insulation). A purely insulting layer would couple entirely via it’s capacitance, which is a noiseless process. Small capacitances ($<$100 pF), however, will theoretically integrate an amplifierÕs input current noise and multiply the effect of the amplifierÕs voltage noise [27]. In practice, however, the specifications of a good amplifier are rarely the limiting factors for dry and even insulating electrodes.

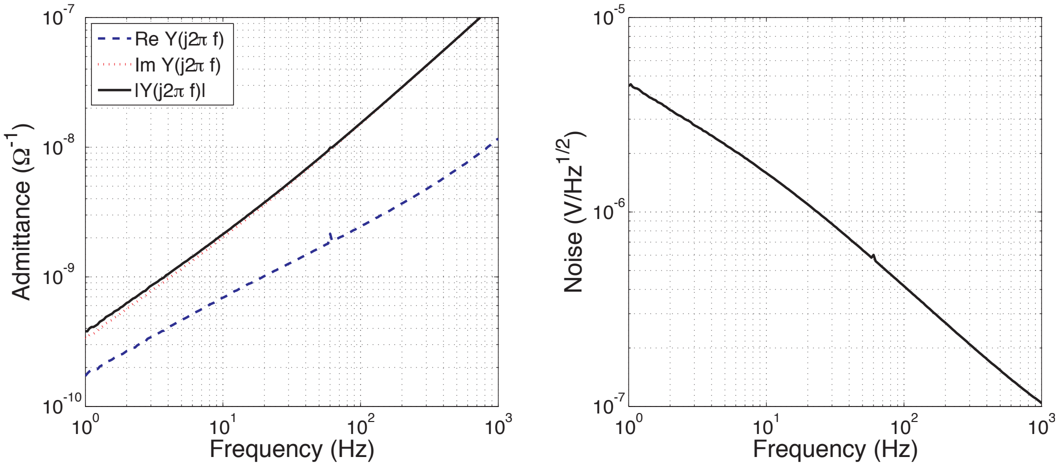

Figure 2.3: Measured admittances of a thick cotton sweater and it's calculated thermal noise spectra. Contrary to conventional wisdom, cotton is far from resembling an ideal capacitor and generates appreciable thermal noise.

2.3 Experimental Protocol

Fully modeling the interaction between the human body, skin, electrode, and electronics is the primary difficulty with characterizing various types of sensors. Attempts at bench measurements, even with simulated human bodies, often do not produce results that are consistent with observed performance on live subjects.

For the purposes of this paper, we measured the noise of the electrode on a live subject. A pair of differential active electrodes were placed on the forearm of the subject to capture all of the skin-electrode interface. The forearm is a convenient location since there is not any ECG or EMG artifact with a relaxed arm. In this paper the subject consisted of an 18 year old male. The experiments were conducted in a typical office environment. Care was made to move into areas of minimal 60 Hz interference. Two elastic cloth bands provided a uniform constant pressure to hold the active electrodes in place in order to prevent artifacts caused by slight motion or friction. An active ground was placed on the upper arm via a wet AgCl adhesive to minimize 60 Hz interference. The subject would allow approximately one minute for the electrodes to stabilize to prevent electrochemical drift from appearing in the collected data. Subsequently, the subject would slowly contract the muscles in the forearm to test the four channels for response. After these initial procedures to find the optimal placement of the active electrodes, the subject remained in a relaxed position with nominal muscle contraction for 6-minute intervals.

Between each measurement interval, the subject would allow muscles to contract and relax for a period of several minutes to avoid causing strain on the arm. However, despite these precautions, measurements taken in succession caused involuntary contractions of the striated muscle, causing repetitive and involuntary EMG artifacts to appear in the collected data. This phenomenon is known to occur when a muscle is held in the same position for a prolonged duration, causing it to become hyperexcitable and create a forceful contraction. Nevertheless, by analyzing the segments of data with the least amount of artificial motion artifacts, the effects of muscle contraction were compensated for.

A high-resolution wireless bioinstrumentation device was used to measure the data. The amplifier's gain was set to 40dB and digitized with a 16-bit ADC. Telemetry was transmitted wirelessly via Bluetooth at 1800Hz. The fully wireless and battery powered systems minimize external sources of interference.

As previously mentioned, a variety of electrode materials were used with sensors including a standard wet Ag/AgCl electrode, cotton, HASL, latex, silver cloth, and solder mask. The wet electrodes were noted to be the least comfortable, causing irritation to the subject when worn for longer durations. In general, the other electrodes were comfortable, left no skin irritation, and were easy to apply and remove.

A thin t-shirt made of 100% cotton was used to build a cotton electrode. This simulated a typical non-contact electrode, such as those that acquire ECG through clothing.

Another material tested was commercial laboratory latex from a protective glove was customized and wrapped around the active electrode. It maintained a higher degree of comfort than all other tested materials, with the exception of cotton. The latex is thin, which permits it to maintain a high coupling capacitance, even though latex is nominally very insulating.

Silver cloth (LessEMF.com, Argenmesh) is also an interesting electrode material. At first glance, it would appear that silver cloth is an ideal dry contact electrode material. It

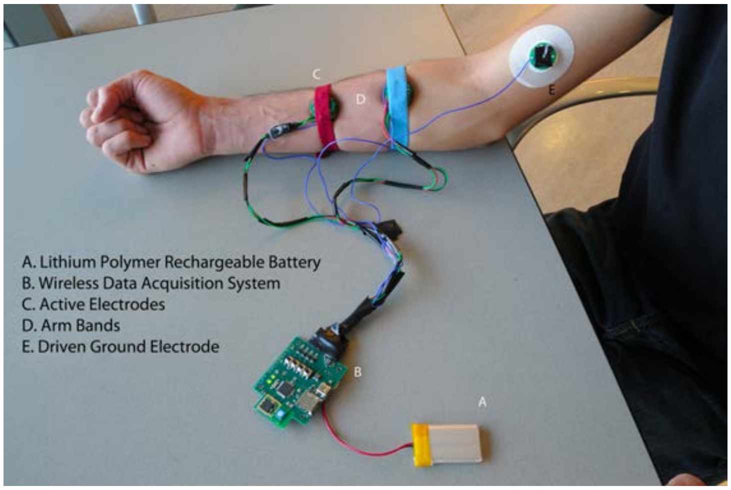

Figure 2.4: Electrode noise characterization setup. Two electrodes are mounted on the forearm to record the baseline noise for different types of electrodes under realistic conditions. A third electrode is used to ground the instrumentation.

inherits the stable electrochemical properties of silver (although not as good as Ag/AgCl), and is wearable and soft against the skin. It is also highly conductive like any metal. However, experiments show that silver cloth actually provides a very poor contact, likely due to the surface texture.

Solder mask from a standard PCB process was also tested since it is a protected surface that is easy to clean and standard with any electronics manufacturing process. Like latex, soldermask is interesting because it has a high resistance, yet may provide acceptable signal quality since the coupling capacitance is large.

2.4 Measured Results

Table I shows the measured electrode impedances for the six electrodes (on the subject’s arm) used in the experiment. As expected, conductive electrodes have relatively low resistances, whereas the insulating/non-contact electrodes have a much higher DC resistance. The capacitance, measured with a LCR meter, is also provided. Electrodes with thin interface layers have high coupling capacitance. The six materials represent a broad spectrum of possible electrode impedances.

Table 2.1: Measured Material Electrical Properties

Wet Ag/AgCl	$660\,\mathrm{k\Omega} \parallel 36\,\mathrm{nF}$
HASL	$6\,\mathrm{M\Omega} \parallel 5.2\,\mathrm{nF}$
Latex	$100\,\mathrm{M\Omega} \parallel 280\,\mathrm{pF}$
Silver Cloth	$40\,\mathrm{M\Omega} \parallel 900\,\mathrm{pF}$
Soldermask	$1.5\,\mathrm{G\Omega} \parallel 400\,\mathrm{pF}$
Cotton	$1\,\mathrm{G\Omega} \parallel 40\,\mathrm{pF}$

It is worth noting from the measured electrode impedances that the concept of a purely 'capacitive' non-contact electrode is an oversimplification and not usually encountered in practice. Even strong insulators such as cotton or soldermask have resistances on the order of a few gigaohms, much less than the input impedance of a CMOS amplifier, and are partially resistive within some of the ECG/EEG frequency bands. Likewise, 'conductive' electrodes still have resistances in the order of hundreds of kilo-ohms to mega-ohms. It is hard to achieve low contact resistances aside from vigorous skin preparation, which is impractical for wearable BSNs. In addition, the equivalent noise current ($1\,\mathrm{G\Omega} = 4\,\mathrm{fA/Hz^{1/2}}$) of these materials is much greater that the input current noise of a good CMOS amplifier ($0.5\,\mathrm{fA/Hz^{1/2}}$), which suggests that optimizing for current noise specifications, as previously thought [12], is not necessary for typical dry and insulating electrode designs. It is possible to add an explicit dielectric to the electrode, such as glass, to make the total DC resistance infinity, but the overall effect will be negligible since it will appear as an electrical short compared to the dominant RC interface layer.

Figure 2.5 shows the computed noise spectra from 3 minutes worth of sample data taken on the forearm along with the predicted thermal noise floor from the electrode's resistance and capacitance. The noise spectra was computed with MATLAB's *pwelch* function to estimate the PSD of the data sample.

With the exception of the silver cloth, the R-C thermal noise is accurate at computing the relative noise levels of the electrode, despite the fact that the magnitude of

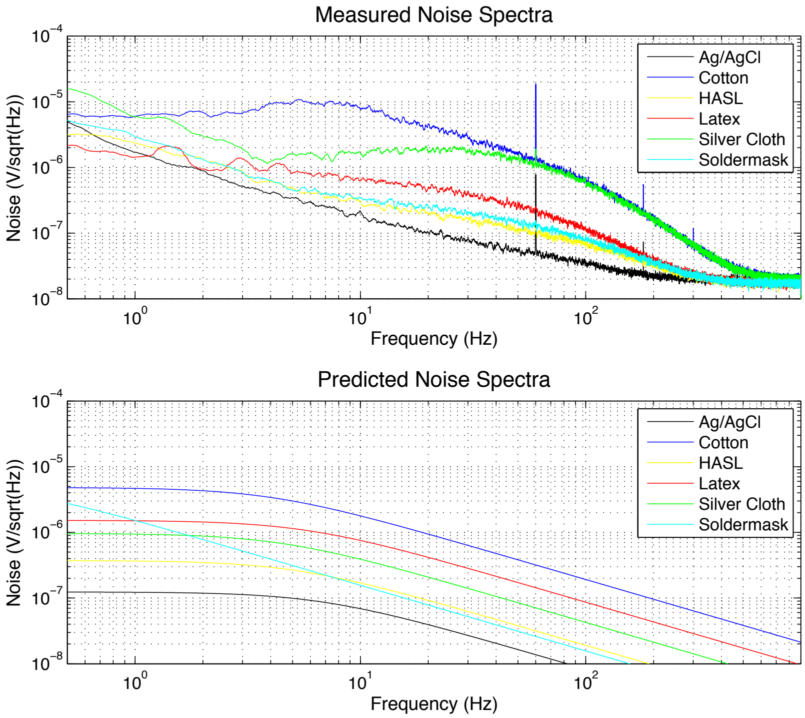

Figure 2.5: Measured and predicted noise spectra for each electrode type. The noise spectra was computed from a 3 minute segment of data taken on the forearm.

the predicted spectra is less than the measured one because the thermal noise model does not account for the excess interface noise. Low noise electrodes, such as the wet Ag/AgCl, seem to be entirely dominated by excess $1/f^2$ electrochemical noise and drift within the frequencies of interest for biopotential recordings. Insulating electrodes such as cotton or latex follow the thermal noise model much more closely since the thermal noise contributions are much larger, especially at lower frequencies and insulating electrodes may not have the same electrochemical noise/drift effects as conductive electrodes.

It is interesting to note that most electrodes have a $1/f^2$ noise spectra at lower frequencies, with the exception of cotton and silver cloth, which have much greater overall noise levels. For the Ag/AgCl electrode, it is theorized that this arises from electrochemical effects. For insulating electrodes, the theory suggests that the equivalent electrode capacitance shunts away the thermal noise with increasing frequency. At present, it still

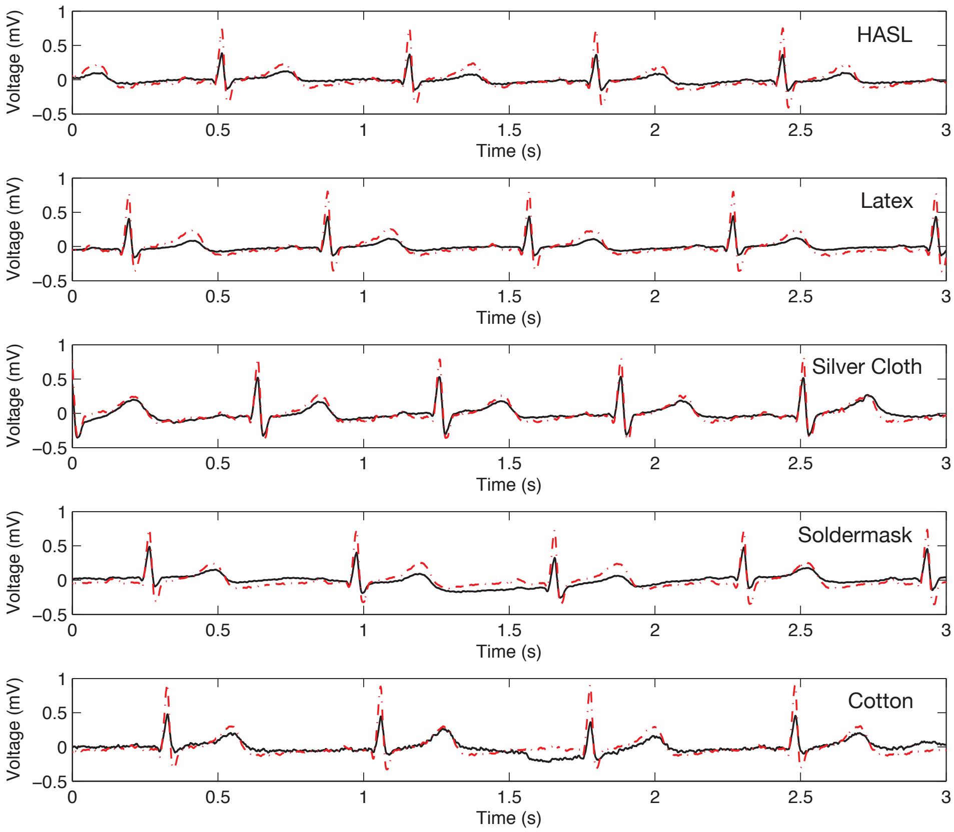

Figure 2.6: Sample ECG data taken with the various types of electrodes described in this paper. A reference ECG signal taken simultaneously with Ag/AgCl electrodes is overlaid in red. The bandwidth shown is from 0.5 Hz to 100 Hz.

appears that Ag/AgCl electrodes have the lowest low-frequency noise and drift. There also appears to be additional sources beyond thermal noise from approximately 10 to 100 Hz that is correlated with the electrode's impedance.

While the measured noise spectra does not exactly match thermal noise theory, the model provides a useful starting point and can predict the relative performance of the electrode. The exception is the silver cloth, which we had expected to perform similarly to the dry HASL electrode. One possible source of poor signal quality might arise from the sewed structure of the silver cloth which increases the propensity of rubbing between the electrode and the skin and decreases the surface contact area, both of which increase the amount of noise at the electrode interface.

2.5 Physiological Data

Sample ECG data was collected using the same materials as those used in the noise experiment and plotted in Figure 2.6. The red dashed lines represent the clinical wet adhesive Ag/AgCl electrode for reference, and the black lines represent the signal from the tested electrode material. Data for both the tested electrode and the Ag/AgCl electrode were taken simultaneously for a direct comparison. The amplitude of the ECG in the Ag/AgCl reference signal is slightly higher due to the offset in electrode positioning (Lead II).

The graphs indicate that HASL has potential for clinical applications, and show that the level of drift noise artifacts become close to the Ag/AgCl electrode after a minute of skin contact. Thin insulation such as latex or soldermask also work well, although the amount of low-frequency noise and drift may be prohibitive in some applications. Cotton and silver cloth performed the worst, as would be expected from the noise measurements. Both have excess low frequency drift as well as broadband noise and are very susceptible to motion artifacts.

It is interesting to note, however, that the noise performance is not extremely different at ECG scales. All materials are certainly more than sufficient for R-R beat detection. However, the amount of noise becomes much more significant for EEG applications due to the lower signal amplitude.

For clinical ECG use, stability at low frequencies is critical to distorting the morphology of the signal. Many non-Ag/AgCl electrodes often have large amounts of low frequency noise, react poorly to changing skin conditions (eg. sweat), and are prone to overloading under movement. High-pass filtering is effective at stabilizing the baseline and amplifier’s response, but distorts the shape of the ECG - a common occurrence with current non-contact sensor designs [59]. EEGs which have different frequency response requirements may be more tolerant of more aggressive high-pass filtering, but have much more stringent overall noise requirements.

2.6 Discussion

This paper provides several useful options for implementing future body area physiological sensors and provides a simple test protocol to measure and compare the noise of new electrode materials. Several example conductive and non-conductive materials were tested. Although excess interface and biological noise render it impossible to fully predict the behavior of electrodes from analytical models, empirical data suggests that overall noise levels are strongly correlated with electrode impedance within the frequencies of interest, not just the DC resistance level. For example, soldermask and cotton have extremely high resitivity, (1 GΩ), orders of magnitude higher than a standard Ag/AgCl electrode. Nevertheless, soldermask was able to provide relatively low-noise signals due to its high capacitance. Cotton, however, was noisy within ECG/EEG frequencies due to its low capacitance.

For dry and non-contact electrodes where it is impossible to achieve a low contact resistance, it may be possible to achieve a high signal quality by *maximizing* both the electrode's resistance and capacitance. Excellent signals, particularly for ECG, may be obtained with simple materials including bare lead-free PCB. Contrary to what may be expected from their insulating nature, latex and soldermask provided signals that were quite comparable to a dry metal electrode. Furthermore, acceptable signals may be obtained with comfortable materials such as cotton. Interestingly silver cloth performed quite poorly and is no better than regular cotton fabric.

It is expected that non-traditional electrode materials will become increasingly important for medical and non-medical use, especially given the importance of subject comfort for wireless, wearable sensors.

Chapter Two is largely a reprint of material published in the 2011 IEEE Body Sensor Networks Conference: N. Gandhi, C. Khe, D. Chung, Y. M. Chi and G. Cauwenberghs, "Properties of Dry and Non-contact Electrodes for Body Sensor Networks," *IEEE Body Sensor Networks*, 2011. The author is the primary author and investigator of this work.

Chapter 3

A Non-Contact Electrode with Onboard Filters and Digitizers for High-Density Physiological Sensing

3.1 Introduction

The use of biopotential measurements is an integral tool in both research and clinical settings. Electrical signals on the body's surface like electrocardiograms (ECG), electroencephalograms (EEG), and electromyograms (EMG) provide useful information regarding the physiological state of the subject. Typical recording systems still primarily use wet type electrodes comprised of a metal plate on an adhesive sheet with the skin-electrode interface conducted through a gel paste. Consequently, preparation for each recording is non-trivial and places practical limits on their use for high density, long term, wearable biopotential recording systems.

Capacitive type electrodes that do not require direct contact are attractive in body sensor applications since they require a minimal of preparation and impose the least impact on the end user. Early work [8] [10] have shown efficacy in resolving EEG and ECG type signals through capacitive coupling. Recent developments in microelectronics have revived interest in this type of biopotential sensing.

Prance et. al [11] [60] demonstrated the use of modern integrated amplifiers

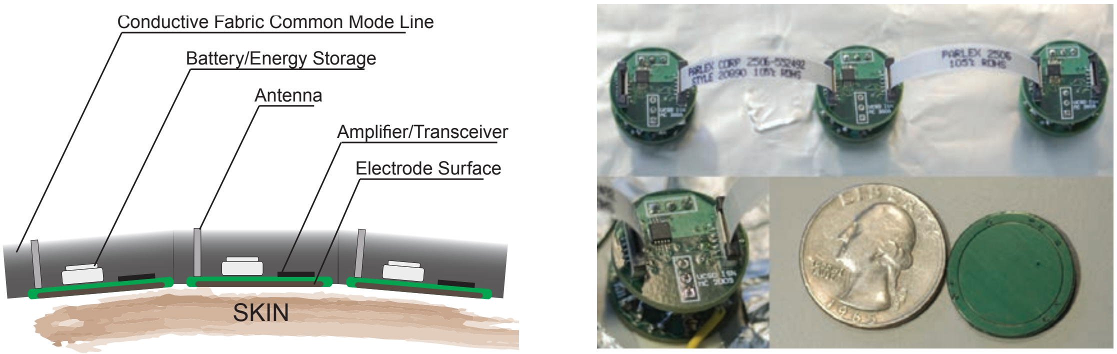

Figure 3.1: Wearable biopotential sensor networks monitoring. (Top) Conceptual high-density integration of non-contact biopotential sensors in a wireless body network embedded in conductive fabric, serving as active signal reference. (Bottom) Realized wired network of non-contact sensors, with daisy chain digital output.

to achieve the ultra high input impedances necessary to resolve signals through small coupling capacitances. Other contactless sensor approaches [61] [34] [62] have successfully met or exceeded the performance of gel electrodes in ECG applications. However, to date, the full potential of capacitive biopotential sensing in a high spatial resolution wearable body sensor network has not been realized.

In this paper, we present a new active electrode architecture particularly suited for high resolution biopotential sensing. The compact coin sized sensor features a common-mode noise suppression front-end with a high differential gain. A single conductive sheet, spanning the area of the body being sensed, serves as a common-model signal reference for all sensing nodes, actively driven to the average of each sensor node. Finally, the electrode consumes a minimal of power and has a easy to use fully digital signaling interface.

Fig. 3.1 illustrates the concept of a fully wireless, non-contact body sensor network for high-resolution biopotential mapping, and the current realization of a wired network with daisy-chain digital readout presented here. This paper focuses on the design of the non-contact sensor with active common-mode suppression through a single conductive sheet extending over the network. The ability to integrate these networks in lightly conductive fabric make it appealing for non-obtrusive integration in wearable body sensor networks.

3.2 Non-Contact Sensor Design

3.2.1 Electrode Construction

Each sensor (Fig. 3.1) consists of two small round electrically connected standard printed circuit boards the size of a US nickel coin. The upper board contains a 16-bit analog-to-digital converter and voltage reference. Unlike traditional electrodes that output a single analog signal, interfacing is facilitated through two miniature 10-wire ribbon cables on each side which provides power along with the digital clock, control and data lines.

The ADC output from each board is a serial data stream which is shifted in a daisy chain [12] from board to board to the end of the chain which connects to a custom USB data acquisition interface. This connection scheme minimizes the amount of cabling required across the sensor network, where the total connection length scales with the number of sensors and the average distance between sensors.

Biopotentials are sensed through a $228\,\text{mm}^2$ copper fill insulated by solder mask on the lower board, which is shielded from external noise by the outer copper ring and a solid metal plane directly above the electrode. The amplifier circuit is placed directly on the top surface of the lower board and output an analog signal which is digitized by the upper board.

3.2.2 Sensor Amplifier Circuit

Figure 3.2 shows the analog front-end schematic for a single electrode channel consisting of two operational amplifiers and associated passive components. The first operational amplifier (OA1) provides differential gain and drives the common line. The second operational amplifier (OA2) serves as a buffer to drive the active shield and bootstraps the biasing network.

Biopotentials are coupled to the non-inverting input of OA1 through a capacitance, C_s, formed by the electrode and the skin. For this type of capacitive sensing, the input

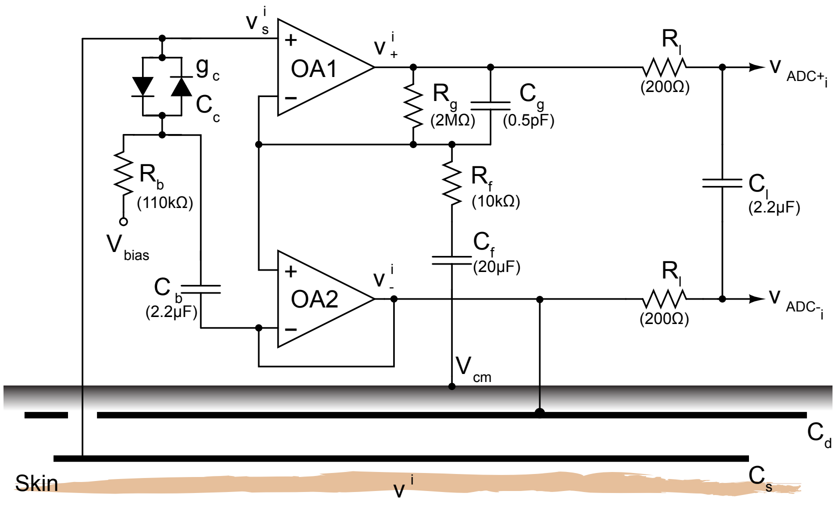

Figure 3.2: Schematic of electrode analog front end amplifier circuit. All electrodes in the network are joined at V_{cm}, through a single conductive layer spanning the network.

impedance of the sensor input must be kept extremely high since any finite input resistance forms a high pass filter with the coupling capacitance, shunting the signal. For the low frequencies (0.1 Hz-100 Hz) in physiological measurements with the small coupling capacitances (0.1-10 pF) in non-contact capacitive coupling, the input resistance must be in excess of 1 TΩ. In addition, it is also desirable to minimize any parasitic input capacitance C_{in}, since it further attenuates the body signal v^i of sensor i in the network as it is received at the amplifier input:

$$v_s^i = \frac{C_s^i}{C_s^i + C_{in}^i} v^i. \tag{3.1}$$

Although the FET input amplifier (LT6078) provides low noise operation at low power consumption with high input impedance and low input capacitance, it requires an input biasing network to provide a DC current path to counteract leakage currents and fix the DC input voltage to a mid-rail level for maximum output signal range. Using a simple resistive bias network is impractical from a reliability and noise standpoint. Although a biasing resistor can be bootstrapped to the required resistance, minimizing its current noise contribution requires an impossibly high value (>1 TΩ). Instead, input biasing was accomplished with two back-to-back diodes to V_{bias} through a 100 kΩ resistor, R_b, at DC and provide a path for the amplifier's input bias current in a similar scheme to [60], but with the addition of a second diode for protection and clamping. To mask the diode's parasitic capacitance and conductance, C_b (2.2 μF) bootstraps the input for input frequencies higher than $1/2\pi R_b C_b$ Hz, thus preserving the amplifier's high input impedance while achieving lower noise levels than what is possible with a purely resistive bias.

Unlike most previous capacitive electrode amplifier designs [60] [11] [62], each electrode serves as a self-contained channel of a distributed biopotential sensor network connected through the common line, V_{cm}, rather than a simple voltage buffer. The output of each electrode is the amplified and filtered difference between the local biopotential, and its spatial and temporal average over the aggregate of electrodes, actively driven and communicated over the shared V_{cm} node.

In each electrode, the non-inverting node of OA1 follows the capacitively coupled signal from the body. This sets V_{cm} to the average of the potentials v_s^i as seen by each electrode, averaged through the passive voltage mixing network formed by R_f and C_f:

$$V_{cm} \approx \frac{1}{N} \sum_{j=1}^{N} v_s^i \tag{3.2}$$

where N is the number of sensors connecting to the V_{cm} node. The sensor circuit amplifies and filters the difference between v_s^i and V_{cm}, hence performing global common-mode subtraction:

$$v_+^i - v_-^i = A_{fg}(j\omega)\ (v_s^i - V_{cm}) \tag{3.3}$$

where

$$A_{fg}(j\omega) = \frac{j\omega C_f R_g}{(1 + j\omega R_g C_g)(1 + j\omega R_f C_f)} \tag{3.4}$$

provides a band-pass response with mid-band gain of R_g/R_f =46 dB over a $1/2\pi R_f C_f$ =1 Hz to $1/2\pi R_g C_g =$ 100 Hz bandwidth. For a high resistance fabric used as the common-mode connector, depending on the value of the sheet resistance relative to R_f, the common-mode signal V_{cm} in varies spatially, and the network produces output signals that are spatially as well as temporally high-pass filtered across the sensor array.

For true common-mode components in the input, the current through R_f is zero, so that common-mode signals are absent in the amplified differential signal at the ADC input. Hence, the common mode rejection ratio (CMRR) of the sensor is relatively insensitive to component matching and the amplifier's loop gain. However, the CMRR is critically sensitive to gain variations induced by non-contact capacitive shunting of the body signal at the amplifier input. Variations in distance between sensors and the body surface, as well as variations in dielectric properties of texture, cause variations in coupling capacitance C_s that introduce large common-mode gain errors according to.

An active shield guards the input from contamination from externally coupled noise. The active shield driven by a buffered version of the input signal has been shown to be effective [11] [34] [12] in guarding the amplifier input without introducing addition loading to the input. Here, the second amplifier, OA2, drives this shield (C_d) and also provides a low-impedance source to drive the differential ADC inputs, with additional anti-aliasing low-pass filtering over $1/2\pi R_l C_l = 100\,\text{Hz}$ bandwidth provided by C_l and R_l.

The net signal at the ADC input, including the effect of noise sources in the amplifiers and input diodes, is approximately given by:

$$\begin{aligned} V^i_{ADC} &= V^i_{ADC+} - V^i_{ADC-} \\ &= A^i(j\omega)\,(v^i + v^i_n) - \frac{1}{N}\sum_{j=1}^{N} A^i(j\omega)\,(v^j + v^j_n) \end{aligned} \tag{3.5}$$

with net channel gain:

$$A^i(j\omega) = \frac{1}{1 + j\omega R^i_l C^i_l}\,\frac{A^i_{fg}(j\omega)}{1 + \frac{1}{C^i_s}\left(C^i_{in} + \frac{g^i_c(1+j\omega\tau^i_c)}{j\omega(1+j\omega\tau^i_b)}\right)} \tag{3.6}$$

and with input-referred noise:

$$\begin{aligned} v^i_n &= \frac{C^i_s + C^i_{in} + C^i_d + C^i_c + \frac{g^i_c}{j\omega}}{C^i_s}\,v^i_{n1} \\ &+ \left(\frac{C^i_d + C^i_c\left(\frac{1+j\omega\tau^i_c}{1+j\omega\tau^i_b}\right)}{C^i_s}\right) v^i_{n2} \\ &+ \frac{1}{j\omega C^i_s}\,(i^i_{n1} + i^i_{nb}) \end{aligned} \tag{3.7}$$

where v^i_{n1} and v^i_{n2} are the input-referred voltage noise of amplifiers OA1 and OA2 respectively, i^i_{n1} is the input current noise of OA1, and i^i_{nb} is the current noise contributed by the input diodes. The small signal conductance of the double diode input clamp is represented by g_c^i and its associated capacitance by C_c^i. The time constant of the bootstrapped bias network, $\tau_b^i = R_b^i C_b^i$, and the input clamp, $\tau_c^i = g_c^i/(C_{in}^i + C_s^i)$, also appear in the gain and noise expressions.

From the gain equation, the effect of bootstrapping of the input diode serves to mask the diode conductance, g_c, by a factor approximately τ_c^i/τ_b^i as well as canceling its parasitic input capacitance, C_c. This is useful due to the relatively high capacitances associated with the low leakage diodes used for minimizing current noise. It is also desirable to use C_b to minimize the dynamic voltage excursion across the input diode to maintain its low conductance bias point to avoid distorting the signal for larger input swings.

Secondly, while the use of this network largely eliminates the parasitic conductances at the input, it also serves to couple excess voltage noise back to the input node, hence increasing the overall noise levels. Each parasitic shunt conductance at the input node directly increases the net effect of v_{n1}^i by a factor set by the ratio of the the shunt conductance versus the sensor capacitance. The use of the OA2 for shield buffering also couples noise from v_{n2}^i through C_d^i and C_c^i. From a noise perspective, it is still advantageous to minimize each of these parasitic terms, even though feedback and bootstrapping can be used to minimize their impacts on the gain term.

The effect of input current noise, however, is dependent only on the size of the sense capacitance, C_s. For weak sensor coupling, the current noise will dominate the overall noise expression and set the fundamental noise floor for signal detection.

Finally, a source of error is contributed by the C_{in}^i/C_s^i mismatch, resulting in a variable gain reduction from A_{fg} in each channel. For higher gain as well as common mode rejection, future version will include a compensation network to cancel the effects of amplifier input capacitance.

3.2.3 ADC

A 16-bit differential ADC (TI ADS8318) was used to acquire the amplified and filtered signal from the electrode. As previously mentioned, the ADC digital data lines are connected as a daisy chain shifting serial data from the end of the sensor chain back

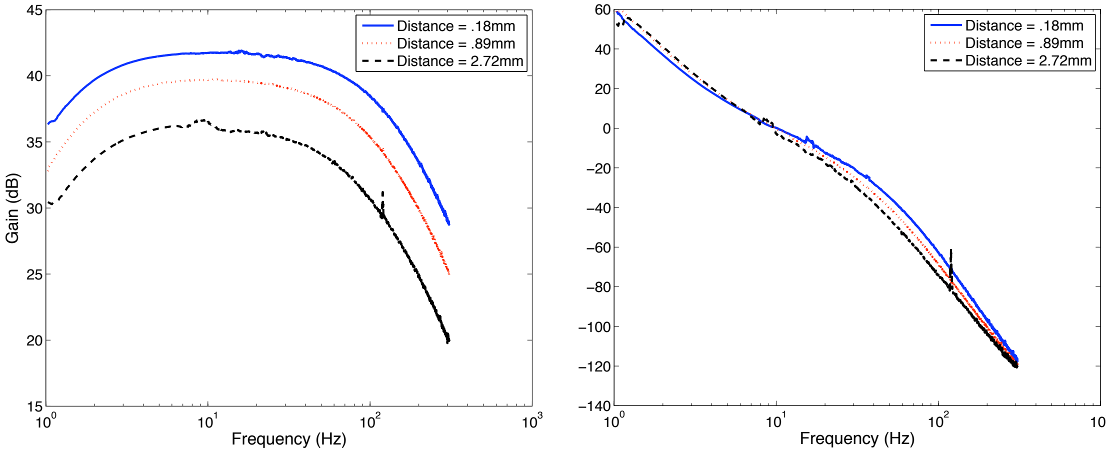

Figure 3.3: Sensor differential gain (bottom) and phase (bottom) at different distances.

to the host data acqusition module. A common clock and chip select line synchronizes the conversion and transfer of data at a sample rate of $1ksps$.

3.3 Experimental Results

A prototype network of eight sensors was implemented. All results presented below are obtained with two sensors, implementing two-point differencing. The common mode line is implemented with a single wire.

3.3.1 Sensor Gain

Sensor gain is dependent on the ratio of the skin-electrode capacitance versus the parasitic amplifier input capacitance, resulting in decreased gain as the sensor is placed further from the surface of the skin. To characterize the performance of the sensor at various distances, two sensors were coupled to two metal planes across glass dielectrics of varying thickness.

A differential test frequency sweep was applied to the two metal plates from a function generator. The sensor output, along with the test input were recorded through the ADCs, allowing the gain and phase to be measured.

The gain is shown in Fig. 3.3 and decreases as the sensor is placed more distant

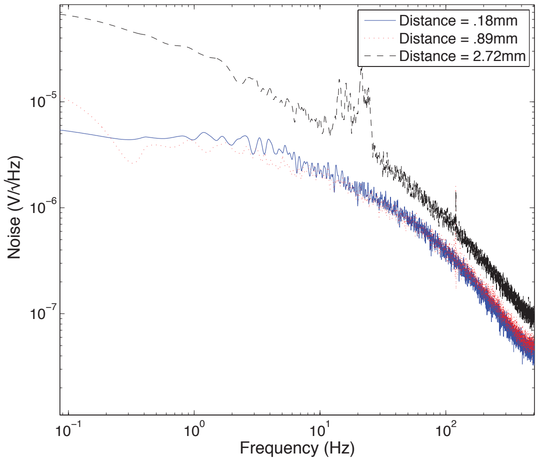

Figure 3.4: Sensor input referred noise spectrum at different distances.

from the signal source, as expected. The phase of the transfer function is virtually invariant over sensor distance, indicating that sensor input has a sufficiently high input resistance that the only signal attenuation is due to the parasitic input capacitance.

3.3.2 Noise

Noise levels were measured for a two channel system by placing the two electrodes face-to-face with a glass dielectric of different thickness, thereby shorting the inputs, in a similar manner as before and recording the resultant output noise as measured by the ADC. The input referred noise spectrum is shown in Fig. 3.4 and is computed by taking the total output noise spectrum and dividing by the previously found mid-band gain at the same separation distance. Total measured in-band input referred noise is approximately 14 μV_{rms} for both the .18*mm* and .90*mm* sensor separation distances and degrades significantly for further sensing distances.

Reducing the level of input noise can be accomplished by having a lower input leakage current as mentioned in the previous section. At present, the diodes used have a total leakage current of approximately 6 pA, much larger than the input bias current of the amplifier resulting in 1 fA/Hz$^{1/2}$ of current noise. An complete integrated solution with on-chip biasing techniques would significantly improve the noise performance.

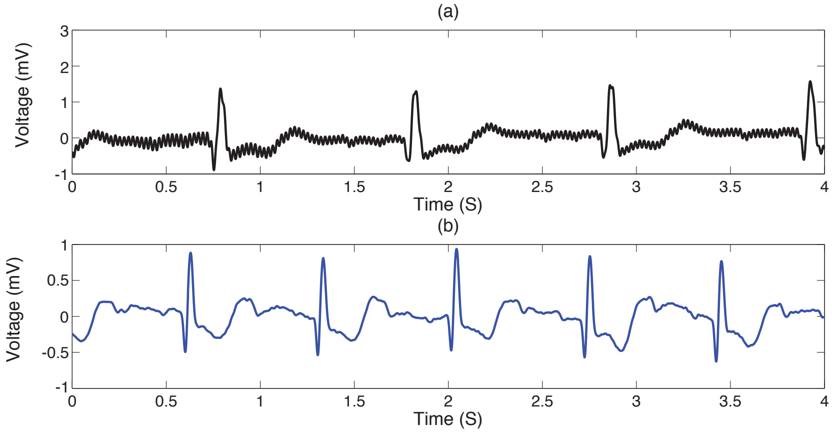

Figure 3.5: ECG recording taken over subject's chest with non-contact sensor through a cotton shirt (a) and directly over the skin's surface (b). In both cases the signal ground was floating with respect to the body.

3.3.3 Power Consumption

Overall power consumption for each electrode including amplifier and ADC is 285 μA at 3.3 V. Power consumption is dominated by the amplifier which consumes a quiescent current of 100 μA for the two device package. This is more than ten times more power efficient than previously reported [12]. The power requirement of only 940 μW at a single 3.3 V supply along with the fully digital interface makes it easy to interface a large scale network of these electrodes with a low power wireless module or a simple notebook powered USB system.

3.4 Physiological Recordings

Sample recordings of ECG are shown in Fig. 3.5 and are made from a two electrode test setup. One sensor was placed above the heart while the second was placed over the opposing rib cage and the differential voltage is recorded. A clear ECG is observed when the sensor is placed directly above the skin's surface. When the recording is made over a shirt, some 60 Hz line noise is introduced as a result of capacitive mismatch due to the larger separation distance and corresponding smaller coupling capacitance.

Future introduction of an improved active shield that bootstraps the input with gain is expected to significantly reduce the capacitive mismatch common-mode error and eliminate residual line noise.

3.5 Discussion

A small network of active capacitive electrodes for low-power non-contact biopotential sensing has been implemented and demonstrated. While the effect of capacitive gain errors due to variable strength coupling in non-contact sensing introduces common-mode errors in the received signals, future work involving active bootstrapping is expected to mitigate these effects.

This work represents the first attempt in this research to construct a non-contact sensor, and as evident from the results, it exhibits significant performance issues. In particular the signal quality is quite poor, and the input bias is often unstable - easily leading to amplifier saturation. Problems with passive grounding and wired instrumentation result in signals usually contaminated with 60 Hz interference.

Lessons learned in this first project were applied towards the subsequent iterations of the non-contact sensor resulting in the design of a wireless discrete-component version with a much simplified front-end circuit architecture, but significantly superior performance. In addition the difficulties with input biasing and input impedance lead to the development of an integrated front-end, also described in subsequent chapters.

Chapter Three is largely a reprint of the 2009 IEEE Body Sensor Networks paper: Y. M. Chi, S. R. Deiss, and G. Cauwenberghs, “Non-contact Low Power EEG/ECG Electrode for High Density Wearable Biopotential Sensor Networks,” *IEEE Body Sensor Networks, 2009.* The author was the primary author and investigator of this work.

Chapter 4

Design of Low-Cost, High-Performance, Wireless Non-contact ECG/EEG Sensor Array

4.1 Introduction

Wireless health, driven by an aging population and increasing technological sophistication, is expected to be a key driving force towards improving the quality of life. Advancements in embedded electronics and wireless technology have made inexpensive and wearable physiological monitoring devices a reality. Combined with the appropriate data and signal infrastructure, mobile monitoring devices have the potential for significantly improving time timeliness and accuracy of medical diagnostics.

Of all the numerous parameters that can be observed, brain and cardiac biopotential signals in the form of EEG and ECG are two critical physiological indicators that are directly suited for long-term wireless health monitoring. Currently the standard wet adhesive electrode remains universally used for ECG/EEG applications in both clinical and ambulatory environments. For home use, however, the standard adhesive electrode is often cited as a major inconvenience, leading to low usage compliance - significantly reducing the effectiveness of outpatient monitoring. Common problems include skin irritation from the electrolytic gels and discomfort from the adhesives. Likewise, EEG

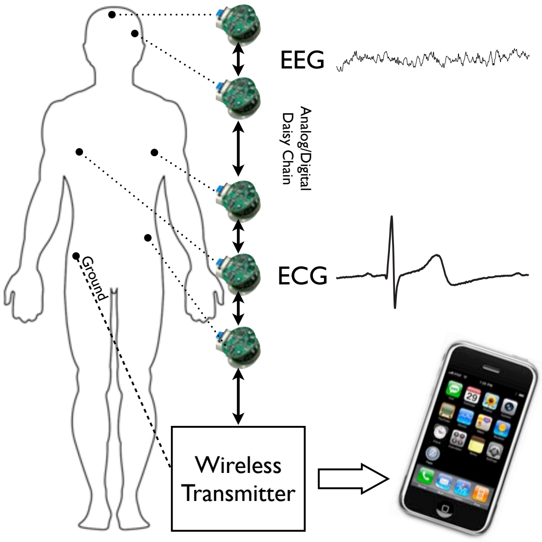

Figure 4.1: Concept of the wireless non-contact physiological monitor. The electrodes are embedded inside a wearable harness. Data from the electrodes is aggregated by a base unit for storage or local telemetry to a wireless portal

monitoring beyond a limited number forehead electrodes is impractical simply due to the difficulty of applying and maintaining scalp electrodes. To realize the true potential of future wireless health systems, a less obtrusive sensor is needed to match the advancements made in wireless technology.

As an alternative, dry electrodes [12] [13] have started becoming much more common-place. However, like wet electrodes, dry electrodes still require direct electrical and physical contact to the skin. In addition, dry electrodes, which do not have the benefit of a conductive gel, are much more sensitive to the condition of the skin and are highly susceptible to motion artifacts.

In contrast to wet and dry contact sensors, non-contact non-contact electrodes do not require an ohmic connection to the body. This offers numerous advantages since non-contact electrodes require zero preparation, are completely insensitive to skin conditions and can be embedded inside a garment for a completely unobtrusive, patient-friendly system. While the concept of non-contact biopotential sensors is not new, with the first working device reported decades ago [8], a practical device for patient use has yet to materialize. More recently, several authors have presented results from designs utilizing the latest in commercially available discrete low noise amplifiers [12] [11] [63], including some wireless designs [61].

Over the years, many clever designs have appeared, some proprietary. However, no technology has truly progressed beyond the lab prototype stage and into commercial use. In addition, general knowledge about non-contact sensors, including design techniques are not fully available in the literature. In this paper, we attempt to address these shortcomings by presenting the full designs, including all the relevant details in the analog front-end, for a high-quality, non-contact, wireless ECG/EEG monitor. In addition, we characterize the system-level performance by directly comparing the non-contact electrode against traditional, clinical Ag/AgCl electrodes and show that they have the potential of approaching the performance of wet electrodes in some applications. This work builds on the paper previous published in the Wireless Health 2010 conference [14], which outlined the design and basic experiments for the non-contact ECG/EEG system. This paper adds additional key theory, measurement and implementation details on the non-contact sensors and additionally describes the first report of a completely wireless, fully self-contained non-contact ECG monitoring module.

4.2 System Design

A full schematic depicting the wireless, non-contact sensor system is shown in Figure 4.3. Each electrode contains an onboard amplifier, filter, buffer and connects to the wireless base unit. All of the electrodes, including the active ground, can be fully insulated. Since no galvanic connection is present and the device is battery powered, the risk from electrical failures and shock is minimal.

4.2.1 Non-contact Active Electrode Overview

The basic design and function of non-contact electrodes has been well explored and documented in the literature, with earliest working devices dating back to 1968 [8]. Nevertheless, the use of wet Ag/AgCl electrodes remain ubiquitous for medical and clinical usage.

Figure 4.2: Picture of the non-contact, non-contact electrode. The sensor is manufactured on a standard PCB, which contains the amplifier circuits on the top and the sensing plate on the bottom.

Common problems associated with non-contact, non-contact electrodes in uncontrolled, non-laboratory usage include:

1. Noise - Non-contact electrodes exhibit a much larger intrinsic circuit noise floor.
2. Motion Artifacts - Even slight amounts of motion/friction saturate the signal and the electrode by nature does not adhere to the body.
3. Interference Pickup - The sensitive amplification circuitry of the electrode is very susceptible to 50/60 Hz line noise.
4. Complexity - The need for non-standard and relative specialized components directly on the electrode, especially when compared against the standard disposable electrode.

In general, these problems can be categorized as arising from two sources. The first consists of circuit design, accounting for the issues with complexity and intrinsic noise. The second is largely due to mechanical implementation and account for interference and motion artifacts. Through our experience, these problems with non-contact sensors can be significantly mitigated with careful design. The details will be explained in full throughout this paper.

We have developed a simple, repeatable, robust and relatively inexpensive method for producing high quality non-contact electrodes. The physical substrate of the electrode is a standard PCB. Figure 4.2 shows a close up of the latest generation of our non-contact

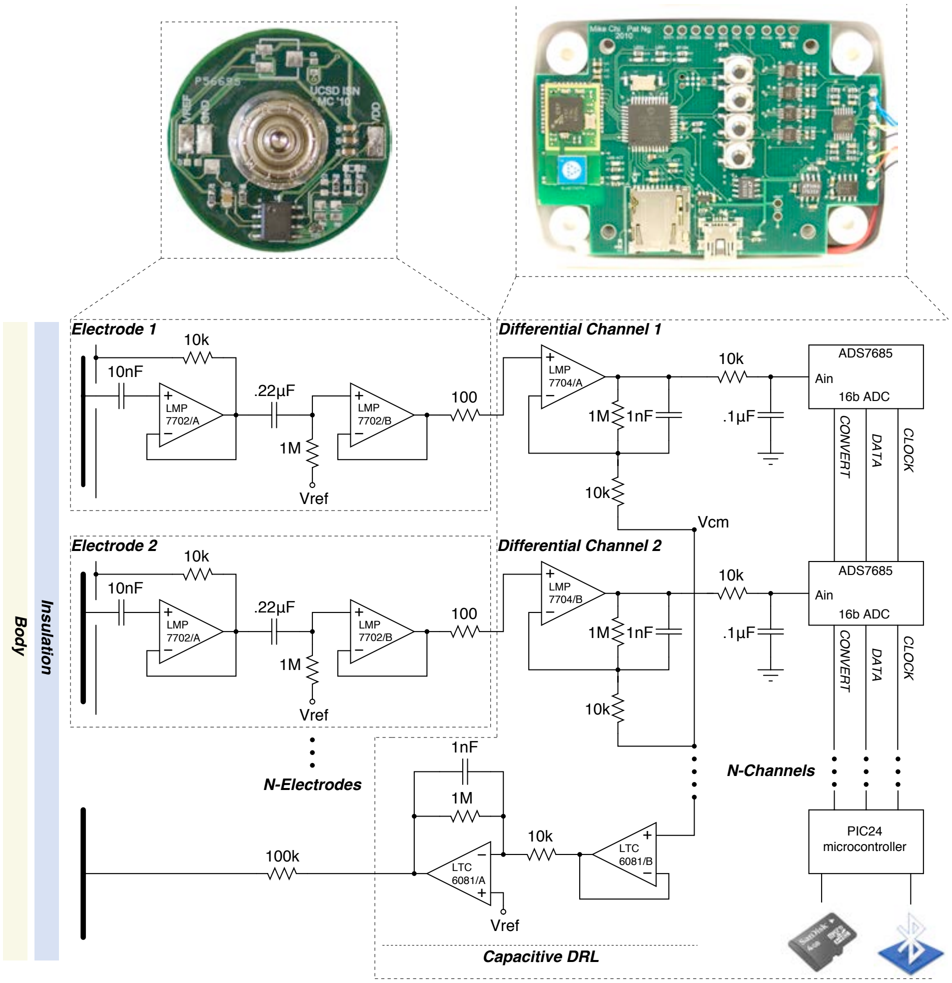

Figure 4.3: Full schematic of wireless ECG/EEG system. The non-contact electrode PCB contains the front-end amplifier. Differential gain, digitization, active grounding and digital processing/wireless is contained on separate base unit.

electrodes. As before, amplifier circuits to buffer the weak signal acquired electrode are housed on the top. In the center, a snap connector is used to provide mechanical stability, as well as provide compatibility with standard medical/research instrumentation (additional power, reference and ground lines are needed as well). An active shield formed by the inner plane of the PCB and a ring around the sensing plate protects the electrode from external interference. The overall dimensions of the sensor is slightly larger than a US quarter.

The bottom plate of the electrode is a solid copper fill, which forms a parallel plate capacitor with the body to couple biopotential signals. In this version, the copper fill is not insulated with soldermask, allowing the sensor to optionally function as a dry contact electrode. As a dry-contact sensor on the skin, the signal is virtually indistinguishable from clinical wet Ag/AgCl electrodes. However, this paper will focus on the use of this sensor as a non-contact electrode, sensing signals through insulation such as fabric.

4.2.2 Non-contact Active Electrode Circuit Design

In contrast to previous reported implementations [12] [11] which involved a combination of uncommon components (such as the expensive, electrometer-grade INA116), capacitance cancellation schemes and proprietary/unpublished designs, we have built a very high quality active non-contact electrode based around a common, inexpensive and widely available amplifier, the National Semiconductor LMP7702. Only three resistors and three capacitors are required to complete the device.

The LMP7702 is a CMOS opamp in a dual SOIC-8 package with an input structure suitable for ultra-high impedance sensors. Although on paper, the current-noise is specified as ten times greater than the INA116, we have found the noise performance to be comparable, if not better in practice. In addition, the LMP7702 is specified to operate at a much lower supply voltage (down to 2.7 V).

The first opamp in the package is configured as an unity-gain voltage buffer. The 10 nF and 10 kΩ resistors are used to protect the input of the amplifier and isolate the output of the amplifier from the active shield. No external input biasing network is necessary with the LMP7702 and the inputs consistently charge and stay within the rail-to-rail input range during use. Likewise, the outputs are also stable since the amplifier has rail-to-rail outputs and is configured as unity gain. This achieves optimal performance since any bias network necessarily adds noise and degrades the input impedance.

The lack of a bias network, however, results in an undefined (although full usable) DC operating point. To remove this offset as well as low frequency noise/drift, a passive RC high pass filter with a corner frequency of 0.7Hz is used to center the signal around V_{ref}. The second opamp in the package is then buffers this high-passed signal and drives the cable connecting the electrode to the base unit. A 100 Ω resistor is used to isolate the cable capacitance from the amplifier's output.

Although this lack of gain through multiple buffers is theoretically disadvantageous from a noise perspective, in practice the noise from the non-contact electrode to body interface will dominate the subsequent stages. Having a unity gain buffer also eliminates the need for impractically precisely matched passive components at the electrode to achieve a good common-mode rejection ratio (CMRR).

4.2.3 Wireless Base Unit

Each of the electrodes outputs a buffered, unity-gain, analog signal. A compact, battery-powered base unit (Fig. 4.3) provides the necessary power, reference and ground lines.

An N-input differential amplifier was constructed by extending the topology of the well known 3-input instrumentation amplifier [64]. In general, any practical biopotential amplifier circuit should work well. Since the non-contact electrodes are AC coupled with low-offset buffers, it was possible to incorporate a large amount of gain (40 dB) directly within one amplifier stage. A 16-bit ADC (AD7685) is used, resulting in a LSB of 0.5 μV over an input range of 33 mV.

A two pole passive RC filter is used to filter out high-frequency components before the ADC. Both corner frequencies are set at 159 Hz. Although the anti-alias filter provides only a shallow roll-off, we use a sufficiently high internal sampling rate to avoid any noticeable aliasing artifacts. This also minimizes the number of passive and active components.

The overall bandwidth of the system is then dictated by the analog high-pass filter of the non-contact electrode, 0.7 Hz, and the antialias filter, 159 Hz.

4.2.4 Grounding

Subject grounding is one of the most important factors in achieving good signal quality. Unfortunately, it is often overlooked and not always explained clearly in the literature. In our experience, many of the problems with biopotential instrumentation, including non-contact sensors, were due to improper grounding techniques.

In line with the idea of a fully insulated system, we use non-contact coupling to connect the circuit ground back to the body. A dummy electrode without components is used to as the non-contact ground electrode. Such a ground is fully insulated, but offers only a weak coupling, rendering the system susceptible to interference (Fig. 4.4) as the the body and instrument circuit float independently from each in the presence of interference.

Actively driven grounding schemes are a well-known technique [65] to reduce the influence of common-mode interference. Also commonly referred to as the driven right leg (DRL), active grounding reduces the impedance of the ground by placing it within the feedback loop of an amplifier and driving the body to the same potential as the circuit ground. It is important to note that the DRL does not necessarily involve driving the right leg and that the nomenclature stems from its first use in ECG applications. Generally the DRL electrode may be placed anywhere on the body.

In our system, an active ground circuit is implemented on the base unit with the average of all the electrodes, V_{cm}, connected to an inverting amplifier with gain of -100 to provide an additional 40dB of CMRR for the system. The signal is fed back into the body through the dummy DRL electrode.

An simple experiment, depicted in Figure. 4.4 illustrates the effectiveness of this active ground. The non-contact active ground is as effective as a driven dry ground contact (anti-static wrist strap). Passive dry grounds start to suffer from 60Hz noise pick-up. A floating (purely parasitic) ground may also be used, but suffers from large 60Hz and other low frequency artifacts, and is not suitable for any serious measurements.

The combination of the active ground and the fact that the battery-powered system is fully isolated from the electrical mains, results in a very clean signal, free from $60Hz$ interference.

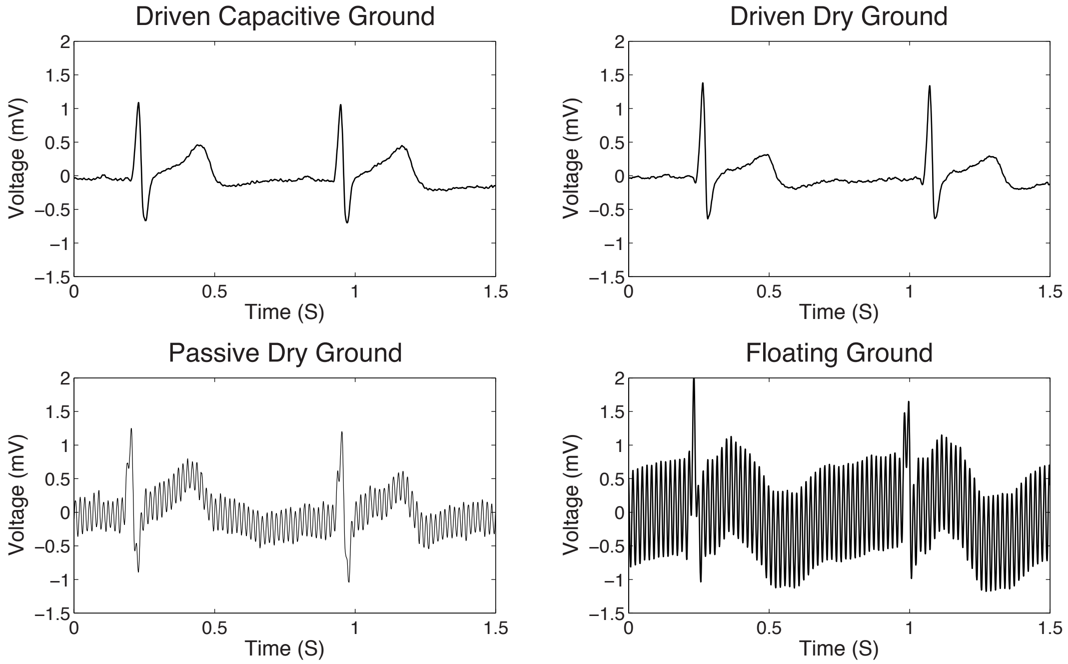

Figure 4.4: Comparison of different grounding techniques. The signals are shown at full bandwidth, without 60 Hz filters.

4.2.5 Radio Frequency Interference

An additional concern for portable, wireless healthcare devices is immunity against radio frequency interference. Portable sensors must be robust against radiofrequency and other electromagnetic sources, especially with the possibility of coexisting with multiple nearby wireless transceivers. To qualitative assess the effect of a typical RF interference event on the sensor, we placed a cellular phone on top of both an electrode in use and observed the signal output. A second experiment involved placing the the cellular phone on top of the base unit PCB, as a baseline. Calling the cellular phone initiates a burst of RF activity (commonly manifesting as pops on poorly shielded audio equipment) and introduces interference into the biopotential measurement. Figure 4.5 depicts the induced effect on the ECG trace. It is important to note that the induced disruption in the signal was actually *greater* with the RF source near the base unit, which demonstrates the effectiveness of the electrode's active shield. In general, it can be concluded that with the presence of the integrated shield, the non-contact electrode is, at a minimum, no worse

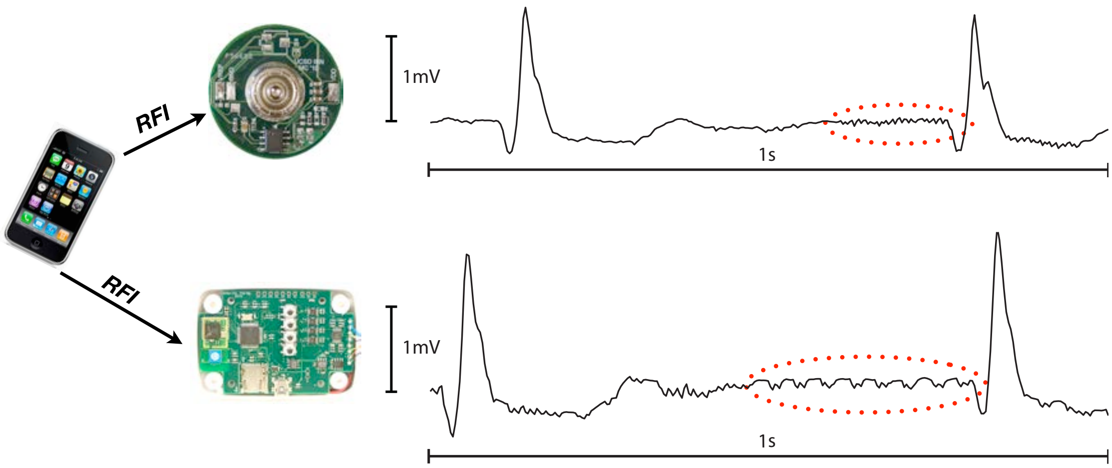

Figure 4.5: Results of the RFI experiment test injecting bursts of activity from a cellphone into both the electrode and the base unit. The non-contact electrode's active shield is highly effective at reducing the effects of external interference

than a low-impedance wet electrode in terms of RFI rejection.

4.2.6 Data Acquisition

A simple 16-bit microcontroller (PIC24) was used to control the ADC. The base unit supports both Bluetooth wireless connectivity for live streaming of data to a PC or other display interface. For longer-term mobile recordings, a microSD interface is also available. The entire system is powered from a 900 mAh rechargeable lithium-polymer battery good for approximately 10 hours of continuous recording with real-time wireless telemetry.

The device is recharged through a mini-USB connector. A USB-RS232 converter (FT232R) is also available for higher bandwidth, real-time streaming of data than what is possible with the Bluetooth application. For safety reasons, this mode should only be used with an unplugged laptop, since no power isolation circuit is provided.

For the purposes of the experiments in this paper, we utilized the Bluetooth transmitter which streamed data into a simple PC display and logging application at a rate of 343Hz for the four signal channels. In addition, higher data rate modes are also available, supporting four channel streaming at 1800 Hz. As wireless protocol

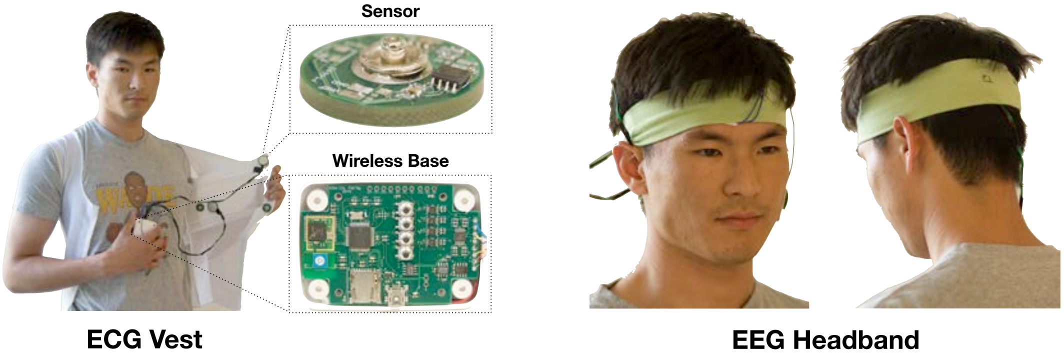

Figure 4.6: Picture of the prototype ECG chest vest and EEG head band.

and optimization is not the focus of the paper, the Bluetooth module is a convenient, industry-standard, platform to conduct experiments on a variety of mobile platforms and offers the flexibility of very high data rates, as necessary.

4.3 Wearable Sensor Harness

As mentioned earlier, non-contact electrodes do not have the benefit of being fixed to body via an adhesive. Consequently, they are very sensitive to motion errors and require a secure harness on the wearer to achieve an optimal signal.

We have developed an ECG chest harness and an EEG headband (Fig. 4.6) to mount the non-contact electrodes. As shown later, a firm harness that fixes the electrodes to the body allows the non-contact electrode to perform almost as well as standard adhesive Ag/AgCl electrodes.

A compression vest was used as the basis of the ECG chest harness. Adaptation of the gynecomastia vest was prepared by sewing electrode snap connectors onto the vest and snapping the electrodes during use. Non-contact electrode placement was assigned to the two midaxillary positions. This vest was ideal for electrode placement due to its elastic contouring ability, covering of the thoracic surface with sufficient firmness. A second elastic band was also optionally available to add additional security for holding the electrodes in place.

For EEG experiments, a simple, tight, elastic cloth headband was used in a similar fashion by sewing in snap connectors for the non-contact electrodes. In contrast to known commercial and research headbands, our version allows for signals to be acquired through hair using the non-contact electrodes. The design and operation of the EEG headband was especially challenging due to the flexible properties of hair which make securing the electrodes difficult.

4.3.1 ECG Experiments

The ECG vest was used to collect live data using the non-contact sensors. For the purposes of generating a direct comparison, two of the four electrode inputs were connected to standard passive Ag/AgCl (3M Red Dot) and the other two were connected to the non-contact active electrodes. The subject was a healthy 21 year old male. Experiments were conducted in a standard electrical engineering lab with no effort to eliminate sources of interference.

For the ECG tests, the non-contact electrodes were mounted into the tight, body-fitting harness with the two non-contact electrodes on the left and right sides of the ribcage. The subject wore a simple cotton t-shirt underneath the harness. Two Ag/AgCl adhesive electrodes were also placed in a nearby position directly on the skin. The output signal for the non-contact sensor was defined by taking the difference between the two and likewise of the Ag/AgCl electrode pair.

Figure 4.7 shows a detailed plot of a ECG sample taken while the subject was sitting at rest. The overall signals are nearly indistinguishable in both shape and noise levels, even though the non-contact electrodes were operating through clothing. All relevant ECG features are clearly visible. The slightly smaller amplitude of the signal from the non-contact electrode is likely due to the signal attenuation from the extremely high source impedance.

One previous study [63] compared the performance of a proprietary non-contact electrode design versus contact electrodes with a subject lying down. We extend the methodology established in these tests to include data with an actively moving subject. Figure 1.6 shows 10-second plots comparing the signal acquired from the non-contact and Ag/AgCl electrodes.

As expected, the signal remains mostly undisturbed while the subject is at rest and

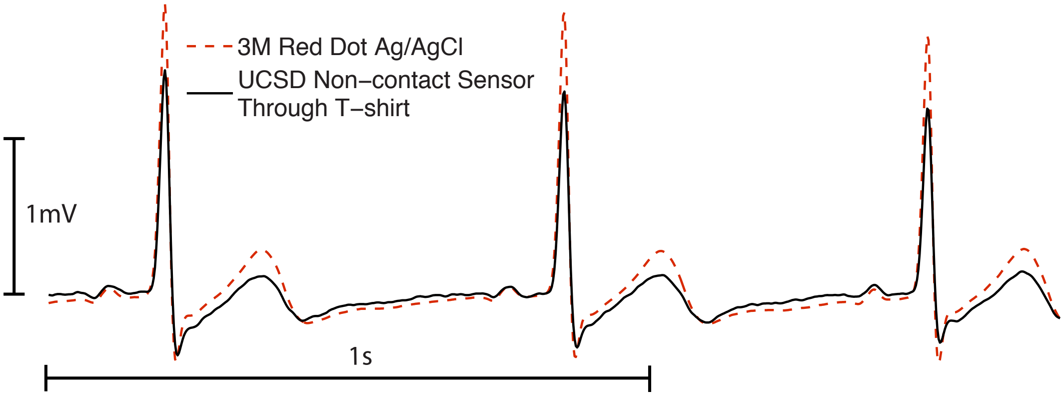

Figure 4.7: Detailed comparison of signal acquired simultaneously from a set of clinical grade 3M Red Dot Ag/AgCl adhesive electrodes and the non-contact sensor. The non-contact sensor was placed over a cotton t-shirt.

walking lightly. During more vigorous activities, motion artifacts become problematic for both electrodes types, rendering the ECG signal useful for only R-R beat detection. The signal for the non-contact electrode is not substantially worse, as long as the non-contact electrodes are fixed tightly against the body using the harness. It should be worth noting, however, that non-contact electrodes are extremely sensitive to friction (rubbing against cotton), which necessitates the hight chest harness.

We again used the same methodology as [63] to compare the extracted R-R beat intervals to show the equivalence of Ag/AgCl and non-contact electrodes, extending their study to subjects in motion. The plot is shown in Figure 4.8. The extracted R-R beat intervals are virtually identical across all the tested activities.

For applications beyond simple heart beat and rhythm detection, a multi-lead signal which can provide a detailed diagnosis of the heart is desirable. However, a full 12-lead resting ECG is difficult to maintain in ambulatory conditions since the patient must precisely place 12 electrodes. Lead derivation techniques are possible with a just a subset of electrodes, as few as four plus ground. As with most lead derivation techniques, we utilized a linear transform to map four electrodes into 12 lead vectors.

The positioning of the electrode (Fig. 4.6) and transformation coefficients were extrapolated from [66]. A slight adjustment in the transformation matrix were necessary since our system outputs each signal referenced against the common-mode whereas

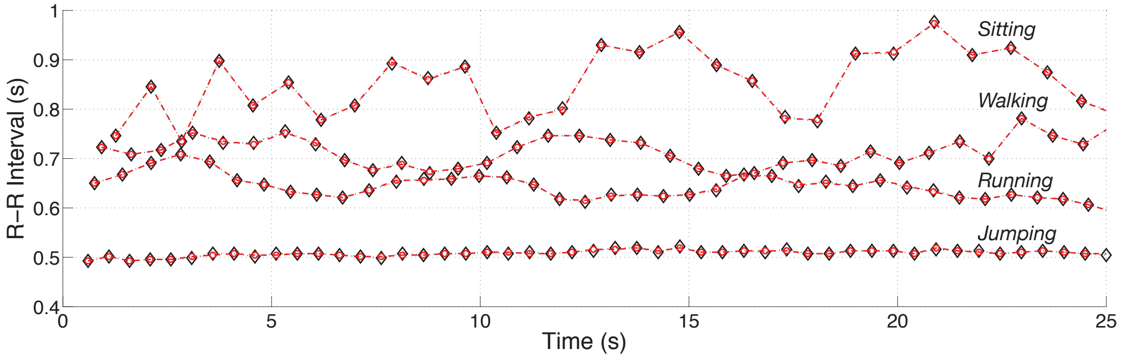

Figure 4.8: Extracted heart beat (R-R) intervals from the ECG signal for the Ag/AgCl sensors (black trace) versus the non-contact sensor (red trace)) prototype. The intervals are essentially identical.

typical EASI schemes [66] are designed to accept sets of bipolar leads (both are mathematically equivalent via a linear transform).

Figure 4.10 shows the derived 12-lead ECG, which show the expected shape and features, such as the increasing amplitude of the R-wave progressing from the V1 to V6 lead. Although the combination of the approximate positioning from the vest harness and increased artifacts from the non-contact electrode will likely degrade the signal, this scheme offers a wearable method for obtaining a useful multi-lead signal from a patient.

4.3.2 EEG Experiments

Similar to the cardiac data, two of the input channels were connected to Ag/AgCl adhesive electrodes to achieve a direct comparison with the non-contact sensors. For the EEG experiments, one non-contact electrode was placed on the forehead (Fp1) and the second on the back (Oz), through hair. Likewise, an Ag/AgCl electrode was also placed on the forehead (Fp2). However, since it was not possible to place an contact electrode through hair, the second Ag/AgCl electrode was placed on the mandible (A1). Unless specified, the output for each electrode was defined as the signal at each channel minus the common-mode of four channels.

Figure 4.11 shows a detailed time-domain plot of all four EEG channels with the subject relaxing, at rest with closed eyes. Not only are the expected alpha rhythms

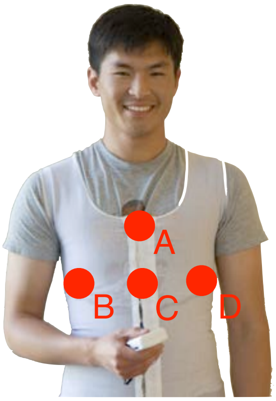

ECG Lead	A	B	C	D
I	0.198	-0.703	0.015	0.49
II	-1.019	0.439	0.075	0.505
III	-1.219	1.141	0.061	0.017
aVR	0.41	0.132	-0.045	-0.497
aVL	0.709	-0.922	-0.023	0.236
aVF	-1.119	0.79	0.068	0.261
V1	-0.23	0.274	0.501	-0.545
V2	-0.22	-0.306	1.075	-0.549
V3	-0.44	-0.555	0.924	0.071
V4	-0.622	-0.624	0.601	0.645
V5	-0.491	-0.625	0.233	0.883
V6	-0.401	-0.319	-0.008	0.728

Figure 4.9: Electrode positions and table of coefficients for 12-lead derivation [66]. Each derived lead is the weighted sum of the four physical electrodes in the vest.

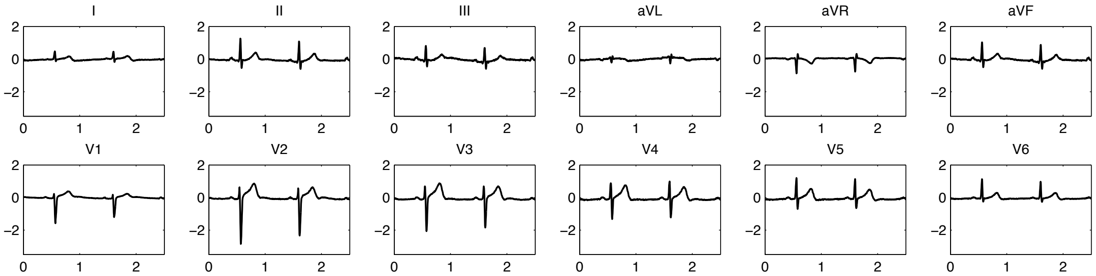

Figure 4.10: Derived 12-lead ECG from 4-electrode chest band in an EASI array.

clearly visible (especially in the occipital electrode), the signals from the Ag/AgCl and non-contact electrodes are virtually identical. Strong alpha wave activity is seen, as expected for an awake, relaxed subject. The signals are all shown at full bandwidth, without an additional digital filtering showing the effectiveness of the active shield and driven ground.

A second montage consisting of two signals was obtained by using the A1 Ag/AgCl electrode as a reference for the frontal and parietal non-contact electrodes. In this experiment, the subject was asked to blink several times and then close his eyes. Figure 4.12 shows the clear blink artifacts in the Fp1A1 signal followed by the onset of alpha waves in the OzA1 signal.

The ability to easily obtain signals from the normally hair covered occipital and

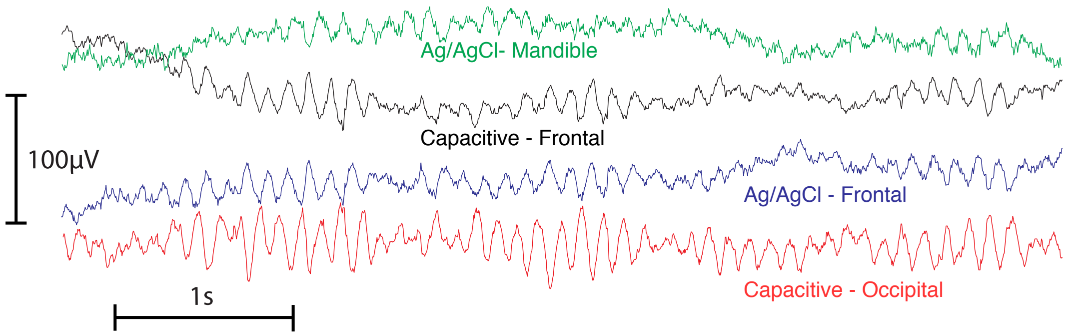

Figure 4.11: Close-up of EEG signals acquired using a mix of Ag/AgCl (3M Red Dot) and non-contact non-contact electrodes. No extra filtering beyond the analog anti-alias has been applied to the raw signal to show that the sensor is free from 60 Hz interference.

parietal regions is especially useful for brain-computer (BCI) and other EEG-based neural interfaces. Frontal forehead electrodes are unable to resolve important responses including the P300 evoked potential potential and the steady-state visual evoked potential (SSVP), both commonly used for BCI applications.

To test the effectiveness of the non-contact electrode over the haired occipital region, a simple experiment was devised where the subject was asked to watch a LED flashing at a specific frequency. Power at the same frequency should be observed in the EEG signal. Figure 4.13 shows the spectrum of the EEG signal for three different trials.

Sleep diagnosis is another important medical application of EEG technology. Sleep apnea along with other sleep related neurological disorders presents a significant health and economic burden. Current clinical sleep diagnosis protocol involves subjecting patients to a complex array of EEG and other sensors, making the procedure both expensive and uncomfortable. A few portable devices have appeared on the market (eg. Zeo) that greatly simplify the number of EEG electrodes by using forehead only sensors, but it is not clear whether the limited amount of signals available on the forehead is sufficient for clinical use. The non-contact sensor allows for EEG signals to be comfortably resolved across the head in the same positions as clinical systems but without the need to apply uncomfortable and inconvenient gels.

To illustrate a simple experiment involving sleep diagnosis, a subject was asked to take a nap while wearing the EEG headband. The recorded EEG signal was analyzed

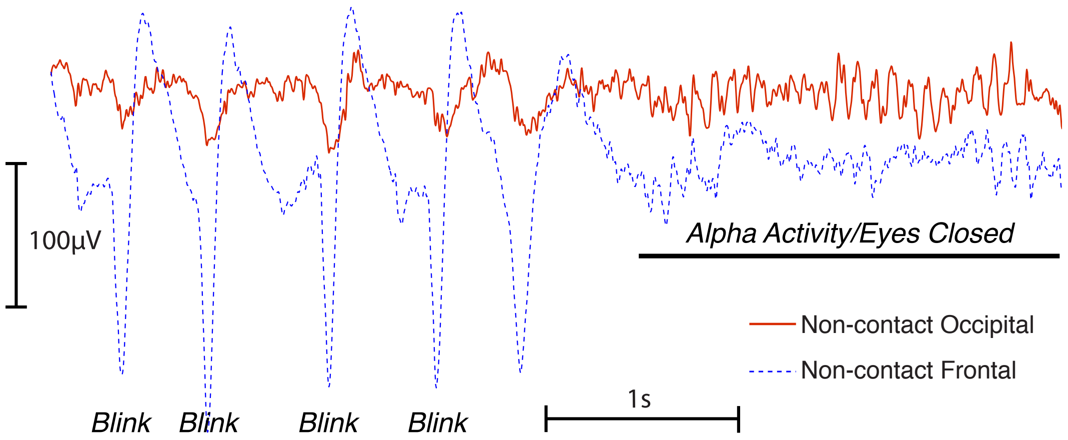

Figure 4.12: Experiment showing the signal from the frontal non-contact electrode (Fp1A1) in blue and the signal from the occipital non-contact electrode (O1A1). Eye blink artifacts are visible in the frontal electrodes during the first half of the recording. Strong alpha activity is seen in the occipital electrode after the subject's eyes close.

by taking a spectrogram (10 s window, 1 to 40 Hz in .1 Hz increments) of the O1A1 montage. The spectrogram is shown in Figure. 4.14 where three states are visible (awake, eyes closed, asleep). In this experiment the time it took the subject to fall asleep was approximately half an hour.

4.4 ECG Tag

In addition to the ECG vest harness, we have also designed a second non-contact ECG sensor module to demonstrate a fully wireless, non-contact sensor. Unlike the previous system consisting of discrete electrodes connected a common base unit (similar a traditional Holter monitor), this ECG Tag is a self-contained module which integrates two recording electrodes, a ground as well as supporting acquisition electronics on a single substrate. This allows for a compact, fully integrated wireless sensor module, without any separate cords or electrodes. Figure 4.15 shows a picture of the ECG tag with dimensions and components.

ECG signals are sensed through two disc-shaped electrodes with equal area on the bottom side of the tag. A simplified version, supporting only one set of differential

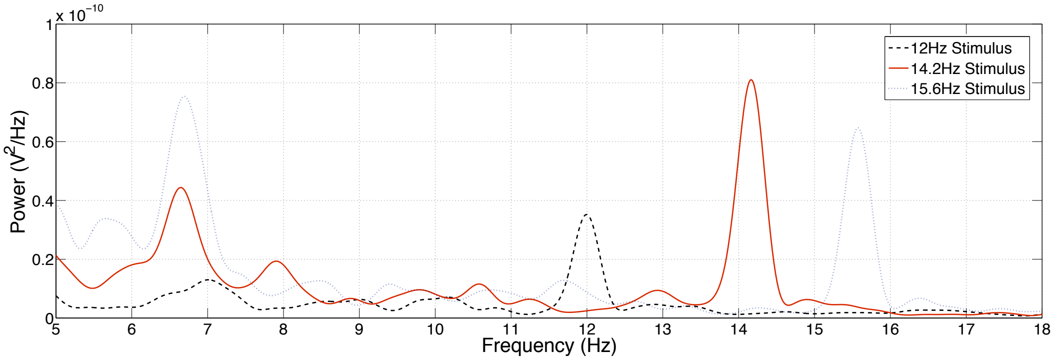

Figure 4.13: Power power spectrum from the SSVP experiment. The subject was asked to look at a flashing stimulus at specific frequencies. The same frequency can be observed in the occipital non-contact electrode.

inputs, of the previous design (Fig. 4.3) was used to amplify and acquire the ECG signals. A set of contact points (Fig. 4.15) on the bottom of the electrode serves as the DRL to ground the sensor to the subject.

Unlike conventional instruments which obtain an ECG lead vector by taking the difference across two or more electrodes separated through a large baseline, the ECG tag measures the Laplacian of the biopotential [67] at a single point on the chest. While this makes it impossible to obtain a standard ECG lead, the signal from the tag still contains familiar ECG morphology (eg. QRST complex).

In addition to the traditional ECG measurements with the vest harness, we also evaluated the signal from the wireless non-contact ECG tag. Figure 4.16 shows samples from the tag in both direct skin contact and through a cotton t-shirt. With the Laplacian electrode arrangement, the greatest ECG signals were obtained on the subject's chest, near the vicinity of the heart.

Signals obtained via the Laplacian electrode are approximately one order of magnitude lesser that with a conventional lead. However, the signal retains the same morphology with the exception of the p-wave which is either not present in the Laplacian of the surface biopotential or is obscured by the noise floor.

Further miniaturization and improvement of the form factor for sensor will make it possible to build an EEG version of the wireless tag. Laplacian configurations are

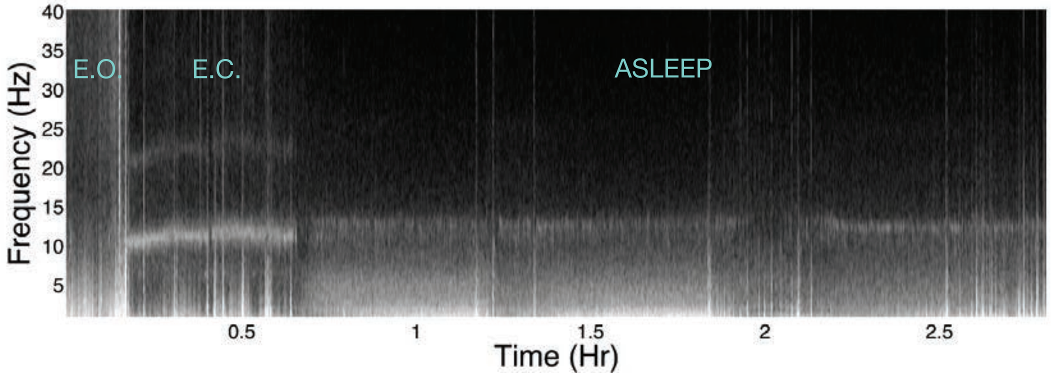

Figure 4.14: Spectrogram of sleep EEG taken with the headband. The signal is taken from the non-contact electrodes (Fp1O1). Three states are visible in the plot. The first is when the subject is awake with eyes open (E.O.), showing the absence of any dominant rhythms. Strong alpha activity is present as the subject closes his eyes (E.C.). This transitions into the last section as the subject enters sleep.

commonly used in standard EEG recordings (evaluated by using an array of nearby electrodes) and is useful in a variety of applications.

4.5 Conclusion

As mobile, wearable physiological monitoring devices become an increasingly important part of wireless health, new sensor systems that are both comfortable and convenient are required. Non-contact sensors have traditionally been poorly understood and thought of as unsuitable for medical-grade applications, but we demonstrate how careful design, both at the circuit and system level can produce signals comparable to clinical adhesive Ag/AgCl electrodes for both ECG and EEG applications in selected experiments, leading to new possibilities in wireless health monitoring.

The sensors and demonstration platforms described in this paper is expected to enable a variety of new wireless health monitors. As an example, for the monitoring of arrhythmia and other cardiac disorders, one version of the wireless health device could consist of a wearable band, slipped comfortably on top of an undershirt. Another embodiment may utilize the small ECG tag as an ‘event monitor’ where the patient or

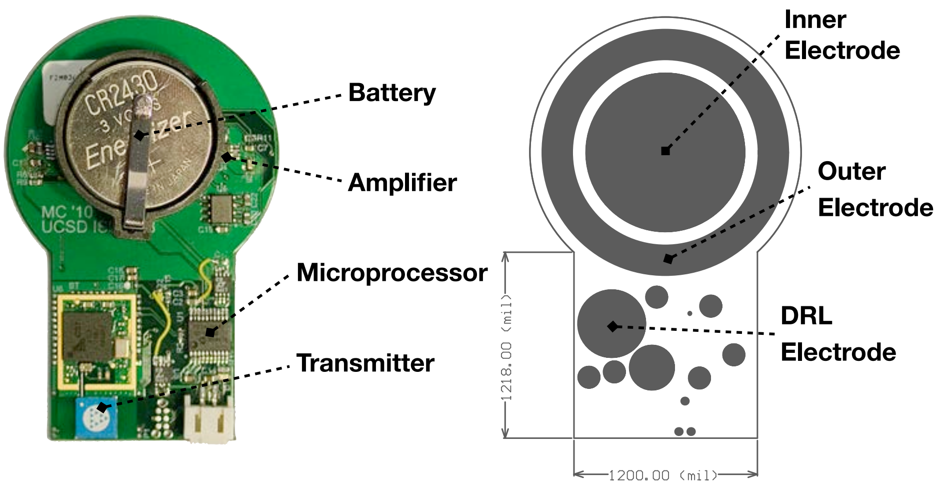

Figure 4.15: Picture of the fully wireless ECG tag. The self-contained module contains all the necessary circuitry for a 2-channel wireless ECG. The bottom of the tag implements a local electrode that evaluates the Laplacian of the surface biopotential on the chest.

health practitioner needs to only press the sensor on their chest to obtain an ECG trace, without the need to remove clothing, whenever desired.

Likewise non-contact sensor technology may become an enabler for practical, high-resolution, high-density EEG systems which are currently confined to hospitals and laboratory environments. Future applications include neurodiagnositics including sleep and epilepsy. In addition, the ability to obtain signals through hair is a key step towards building practical, user-friendly brain computer interfaces and neuroprosthetics. Fully wireless systems based on the non-contact tag may also enable small, unobtrusive, patch-like brain monitoring systems for both medical and consumer use (eg. recreation, alertness monitoring).

Non-contact and other unobtrusive physiological monitoring devices will play an important role in wireless health, especially as more wearable and comfortable version are developed and backed with the appropriate wireless, software and signal analysis infrastructure.

Chapter Four is largely a reprint of material submitted to the ACM Transactions on Embedded Computing Systems: Y. M. Chi, P. Ng and G. Cauwenberghs, “Wireless

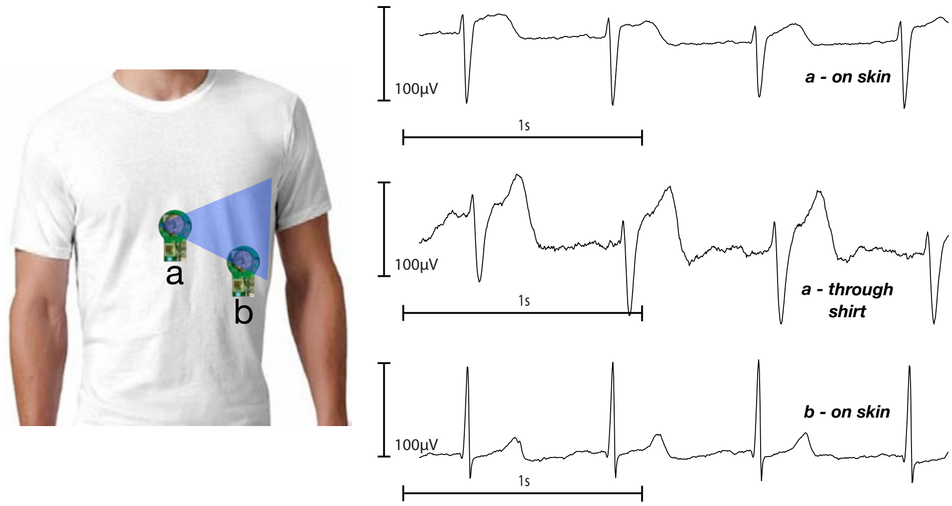

Figure 4.16: Sample signals from the ECG tag taken both directly on the skin (top) and through a t-shirt (middle) on the sternum (location a). An alternative lead can also be obtained by placing the sensor on the left side of the chest (location b), directly over the heart (bottom). The colored region indicates areas on the chest where the ECG tag can obtain a signal.

Non-contact ECG and EEG Biopotential Sensors," *ACM Transactions on Embedded Computing Systems*, (submitted). The author was the primary author and investigator of this work.

Chapter 5

An Integrated High-Input Impedance Front-end Amplifier for Non-contact Sensors

5.1 Introduction

Non-contact electrode technology, which can acquire biopotential (ECG/EEG) signals without the need for gels, adhesives and direct skin contact, has long been explored for use in unobtrusive physiological monitoring [59, 11, 27, 14, 50, 56]. Unlike low-impedance wet and dry electrodes, however, the high source impedance ($Z_s > 1\,\mathrm{G\Omega}\,||\,30\,\mathrm{pF}$) encountered in non-contact interfaces still poses a circuit design challenge at the sensor front-end. Critical performance specifications including noise, frequency response, CMRR, and DC-bias stability are easily compromised, necessitating front-ends with input impedances even greater than what is normally possible from standard FET components.

The concepts behind ultra-high input impedance buffers have been well-known in the literature and analyzed for vacuum tube [33] and early solid-state devices [68, 69] and applied towards electrophysiology recordings, particularly microelectrode arrays. In more recent years, non-contact ECG/EEG have exclusively focused on utilizing commercial off-the-shelf amplifier components due to their ease of use [11]. Although input specifications of these devices are excellent for the majority of applications, the input impedance specifications (approx. 2–5 pF) are still insufficient for non-contact sensing. Active shielding and bootstrapping of the sensor package mitigates PCB-level stray capacitances, but cannot compensate for internal parasitics of an off-the-shelf amplifier. As a result, achieving acceptable performance with standard amplifier components has required manually tuned neutralization networks [11, 70] and elaborate input biasing schemes, both of which are often imperfect and impossible to match between different devices [31].

In light of these limitations, we have designed a custom impedance converter front-end, to specifically address the difficulty with achieving a low input capacitance and low-noise input biasing. An IC approach allows for full access to all the potential parasitic elements starting from the input transistor itself and form a complete active shield around the sensitive input node. With these techniques, we achieved an input capacitance of just 60 fF, and stable frequency response even below 0.01 Hz, completely without the use of neutralization or manual tuning.

This paper specifically focuses on detailing the circuit design and characterization of an integrated, very high input impedance amplifier for biopotential sensing applications. Applications of this chip for cardiac and neurological applications can be found in related publications [71].

5.2 High Impedance Biopotential Sensing

It is useful to illustrate the design considerations for non-contact sensors before delving into the details of the implemented circuit. Building sensor front-end that can interface with the high source impedances encountered in non-contact sensing is often challenging both from a design and implementation standpoint. Figure 5.1 shows the generic single-ended circuit model for a non-contact sensor. The signals from the body is modeled as a voltage source, V_s, which is coupled through an electrode interface reduced to the dominant R-C layer: R_s and C_s. The sensor front-end is a unity gain buffer with some finite input impedance: R_i and C_i and a bootstrapped capacitance (e.g. gate-source capacitance in a source-follower, active shield), C_f. Relevant noise sources

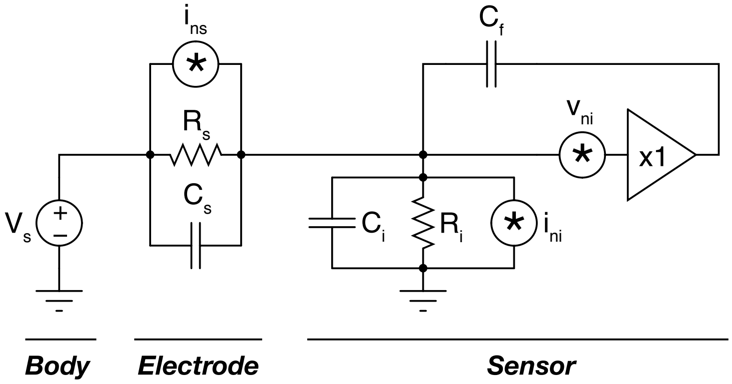

Figure 5.1: Sensor model showing the relevant noise sources from the electrode interface and amplifier.

are the thermal noise current in the electrode, $i_{ns} = 4kT/R_s$, the thermal noise from the input resistance, $i_{ni} = 4kT/R_i$, and the amplifier's input referred voltage noise, v_{ni}. Alternatively the input impedance and noise current could be dominated by shot noise from a P-N junction (e.g. biasing diode), but the results from the resistive model are still fully applicable. Translating the results for a diode can be accomplished by modelling the diode as a small-signal resistor and rewriting it's shot noise current in terms of it's small signal resistance.

5.2.1 Noise Figure

From an intrinsic noise perspective, the total noise at the output of the buffer can be written as,

$$v_{out,n}^2 = [\frac{4kT}{R_s}|Z_s||Z_{in}|^2 + \frac{4kT}{R_i}|Z_s||Z_i|^2 + v_{ni}^2|1 + sC_f(Z_s||Z_i)|^2]\Delta f, \tag{5.1}$$

and the noise figure of the sensor then simplifies to,

$$F = 1 + \frac{R_s}{R_i} + \frac{v_{ni}^2 R_s}{4kT}(\frac{1}{|Z_s||Z_i|^2} + \omega^2 C_f^2). \tag{5.2}$$

As expected, driving the input impedance to infinity ($R_i \to \infty$, $C_i \to 0$) minimizes the noise figure for the sensor, irrespective of the source impedance. The last term in the noise figure equation which depends only on C_f and v_{ni} will be addressed shortly.

Unlike RF design where the source impedance is usually well defined, the range of coupling impedances for biopotential sensing can vary orders of magnitude ($10^3\Omega$ to $10^{12}\Omega$). For a typical non-contact scenario the circuit parameters are: C_s = 20 pF, R_s=1 GΩ, C_i = 5 pF, R_i = 1 TΩ, C_f = 5 pF, v_{ni} = 90 nV/Hz$^{1/2}$ and ω=2π5 rad/sec. Surprisingly, the resulting noise figure at 5 Hz is just .0032 dB, showing that once the electrode interface material, not the sensor front-end amplifiers, accounts for the vast majority of the noise generated.

5.2.2 Input Referred Sensor Noise

The input referred noise of a generic non-contact sensor with a known input voltage and current noise generators has already been well described using models based on discrete operational amplifier components. The difference with an integrated approach is that the designer now has full control over the term,

$$v_{ni}(1+\frac{C_f}{C_s}), \tag{5.3}$$

which describes the voltage noise multiplication effect due to parasitic input capacitance. In terms of input referred noise, it does matter if these capacitances are bootstrapped or not. For these calculations, it will simply be assumed that all parasitic input capacitances have been successfully shielded noting that C_f can be simply replaced by a term representing sum of bootstrapped and non-bootstrapped for the more general case.

Within the frequencies of interest for biopotential sensing, it is the 1/f noise that dominates the voltage noise of the input transistor, rather than thermal noise. Thus the only way to reduce, v_{ni} is by increasing the size of the input transistor. However, increasing the size of the input transistor necessarily also increases the input capacitance of the device. For very low-impedance sources, this is typically not a consideration and the input noise can simply be reduced by arbitrarily scaling the size of the transistor. For capacitive/high-impedance sources, there must exist an optimum trade-off size that balances the input noise with the input capacitance.

The 1/f noise decreases with the square root of the transistor area, A. At the same time, the input capacitance of the transistor largely scales linearly with A. The input 1/f noise, $v_{n,1/f}$ can then rewritten in terms of A and two process parameter constants: $C_{i,0}$,

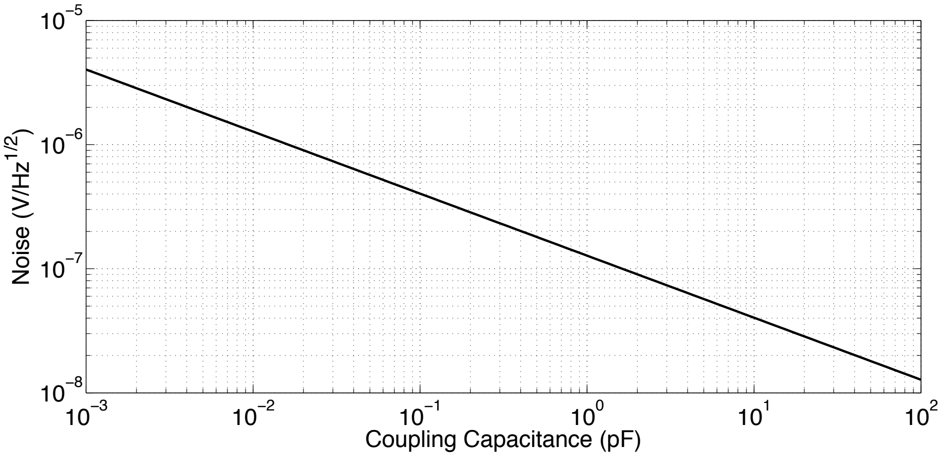

Figure 5.2: Minimum achievable spot noise at 100 Hz in the C5N process by optimizing the size of the input transistor to match the expected coupling capacitance.

the unit input capacitance and $v_{n,0}$, the unit 1/f noise where

$$C_i = AC_{i,0} \tag{5.4}$$

and

$$V_{n,1/f} = v_{n,0}/\sqrt{A} \tag{5.5}$$

For the C5N process constants, extracted through simulation, were: $C_{i,0}$ = 4.5 fF/μm^2 and $v_{n,0}$ = 9.5 μV/Hz$^{1/2}$. The voltage noise term can now be rewritten as,

$$\frac{v_{n,0}}{\sqrt{A}}(1+\frac{AC_{i,0}}{C_s}). \tag{5.6}$$

The lowest noise is achieved by simply achieved by setting the transistor input capacitance equal to the source capacitance. The minimum achievable noise at a given coupling capacitance C_s is then,

$$v_{n,opt} = \frac{2}{\sqrt{C_s}} v_{n,0}\sqrt{C_{i,0}}, \tag{5.7}$$

where the product $v_{n,0}\sqrt{C_{i,0}}$ is a process parameter constant and can be used to compare different technologies. A calculation of the minimum achievable noise for the ON Semiconductor C5N process is shown in Figure 5.2.

In practice it is impossible to have a prior knowledge of the coupling impedance with non-contact sensors and there exists a significant parasitic input capacitance component that does not scale with the 1/f noise. In addition, the amplifier itself is rarely the dominant noise generator once the material interface is accounted for. Thus, detailed optimization is only useful for applications where the source truly capacitive, such as free-space electric field meters.

5.2.3 Common-Mode Rejection Ratio

Common-mode rejection of interference signals is often a much greater design consideration towards achieving adequate performance than intrinsic circuit noise. Typically a CMRR of 80 dB or more is desired. In conventional instrumentation operating with wet electrodes, a high common mode rejection ratio, often well above 100 dB, is easily achieved through good circuit component matching and the fact that the source impedance of wet electrodes are well below that of the amplifier's input impedance. Non-contact sensors, however, suffer CMRR performance degradation due to the signal attenuation from the source to input voltage division. The CMRR of two sensors, limited by the effects of input attenuation, can be written as,

$$\mathrm{CMRR} \approx \frac{|Z_i|}{|Z_1 - Z_2|}, \tag{5.8}$$

where Z_1 and Z_2 is the source impedances of the first and second electrodes. At 50/60 Hz, the impedances are primarily capacitive and the expression simplifies to

$$\mathrm{CMRR} \approx \frac{|C_1 C_2|}{C_i |C_1 - C_2|}. \tag{5.9}$$

Using the same circuit parameters as before, but now with a mismatch of 5 pF between the two electrodes, the CMRR is only 26 dB! It may be possible to add an additional 40 dB or so with an active ground circuit, but the performance is still well below what is required for clinical-type applications. If instead the input impedance of the sensor was increased to 60 fF, then the CMRR increases to 64 dB and becomes 104 dB with an active ground - well within the range of medical grade instrumentation. From these examples, it can be seen that common-mode rejection, rather than noise figure, that drives the need for very high input impedances with non-contact sensors.

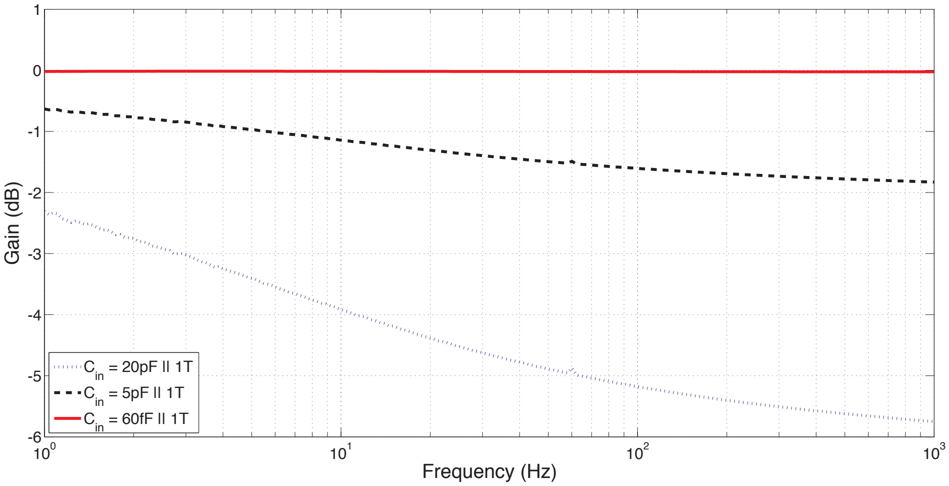

Figure 5.3: Computed sensor frequency response for three possible amplifier input capacitances (20 pF, 5 pF and 60 fF) using measured data from Fig. 2.3 for a cotton interface. Even with just 5 pF of input capacitance, the sensor's frequency response become significantly low-pass filtered due to the high source impedance, which can lead to signal morphology distortion (Fig. 5.10).

5.2.4 Frequency Response

In addition to decreasing the CMRR, excessive parasitic input capacitances at the input can also lead to excessive filtering of the biopotential signal. The most basic effect is the simple voltage divider set by the ratio of the source and input capacitances. As shown previously, however, the source impedance of a typical non-contact interface (e.g. cotton) has a large resistive component as well, which forms an R-C low-pass filter in addition to the simple capacitive voltage divider. Figure. 5.3 plots the effective transfer function with three different input impedances using data collected previously for a cotton sweater. For diagnostic grade applications, large input capacitances relative to the source impedance can lead to significant morphology distortion (Fig. 5.10).

Bootstrapping to mask the parasitic input capacitance also has an effect on the final bandwidth of the sensor. To illustrate the effect of bootstrapping on the input capacitance, it will be assumed that the buffer in Fig. 5.1 is a single pole (f_{3dB}) amplifier

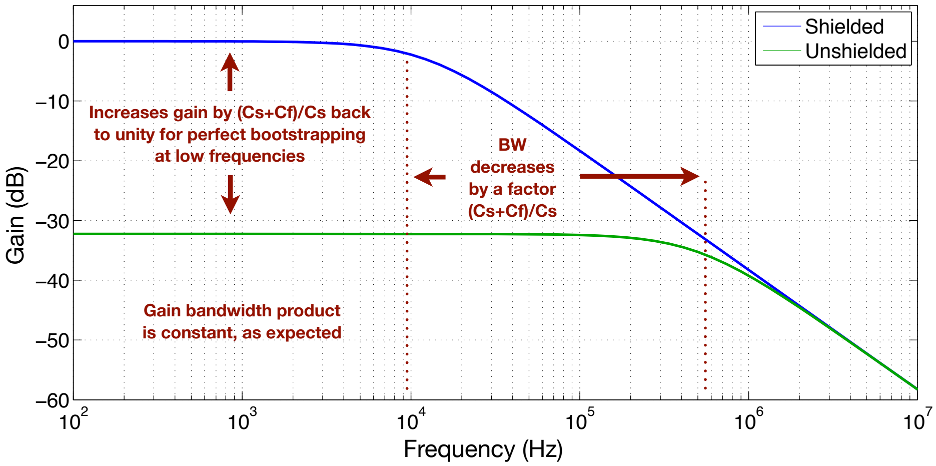

Figure 5.4: Effect of bootstrapping on the effective bandwidth of the sensor. This effect can also be observed in the measured frequency response (Fig. 5.6).

with the transfer function,

$$G_v(s) = \frac{1}{1+\frac{s}{2\pi f_{3dB}}}. \tag{5.10}$$

The total parasitic capacitances (C_i and C_f) will be denoted as C_t. In the case where there is zero bootstrapping, then the effective transfer function is just the original frequency response of the buffer, with an attenuation factor,

$$G_{v1} = \frac{C_s}{C_s+C_t}\frac{1}{1+\frac{s}{2\pi f_{3dB}}}. \tag{5.11}$$

Moving the all capacitances from going to circuit ground to the output of the amplifier via bootstrapping changes the transfer function to,

$$G_{v2} = \frac{1}{1+\frac{s}{2\pi f_{3dB}}\frac{C_s+C_t}{C_s}}. \tag{5.12}$$

In essence, bootstrapping restores the DC gain of the buffer by trading the equivalent amount in bandwidth ($f'_{3dB} = f_{3dB}C_s/(C_s+C_t)$) thus maintaing a constant gain-bandwidth product. This effect can be observed in the measured transfer function of the implemented sensor in Figure 5.6

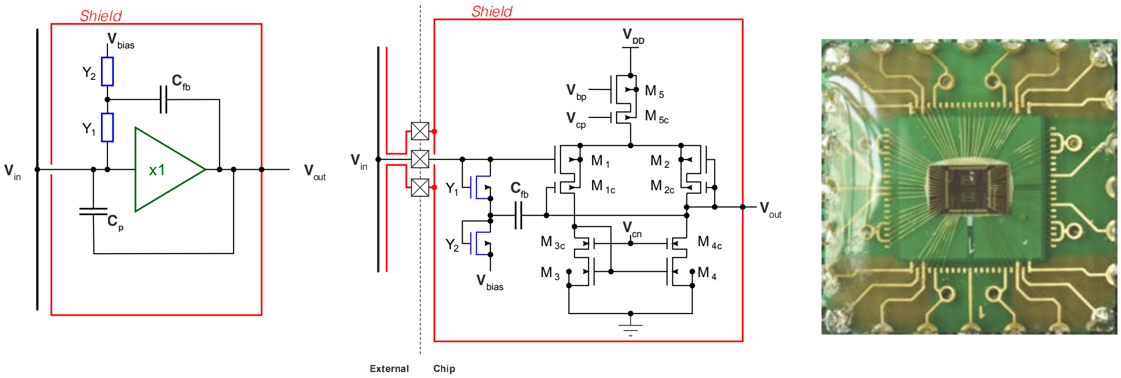

Sensor Concept **Circuit Design** **Fabricated IC and package**

Figure 5.5: (Left) Block diagram of the non-contact sensor front-end. Full access to every internal node of the amplifier allows for complete bootstrapping of parasitic input capacitances. (Middle) Circuit implementation of the front-end consisting of the input bias structure and modified operation amplifier in a 0.5 μm 2P3M CMOS process. See Table 5.1 for device dimensions. (Right) Fabricated IC encapsulated in a custom package which extends the internal shield structures to the PCB level and bootstraps the bond wires.

5.3 Circuit Design and Implementation

Figure 5.5 shows the block diagram of the sensor front end, the circuit schematic, and the fabricated and packaged IC.

The input of the sensor front end is a MOS transistor, i. e., its input impedance is capacitive. A unity gain amplifier bootstraps all parasitic input capacitances C_p and keeps the voltage across them constant. The output V_{out} of the unity gain amplifier also drives a shield that encloses the trace of the input V_{in} on the silicon die, its bond pads and wires, as well as its trace from the sensor electrode to the IC on the PCB. A stable DC operating point is established through a series connection of two extremely low conductance elements Y_1 and Y_2 between V_{in} and a bias voltage V_{bias} that is generated on chip.

The ultra-high impedance front end amplifier is a telescopic MOS operational transconductance amplifier in unity gain configuration. We chose PMOS input transistors because of better $1/f$ noise performance over NMOS transistors.

The input transistor M_1 is part of a differential pair in a separate n-well. Hence, the voltage across the dominant gate to source (and bulk) input capacitance $C_{gs,M_1} + C_{gb,M_1}$ remains essentially constant. To improve the bootstrapping of the source of M_1, the top current source M_5 is cascoded.

The voltage across the gate to drain capacitance C_{gd,M_1} is held constant by a cascode transistor M_{1c}. The gate of M_{1c} is biased by the output voltage V_{out}, which is connected to the gates of the self-cascode transistor $M_{2,2c}$ at the inverting input of the unity gain differential amplifier. To improve bootstrapping of C_{gd,M_1} and minimize offset $(V_{\text{out}} - V_{\text{in}})$, both the cascoded differential pair $M_{1,1c}$ and $M_{2,2c}$ and the cascoded NMOS current mirror $M_{3,3c}$ and $M_{4,4c}$ are laid out as common centroid structures.

A series connection of two high resistive MOS-bipolar pseudoresistors introduced by Delbrück and Mead [72] provides a DC path from V_{in} to V_{bias}. To minimize the loading of the input by the DC bias circuit by unshielded capacitances and leakage conductances, V_{in} is connected to the gate side of the first PMOS pseudoresistor Y_1, while its well is capacitively coupled to V_{out} through a feedback capacitor C_{fb}. A second pseudoresistor Y_2 connects this node to V_{bias}.

The feedback capacitor serves two purposes:

- C_{fb} forms a high-pass filter with Y_2, with the very long time constant $\tau_{\text{HP}} = C_{fb}/Y_2$.
- C_{fb} maintains a voltage of essentially 0 V across the nonlinear MOS-bipolar pseudoresistor Y_1 and keeps it in its region of extremely high resistance [73].

To bootstrap the routing capacitance of the V_{in} trace, we surrounded it by a shield connected to V_{out} both on the silicon die and on the printed circuit board. To minimize unshielded bond wire capacitance, the bond pad of V_{in} is surrounded by V_{out} pads on both sides.

A MOS-only reference circuit [74, 75] generates the bias voltages V_{bias}, V_{bp}, V_{cp}, and V_{cn} for a nominal current consumption of $1.6\,\mu$A per channel.

Table 5.1: Front-end Amplifier Device Dimensions

Device	Size
M_1, M_2	$4 \times \frac{120\mu m}{6\mu m}$
M_{1c}, M_{2c}	$4 \times \frac{120\mu m}{0.6\mu m}$
M_3, M_4	$4 \times \frac{1.8\mu m}{136.8\mu m}$
M_{3c}, M_{4c}	$4 \times \frac{1.8\mu m}{0.9\mu m}$
M_5	$16 \times \frac{3.6\mu m}{32.4\mu m}$
Y_1, Y_2	$\frac{1.5\mu m}{0.9\mu m}$
C_{fb}	200 fF

5.4 Characterization

5.4.1 Input Impedance and Bandwidth

To verify the input impedance of the amplifier, the transfer function of the amplifier was taken at different source impedances (short, 2 pF, 500 fF, and 250 fF). The midband gain is result of the voltage divider formed by the coupling and input capacitances, while the high-pass corner frequency is determined by the input resistance and the coupling capacitance. For this experiment, all the capacitors used were 0603 X7R ceramic capacitors soldered directly to the input of the package and accounts for all parasitics associated with the device. The experimental setup was contained within a Faraday cage, also connected to the active shield. If the cage was instead connected to ground, it would contribute an additional 5 fF of input capacitance.

The transfer function, as measured by a lock-in amplifier, is shown in Figure 5.6. The attenuation of the midband gain is consistent with an input capacitance of 60 fF. Remarkably, there is no frequency response attenuation down to 0.01 Hz at all coupling capacitances except 250 fF. This was accomplished completely without the need for neutralization or any manual tuning [11, 70]. Based on the corner frequency of the 250 fF measurement, it can estimated that the input resistance is approximately 50 TΩ.

A sample plot of the input and output signals to the amplifier of an 40 mV, 0.005 Hz sine wave coupled through 500 fF is shown in Figure 5.7. The extremely high input impedance of the amplifier allows it to successfully resolve low frequency signals through small coupling capacitances. The input bias structure also injects minimal

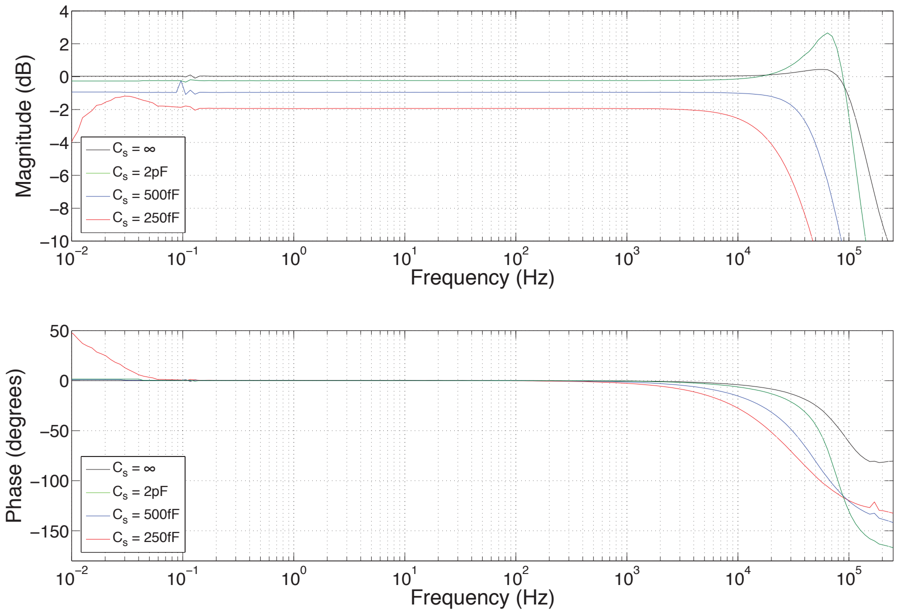

Figure 5.6: Measured transfer function of the sensor front-end at different source coupling capacitances.

leakage and drift noise into the signal, and the amplifier's input does not exhibit a large amount of drift even when the input node coupled with just 250 fF.

Another key consideration for high-impedance sensors is the input bias current. All amplifier inputs, even CMOS inputs, exhibit some finite bias current due to leakage currents, especially if the input node extends externally to the chip. Figure 5.8 shows the measured input current of the amplifier as the source was swept from 1.5 V to 2.5 V using a Keithley 6430 Sourcemeter. Over the operating range of the amplifier, the input current is minimal, normally less than ± 20 fA.

5.4.2 Noise

The completed amplifier's noise performance (including chip package) was measured at the same coupling capacitances as the frequency response. Measuring the voltage noise output across different source impedances allows for an estimate of the input voltage noise, the intrinsic input capacitance, and the input current noise. In this experiment, the output signal of the amplifier was AC-coupled with a corner frequency of

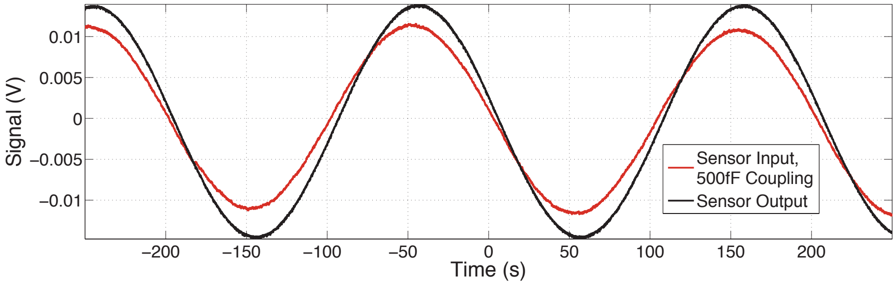

Figure 5.7: Sample segment of a 0.005 Hz sine wave coupled into the amplifier with a 500 fF source capacitance.

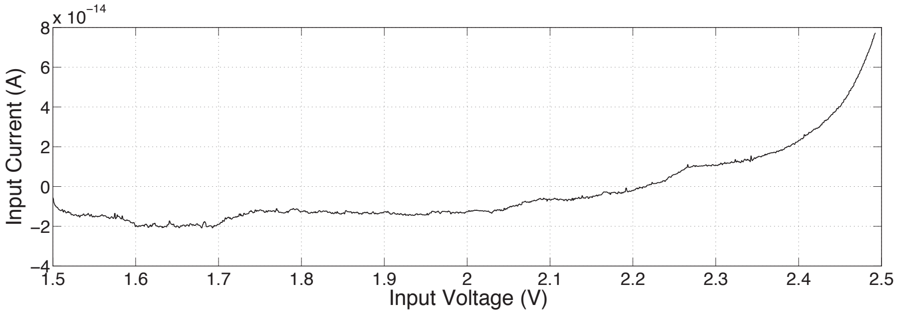

Figure 5.8: Measured input bias current versus input voltage.

0.05 Hz (minimizing low-frequency errors) to remove the DC offset and amplified with a gain of 500. The resulting output was digitized with a 24-bit ADC.

Figure 5.9 shows the estimated PSD of the input referred voltage noise (in this case, equivalent to the output noise since the amplifier gain is unity). The measured noise spectrum with an input short agrees with the predicted noise floor from simulation. Compared to the TI INA116 [76], the new integrated amplifier has a current noise specification that is 2.3× better than the TI INA116. The overall noise levels are approximately 9× better than current state-of-the art discrete sensor implementations [70]. The noise gain is also commensurate with an intrinsic input capacitance of 6 pF.

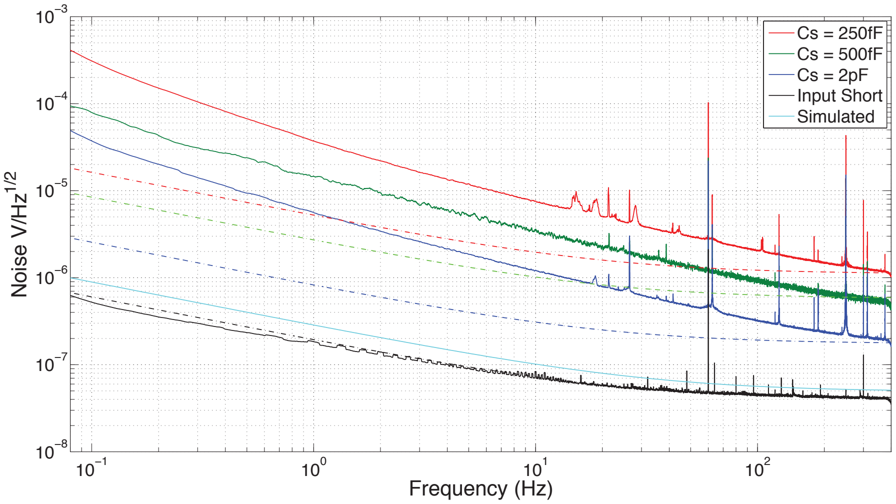

Figure 5.9: Measured noise spectra of the sensor at different coupling capacitances.

5.4.3 Comparative Validation on ECG Benchmark

To quantify the performance of the non-contact sensor under a realistic environment, we devised a simple protocol to simultaneously compare live ECG signals from multiple sensor types. Two standard Ag/AgCl electrodes (control group), an integrated amplifier sensor, a discrete sensor with input capacitance neutralization, and an identical discrete sensor with the neutralization network removed were all placed on the subject's forearm. Each of the electrodes were referenced against a single Ag/AgCl chest electrode, producing 5 output signals. Since the ECG potential is constant on the limb (verified via the two Ag/AgCl control electrodes), any discrepancy between the 5 output signals is the result of noise and distortion. A sample of the raw signal from each of the five electrodes tested is shown in Figure 5.10.

Table 5.2 shows the correlation coefficient, r, of the ECG signal between the different sensors versus the reference Ag/AgCl electrode. The data analyzed was taken over a 2.5 minute segment and bandpass filtered between 0.05Hz and 35Hz. The integrated amplifier shows significantly improved correlation compared to the discrete implementation. Similarly, Table 5.2 also shows the computed linear regression coefficient, b, between the various sensors and the Ag/AgCl reference to illustrate the gain error due to the effects of source-input impedance division. The integrated amplifier manages to

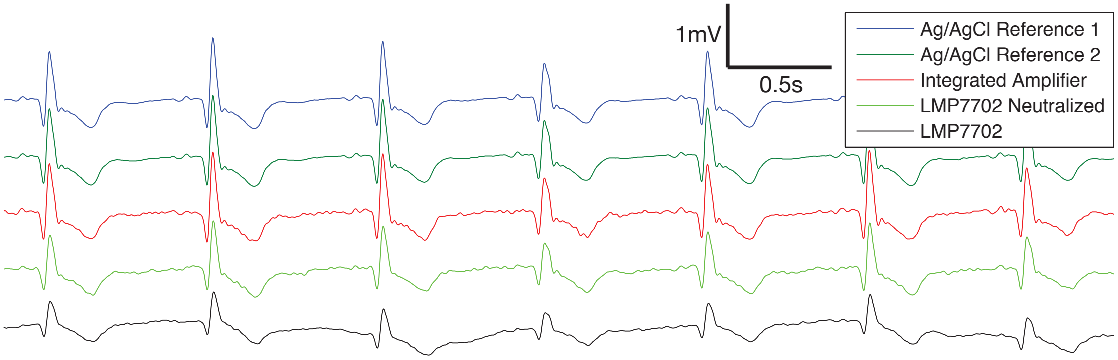

Figure 5.10: Sample segment of ECG acquired simultaneously (0.05Hz to 35Hz bandwidth)from five different electrodes placed on the forearm. The three non-contact electrodes were placed on top of a cotton sweater. All the electrodes were referenced against a common chest electrode. The two discrete based non-contact sensors show signal attenuation due to the it's input capacitance. The new fully bootstrapped, integrated sensor maintains the same signal amplitude as the reference hydrogel Ag/AgCl electrodes, although with greater noise due to the cotton interface.

maintain a high degree of gain accuracy even through the high source impedance of the cotton sweater and is significantly superior to both the neutralized and unadjusted discrete sensors.

Figure 5.11 plots both a raw sample of the error, defined as the difference between each of the electrodes and the Ag/AgCl reference, as well as its power spectra (over the entire 2.5min segment). Unsurprisingly, the difference between the two Ag/AgCl electrodes is negligible. The integrated amplifier has a significantly increased noise floor, in large part due to the noise from the cotton interface [59], but is nonetheless broadband in nature. Significant CMRR errors are visible in both discrete implementations as a result of their relatively large input capacitance. The integrated amplifier, while nosier, represents a fundamentally much more faithful reproduction of the signal due to its low input capacitance.

Table 5.2: Measured ECG Correlation

Sensor	*r*	*b*
Ag/AgCl vs. Ag/AgCl	.992	.999
Ag/AgCl vs. Integrated	.953	.996
Ag/AgCl vs. Discrete (Neutralized)	.918	.865
Ag/AgCl vs. Discrete	.715	.541

5.4.4 EEG Signal Validation and SSVEP BCI Example

As a validation of the sensor for EEG BCI and monitoring applications, a simple alpha wave experiment was used. Figure 5.12 shows spectrograms of EEG data taken during a trial where a subject was asked to close their eyes from the segment spanning 5 to 20 seconds into the trial. The integrated sensor was able to resolve alpha waves through hair over the occipital region. The presence and absence of alpha activity was confirmed by an Ag/AgCl control electrode placed on the forehead.

Steady-state visual evoked potential experiments are effective at verifying the performance of EEG sensor systems since it relies on detecting known and controlled narrowband stimuli. In addition, it also serves as a common BCI paradigm, including one previous capacitive-type system [77].

For the experiment, the integrated amplifier electrode was mounted in a relatively loose fitting headband over the Oz location. A second Ag/AgCl electrode was placed on the forehead at Fp1 and used as a reference. The subject was presented with a 4 by 3 grid of SSVEP stimuli boxes delivered on a computer screen. Each box flashed a different frequency ranging from 9 to 12 Hz. The subject was asked to sequentially focus on each box on the grid. In effect, this performs a SSVEP 'tone sweep' stimulus which should be readily visible in the EEG specta.

Figure 5.13 shows the spectrogram on the acquired EEG. The SSVEP is signal is readily visible, although it is punctuated with a movement artifact partially into the trial. However, it can be seen that the integrated amplifier is fully able to resolve the SSVEP signal to at least 0.25Hz even through hair. To our knowledge, this degree of

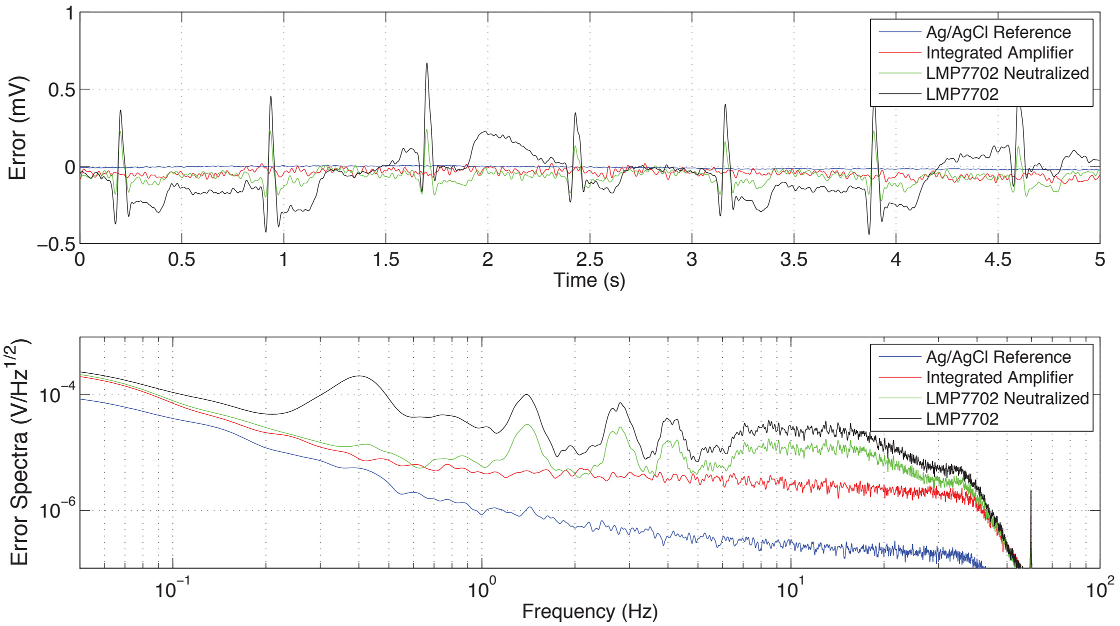

Figure 5.11: Residual error of the signal acquired by the different sensors from the reference Ag/AgCl electrode. The standard discrete electrodes show a significant ECG component, indicating gain error arising from their large input capacitance. The integrated amplifier has greater broadband noise, but successfully preserves the signal gain even through a thick layer of cotton.

signal quality has yet to be demonstrated with other reported non-contact EEG sensor systems, and serves as a proof-of-concept for future, non-contact based EEG arrays.

To demonstrate the amplifier in a high-resolution, non-contact EEG context, an array of 4 non-contact electrodes with the integrated amplifier were used to acquire a 7-lead ECG, through clothing, on a resting subject. At the same time, four standard wet adhesive Ag/AgCl electrodes were placed adjacent to each of the non-contact electrodes to enable a direct comparison with a simultaneous reference ECG. The ECG outputs, through a 0.05 Hz to 35 Hz bandpass filter, are shown in Figure 5.14.

In contrast to the previous generation of non-contact sensors, the new electrode with the integrated front-end easily maintains a stable baseline, even down to 0.05 Hz. Likewise, the high input impedance made possible by the integrated amplifier fully preserves the signal amplitude and does not introduce extra distortion in the frequency

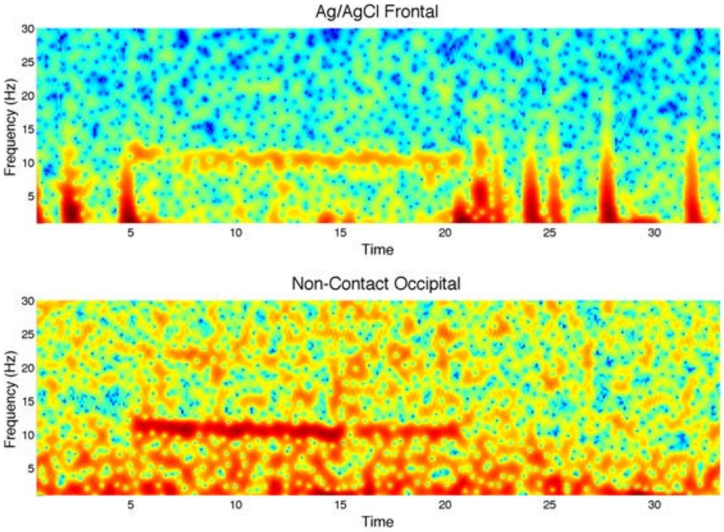

Figure 5.12: Spectrograms of simultaneously recorded EEG signals over a one second sliding window. The electrode with the integrated amplifier was placed on top of hair in the occipital region along with an Ag/AgCl electrode on the forehead. Both electrodes were referenced against the mastoid. Alpha rhythms are visible after the subject was asked to close his eyes.

response. Unlike previous discrete designs [59, 70], the integrated amplifier easily achieves AAMI ECG frequency response requirements completely without the need for manual adjustment.

5.5 Discussion

The integrated non-contact front-end performs significantly better than discrete designs. Table B.1 summarizes the measured characteristics of the front-end. By investing resources at the design stage, it is possible to build superior non-contact electrodes that are much simpler and require no adjustment. Further refinement of this technology can potentially lead to practical non-contact sensor arrays that bypass many of the limitations and difficulties in this field.

Chapter Five is an amalgamation of material submitted to the 2011 IEEE Circuits and Systems - Forum on Emerging and Selected Topics Workshop and the IEEE 2011

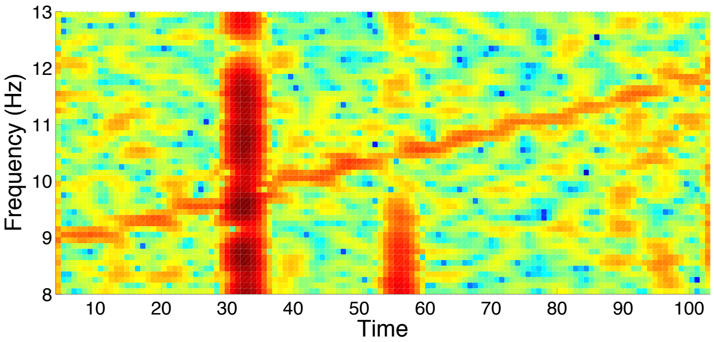

Figure 5.13: Spectrogram from a typical SSVEP BCI-type experiment. An integrated non-contact sensor was placed on the back of the head, on top of hair, and referenced against a forehead electrode. The spectrogram was taken with a 6 s sliding window.

IEEE European Solid-State Circuits Conference plus significant additional text. Y. M. Chi, C. Maier and G. Cauwenberghs, "Integrated Ultra-High Impedance Front-end for Non-contact Biopotential Sensing," *IEEE European Solid State Circuits Conference* (Submitted). Y. M. Chi, C. Maier and G. Cauwenberghs, "An Integrated, Low-noise, High-Input Impedance Front-end for Capacitive Non-contact Physiological and BCI Sensor Systems," *IEEE Circuits and Systems-Forum on Emerging and Selected Topics*, May 2011. The author is the primary author and investigator of this work.

Table 5.3: Integrated Amplifier Specifications

Specification	This Work (measured)	TI INA116 [76]
Process	0.5 μm 2P3M CMOS	TI BiFET
Input Resistance	$> 50\,\mathrm{T\Omega}$	$> 1\,\mathrm{T\Omega}$
Input Capacitance	60 fF	2 pF
Voltage Noise at 1 kHz	$45\,\mathrm{nV}/\sqrt{\mathrm{Hz}}$	$28\,\mathrm{nV}/\sqrt{\mathrm{Hz}}$
Voltage Noise at 1 Hz	$200\,\mathrm{nV}/\sqrt{\mathrm{Hz}}$	$1\,\mu\mathrm{V}/\sqrt{\mathrm{Hz}}$
Current Noise at 1 Hz	$0.05\,\mathrm{fA}/\sqrt{\mathrm{Hz}}$	$0.13\,\mathrm{fA}/\sqrt{\mathrm{Hz}}$
Bandwidth (G = 0 dB)	100 kHz	800 kHz
Offset	0.5 mV	2 mV
Power Supply (1 channel)	1.5 μA at 3.3 V	2 mA at 9 V

Figure 5.14: Sample 7-lead ECG taken simultaneously with the integrated non-contact front-end (red trace) and standard wet Ag/AgCl electrodes (blue trace). The integrated sensor fully matches the frequency response and gain of the wet electrodes. Data is shown over a 0.05 Hz to 35 Hz bandwidth.

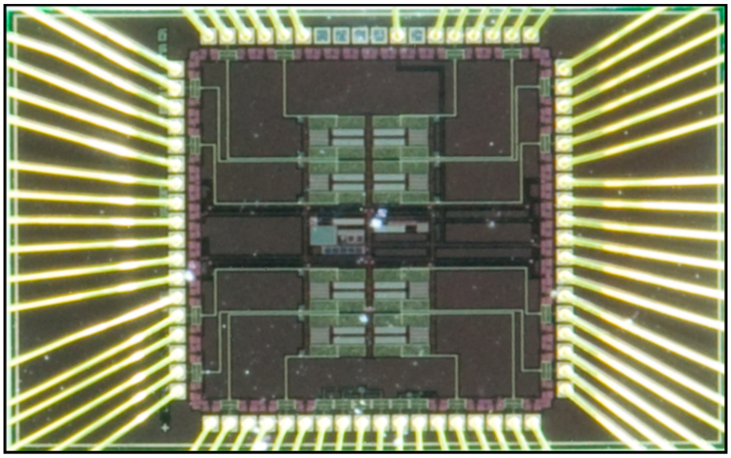

Figure 5.15: Micrograph of the fabricated chip. Each die contains 16 channels and an on-chip current reference.

Chapter 6

Integrated Bioamplifier and ADC

6.1 Introduction

Wireless and implantable biomedical devices are becoming increasingly important for healthcare and research. Wearable, unobtrusive ECG/EEG systems allow patients to screen their vital signs for abnormalities during their daily lives. High density multichannel implantable neural electrodes benefit researchers in understanding the nervous system and will be integral to future neuroprosthetics to help the disabled. Advancements in ultra-low power, integrated circuits has is a key driving force in this field.

The analog front-end consisting of the amplifier and ADC is a one major component in a biopotential acquisition system. For miniature wireless battery powered devices, minimizing the power and complexity of the analog front-end is still a challenge.

To date, several authors have built innovative integrated solutions for multichannel biopotential recordings using the approach of a low noise preamplifier [73] followed by an ultra-low power SAR [78] or $\Delta\Sigma$ ADC [79]. It is possible to achieve excellent noise efficiency specifications [80] [81] [82] as well as very high channel densities [83].

In addition, single chip, commercial multi-channel ECG/EEG products have also appeared on the market with very high resolution, but a relatively large power consumption of around 1 mA/channel. [84]

However, nearly all currently known bioamplifier circuits are designed to drive a separate ADC block, with the exception of [85] which produces pulse delay modulated output. Thus, there are two primary sources of power and complexity in the typical analog front-end. The amplifier section consumes up to several microamperes of current, and is dictated by the noise requirement. The ADC section itself will require separate circuits and will also consume up to tens of microamperes per ADC channel [79]. For future integrated systems, an even more efficient solution is desirable.

In this work, we introduce a new bioamplifier circuit that configures the OTA normally used as just as the amplifier into also functioning simultaneously as an incremental $\Delta\Sigma$ ADC. By integrating the amplifier within the ADC, there is no need to drive any portion of the analog front-end beyond Nyqusit rate and and an explicit anti-alias filter is not needed. The BioADC interfaces directly with unbuffered, μV levels signals from the body and provides a digitized output.

The BioADC reduces the complexity and power of the analog-front end for biopotential systems by integrating the amplification and digitization of signals into one circuit. The main source of static power dissipation is from biasing the core OTA, which sets the noise levels, the same as conventional systems. Power and area for separate, dedicated ADC circuits are eliminated. We were able to achieve a total power consumption of less than 20 μW per channel without compromising on noise and resolution.

6.2 System Overview

The BioADC is a complete amplifier front-end that directly outputs digital codes from input signals down to the microvolt levels. To understand the principle behind the BioADC, it is useful to first examine the conventional integrated bioamplifier [73, 79] shown in Figure 6.1. Normally, the first stage consists of a differential amplifier with a gain (40-60 dB) fixed by the ratio of the feedback capacitors. After the DC-offset and common-mode interference is removed by the first stage, a second stage, which may also have gain, further buffers the signal and usually drives the input of a shared SAR-type ADC. Although this design has been highly successful and SAR ADCs consume a minimal amount of power, this architecture still fundamentally requires multiple amplifier stages. In addition, the buffer/LPF stage must have enough drive to charge the ADC's input capacitors at a high-speed, especially if multiple amplifiers must share the same

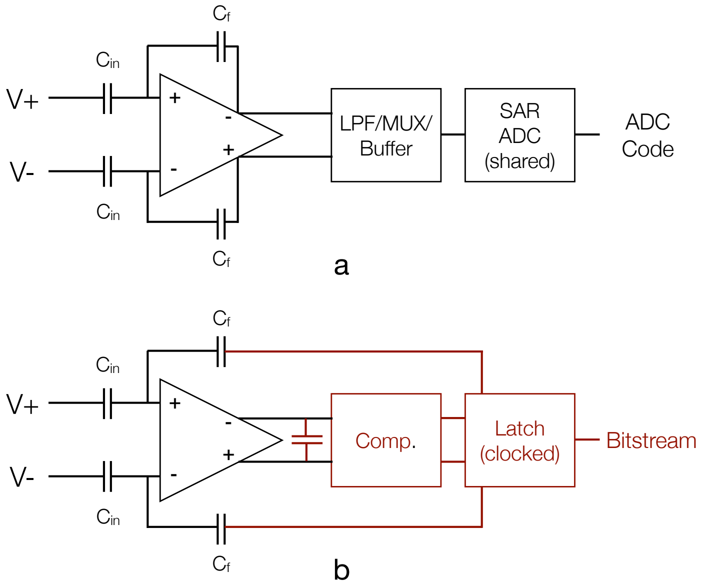

Figure 6.1: Complete schematic of the BioADC for a single channel. Inputs are AC coupled to the input's of the OTA which have dynamic auto-ranging and offset correction through an increment/decrement circuit [86]. The OTA serves as the integrator of the incremental ΔΣ ADC. The amount of feedback from the comparator's decision applied back to the OTA input's is digitally controlled to precisely set the gain.

converter.

In contrast, the BioADC dispenses with the need for both additional buffers or an external ADC. Instead, the entire signal chain is folded within the feedback loop of a single OTA. Like the conventional design, the BioADC incorporates capacitive feedback to set the gain of the amplifier.

6.3 Circuit Design

The core of the BioADC consists (Fig. 6.2) of an OTA, a comparator, data latches and the input coupling and feedback capacitors. Signals from a differential pair of recording electrodes are directly connected to the on-chip capacitors, C_{in}, at the OTA's input. The comparator and feedback capacitors complete the incremental ΔΣ feedback

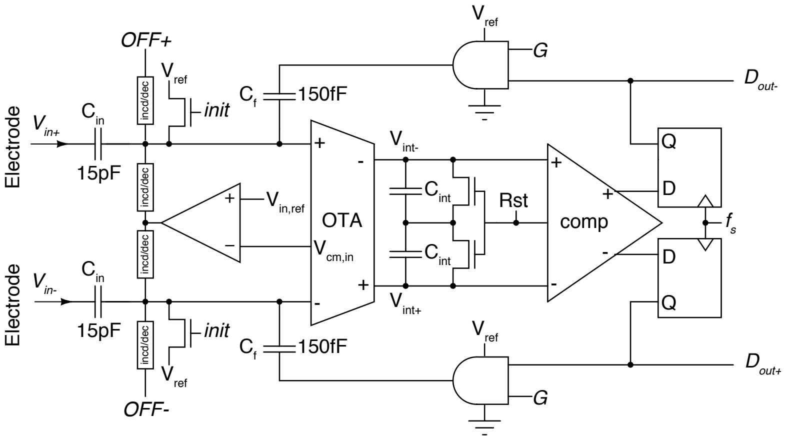

Figure 6.2: Complete schematic of the BioADC for a single channel. Inputs are AC coupled to the input's of the OTA which have dynamic auto-ranging and offset correction through an increment/decrement circuit [86]. The OTA serves as the integrator of the incremental ΔΣ ADC. The amount of feedback from the comparator's decision applied back to the OTA input's is digitally controlled to precisely set the gain.

loop. The digital output from the BioADC is taken from the comparator's latch. In this version, only the core analog circuitry is on-chip and the digital timing, control logic and biases were implemented on the test PCB.

6.3.1 Incremental ΔΣ ADC

A first order, continuous-time, incremental ΔΣ ADC is formed through the OTA, which serves as a resettable $G_m - C$ integrator, a comparator and a negative feedback loop through C_f.

The timing diagram for one sample is shown in Figure 6.3. A sample begins with a pulse (Rst) which resets C_{int} and simultaneously nulls the comparator and OTA offset. The signal is integrated for a period of T_s which ends with a pulse to latch the comparator's decision.

Depending on the integrated voltage, either D+ or D- is asserted high. Because both the inputs and comparator decision are capacitively coupled, the summing node which combines the signal and the ΔΣ negative feedback can be implemented right at the

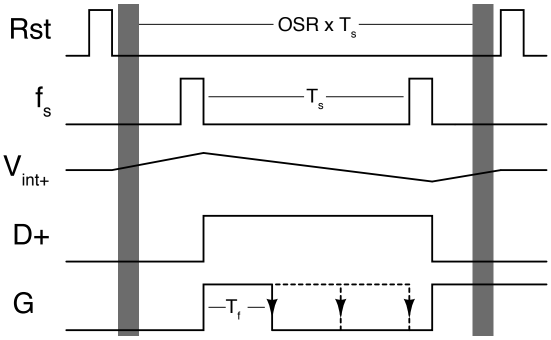

Figure 6.3: Timing diagram showing the integrator reset, the integration and decision of one sample and the digital gain control. The duty cycle of G controls the amount of feedback applied in the $\Delta\Sigma$ loop. The signals for one half of the fully differential circuit is shown.

OTA's input.

The voltage at the output of the OTA integrator over one period, T_s, can be written as,

$$V_{int} = \frac{g_m}{2C_{int}} \int_0^{T_s} V_{in}(t)\frac{C_{in}}{C_t}dt \pm \frac{g_m}{2C_{int}} \int_0^{T_f} V_{ref}\frac{C_f}{C_t}dt \tag{6.1}$$

where the polarity of the second term is controlled by the comparator's last decision, g_m is the OTA's transconductance and C_t is the sum of the capacitances at the OTA's input (including parasitics).

The full scale code for the incremental ADC is set by the amount of feedback applied in the loop and is controlled by the supply voltage and the duty cycle of G (T_f/T_s) resulting in full-scale input of,

$$V_{range} = 2\frac{C_f}{C_{in}}\frac{T_s}{T_f}V_{ref}. \tag{6.2}$$

A total of (OSR-1) periods is integrated and quantized before reseting the integrator. Summing the periods that D_{out+} is high represents a (OSR-1)-bit resolution code for the input signal over a single sample, completing the operation of the incremental ADC. The circuit cannot function reliably as a conventional $\Delta\Sigma$ ADC since the OTA and comparator's DC operating points need to be periodically refreshed.

The gain is ratiometric and set by the sizes of C_{in} (15 pF) and C_f (150 fF) and independent of PVT, bias current and parasitic input capacitances. The two variables

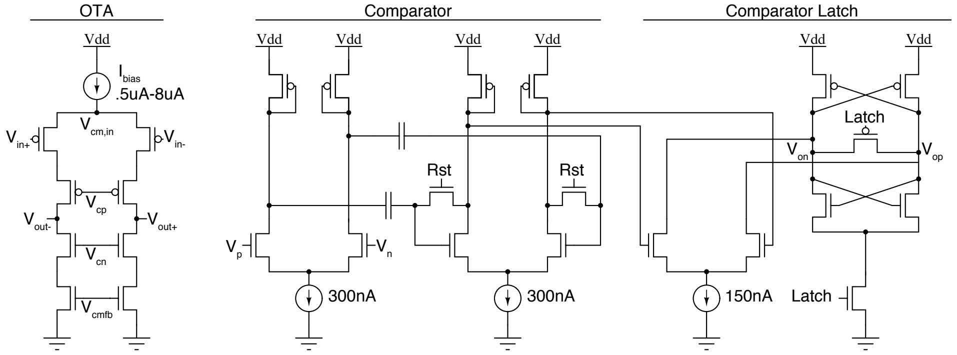

Figure 6.4: Transistor level schematics of the OTA and latched comparator. The main source of static power consumption is the DC biasing current of the OTA which sets the fundamental noise limits.

that control the full-scale range of the BioADC, and hence gain, V_{ref} (nomially set at V_{dd}) and the duty cycle of G (T_f/T_s). Thus, the gain can be well defined and easily tuned through digital control. With the BioADC, it is possible to have full-scale input ranges of less than 1 mV differential, allowing for small μV signals to be directly connected to the BioADC.

The BioADC combines the advantages of several previous implementations of bioamplifiers and ADCs, while integrating both functions with a single core analog OTA for optimal power efficiency. A typical low-noise bioamplifier [73] [79] will also consist of an OTA along with signal coupling capacitors C_{in} and C_f arranged in negative feedback to set the closed loop gain. The addition of the explicit OTA load capacitance, C_{int} and comparator in the feedback loop, essentially operates the circuit as a class-D bioamplifier. In combination with the $\Delta\Sigma$ feedback, the switched output of the BioADC is directly provides a digital output.

The fabricated chip (Fig. 6.11) containing two separate channels was tested for distortion and noise performance using a simple custom PCB with a USB data acquisition circuit. The chip was also connected directly to electrodes placed on a subject to collect live physiological data.

6.3.2 OTA and Comparator Circuits

Figure 6.4 depicts the transistor level schematics for the core OTA and latched comparator for the BioADC. The OTA is a standard, fully-differential cascoded amplifier. The input PMOS pair was sized with an extremely large W/L (480/1.5) ratio and operated in subthreshold. All the other devices are sized to be long, and operated in strong inversion such that the noise should be dominated by the input pair alone [73]. CMFB is accomplished by taking common-mode of the output signal available at the node in-between the two integration capacitors, C_{int} with the DC level restored during the normal reset phase of the BioADC.

The bias current of the OTA that sets the noise floor of the BioADC is nominally between $.5\mu A$ and $8\mu A$. This biasing current is normally the largest source of static power dissipation.

A latched comparator is used as the quantizer for the $\Delta\Sigma$ modulator and consists of two preamplifier stages followed by a positive feedback latch circuit [87]. The first and second pre-amplifier stages are capacitively coupled and reset at the same time as the OTA integrator. This dynamically cancels the comparator and OTA offset as part of each sample conversion. A total of 750 nA is used to bias the latch's preamplifiers.

6.3.3 Input Coupling

A reset switch is enabled only at power-up to initialize the voltage at the OTA's input to a known value, V_{ref}. During normal operation, the input nodes of the OTA are left at a very high impedance. If unattended, leakage currents at the OTA's input will cause drift, both common and differential, at the OTA's input, eventually leading to failure.

To control the OTA input node voltages, two sets of increment/decrement update circuits [86] are utilized as a way to dynamically inject small amounts of correcting current. The increment/update circuits are built from a NMOS and PMOS transistor placed in parallel with their gates respectively tied close to ground.

For common mode control, the voltage at the source of the OTA input pair, $V_{cm,in}$ (Fig. 6.2 and Fig. 6.4), is monitored and compared to the desired level, $V_{in,ref}$. The comparator for the common-mode control circuit is a simple 1-stage OTA biased with only 50 nA of current and does not contribute a significant amount of power.

Differential offsets are dynamically canceled by negatively feeding back the output bitstream into the differential increment/decrement network (OFF+, OFF-). The increment/decrement circuit contributes a small amount of current into the input node, $\pm i_{off}$, removes the DC-offset and stabilizes the operating point of the OTA's input node. The total amount of feedback applied during each sample is proportional to the output ADC code. In effect, it performs the same function as a biasing resistor but avoids the difficulty of implementing of an appropriately large-valued resistor on-chip ($> 100G\Omega$). It is easy to see the high-pass transfer function implemented by this structure by writing the input voltage of the OTA, V_i, as a function of both the source signal, V_s, and the offset correction current, i_{off},

$$\frac{dV_i}{dt} = \frac{dV_s}{dt}\frac{C_s}{C_s+C_f} - \frac{V_i}{V_{range}}\frac{i_{off}}{C_s+C_f}, \tag{6.3}$$

where the differential change at the input node is the sum of the differential change of the signal source plus the effect of negative feedback due from the increment/decrement circuit. Rearranging and writing it in the frequency domain yields the following single-pole high-pass transfer function,

$$\frac{V_i(s)}{V_s(s)} = \frac{C_s}{C_s+C_f}\frac{s}{s+\frac{i_{off}}{V_{range}(C_s+C_f)}}, \tag{6.4}$$

with a high-pass corner of,

$$f_{hp} = \frac{i_{off}}{V_{range}(C_s+C_f)}. \tag{6.5}$$

Using this model, it is estimated that the implemented correction current is approximately $75fA$.

6.3.4 Input Impedance and Bias Current

For physiological recording applications, the input impedance specifications of the amplifier are often an important consideration. The lack of sampling capacitors means that the BioADC does not require a low-impedance source to charge and discharge a conventional ADC's input. However, the switching action of the feedback network does draw a small, but non-negligible, amount of current from the source. Examining the input node, it can be seen that the current draw during each sample is,

$$i_{in} = \frac{1}{2} V_{range} C_s f_s N, \tag{6.6}$$

where N is the number of output bit transistions during the sample. Since the number of transitions during a sample is not directly proportional to the output code, the dynamic resistance of the BioADC's input is not well defined. However, it is possible to estimate the worst case current draw by simply assuming that the BioADC switches during every cycle. At a master clock of 524.288 kHz and a maximum range of 20 mV, this corresponds to an input current of 80 nA - comparable to a BJT input stage.

The worst case input resistance can also be obtained by assuming a change from zero transitions in the output code during one sample and followed by a sample with a maximal number of transitions,

$$R_{in,min} = \frac{1}{C_s f_s (OSR - 1)}. \tag{6.7}$$

This corresponds to a minimal input resistance of 128k Ω using the same parameters as before.

6.4 Experimental Results

Since the BioADC acts as both amplifier and digitizer, it is important the characterize the key specifications of the circuit for both domains.

6.4.1 Distortion and Resolution

Since the BioADC is fundamentally an AC coupled system, the INL and DNL of the ADC are difficult to determine with traditional methods. In addition, it is not possible to define DC specifications of the circuit, since the input structure automatically removes DC stimuli. In practice, this is not a serious limitation since the majority of biopotential signals are AC in nature.

Non-linearities in the differential pair of the OTA are the primary contributors the distortion within the BioADC. To quantify these effects, a single tone test is used

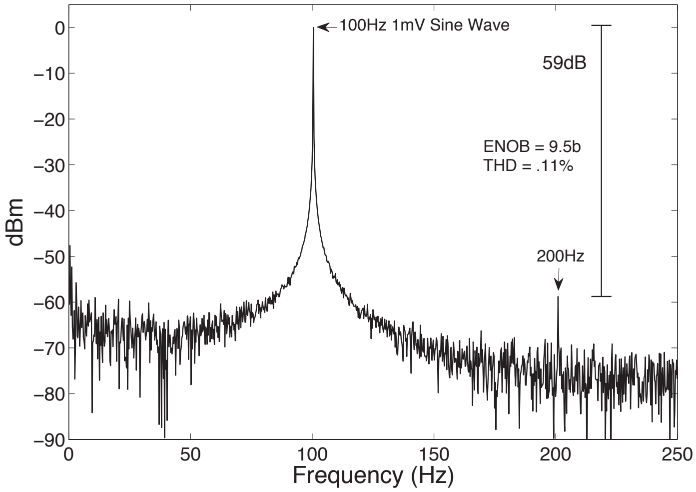

Figure 6.5: Single tone test at 100 Hz. The BioADC achieves an ENOB of 9.5 b when operating an oversampling ratio of 2^{10} and an output data rate of 512 Hz.

to measure the level of distortion for AC signals, which is relevant for it's intended use cases. The FFT of a $100Hz$, $1mV$ input signal is shown in Figure 6.5. For this test, the BioADC was set to operate at an oversampling ratio of 2^{10} which corresponded to a post decimation sample rate of 512Hz. The gain setting was set such that the full-scale code was just slightly higher than the 1mV input tone.

Overall distortion levels are low, and the BioADC achieves an ENOB of $9.5b$ for a $1mV$ full scale input, which is more than sufficient for the majority of biopotential recordings. Distortion levels will rise as V_{range} is increased due to the larger magnitudes of the input and feedback signals.

6.4.2 Frequency Response

The bandwidth of conventional bioamplifier's is set by the g_m of the input stage and it's load capacitance. For the BioADC, which outputs discrete-time digital codes, the bandwidth is ultimately dictated by the sampling rate of the incremental converter.

The measured frequency response of the BioADC is shown in Figure 6.6. Even without an explicit low-pass filter at the BioADC's input, the decimation filter (counter) of the incremental ADC acts as a discrete time moving average filter with nulls at integer

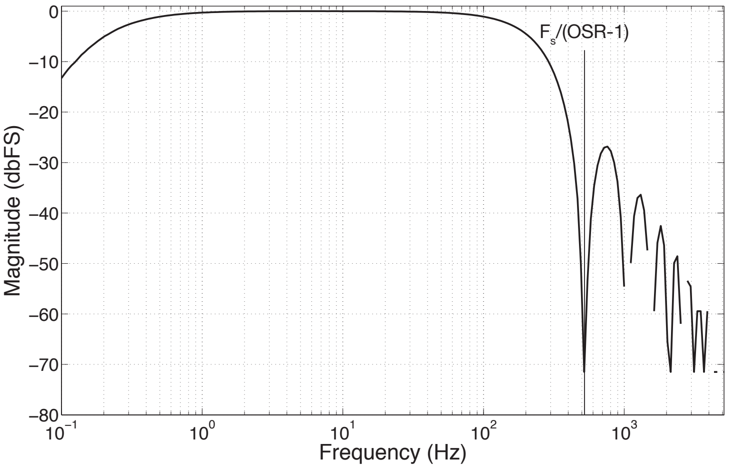

Figure 6.6: Single tone test at 100 Hz. The BioADC achieves an ENOB of 9.5 b when operating an oversampling ratio of 2^{10} and an output data rate of 512 Hz.

multiples of the sample rate [88]. While this eliminates the need for external filters and buffers, the moving average filter does not as strongly attenuate frequencies at the edge of the signal band as strongly as an explicit anti-alias filter. Nevertheless, this removes the need for external filters, active or passive, at the input and is sufficient for many applications.

The high-pass corner frequency is set by the correction current of the input bias structure and is approximately 0.2 Hz, in the current implementation. In practice this can also be tuned by adjusting the bias voltages on the increment/decrement switches.

6.4.3 Noise

The noise behavior of the BioADC is determined by multiple noise sources. At coarse quantization levels (large V_{range}), the BioADC works mostly as a quantizer and is dominated by quantization noise. As the input range decreases, the BioADC starts to behave mostly as an amplifier and is dominated by circuit noise from the OTA and input structures. Proper design of the OTA can further ensure that the OTA's noise levels are determined mostly by the input pair alone. Both of these noise mechanisms are well understood. Finally, additional $1/f^2$-like noise is also introduced by the input offset and bias network, which contributes shot noise from the leakage currents and is integrated onto the coupling capacitors.

The input-referred noise due to quantization error from the incremental ADC follows from the standard noise equation at a given sample rate and LSB step,

$$v_{n,adc} = \frac{\frac{V_{range}}{OSR+1}}{\sqrt{\frac{12f_s}{OSR+1}}}\Delta f. \tag{6.8}$$

Similarly the thermal noise (neglecting the contribution of the cascode devices) of the OTA follows standard noise analysis,

$$v_{n,OTA} = \frac{C_s+C_f+C_p}{C_s}\frac{16kT}{3}\frac{1}{g_{m1}}(1+\frac{g_{m4}}{g_{m1}})\Delta f, \tag{6.9}$$

where the capacitive divider accounts for the signal attenuation from the the BioADC's inputs to the OTA through the capacitive feedback network and other parasitic capacitances (C_p). Since the coupling capacitors are much larger than the feedback capacitors and any parasitics, it is convenient to simply set this as unity in further analysis. In addition, given the aspect ratio of the input device pair versus the tail current sources, it is expected that the term g_{m4}/g_{m3} is minimal.

The lack of sampling capacitors in the BioADC's structure avoids kT/C noise common to most ADCs. However, the capacitively coupled structure of the BioADC's input and summing node is susceptible to shot noise from leakage currents. Any current noise at the OTA's input converts to voltage noise across the coupling capacitors, which present a high-impedance at low-frequencies. At a given correction current, I_{off}, there also exists an associated shot noise power, $2qI_{off}$. The input referred noise is,

$$v_{n,leak} = \frac{C_s+C_f+C_p}{C_s}\frac{\sqrt{2qI_{off}}}{\omega(C_s+C_f+C_p)}\Delta f, \tag{6.10}$$

noting again the capacitive divider ratio from OTA's input node to the BioADC's input. In this case, the entire expression simplifies such that only the C_s term remans in the dominator.

The aggregate effect of all the noise generators obtained by simplifying then summing is

$$v_{n,in}^2 = [\frac{V_{range}^2}{12f_s(OSR+1)}+\frac{16}{3}\frac{kT}{g_{m1}}+\frac{4qI_{off}}{\omega^2C_s^2}]\Delta f. \tag{6.11}$$

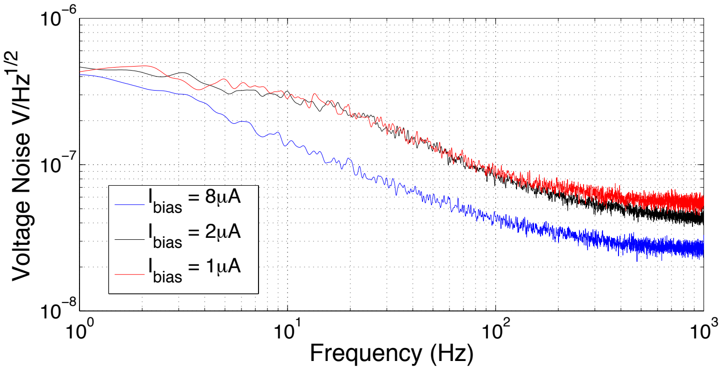

Figure 6.7: Input referred voltage noise of the BioADC at an OTA bias current of 1 μ A and 8 μA. The BioADC achieves an NEF of 3.1 and an input referred noise of 2.6 μV$_{rms}$ at I_{bias} = 1 μA. The theoretical white noise limit, $2qI_{bias}/g_m^2$, of a subthreshold MOS transistor is also shown.

In addition to the intrinsic noise sources in the BioADC, as described above, it is also possible that the switching action of the quantizer and latches in the feedback network coupled additional noise into the system. To measure the total noise spectra of the BioADC, the inputs were shorted to ground and the output codes were measured. To minimize the effects of quantization noise, V_{range} was set to a minimal level.

The ADC's noise floor was measured by shorting both differential inputs to ground and recording the output data stream. Figure 6.7 shows the input-referred voltage noise density for OTA bias currents of 1 μA and 8 μA.

The noise at low frequencies is mainly dominated by $1/f$ noise of the input transistors as well as noise from leakage currents from the increment/decrement circuit. At higher frequencies, the levels approach the thermal noise limits of the input differential pair.

A noise efficiency factor of the ADC is 3.1 at a bias current of 1 μA and a total input referred voltage noise of 2.6 μV$_{rms}$ is measured. At a bias current of 1 μA, the BioADC approaches the fundamental thermal noise floor of the subthreshold input pair showing that the addition of the ADC circuits does not significantly degrade the noise performance. The overall performance of the BioADC is comparable to the best integrated bioamplifiers reported to date.

Figure 6.8: Artificial (top) and live ECG (bottom) signals acquired by the BioADC. Passive AgCl clinical adhesive electrodes on the subject's were connected directly to the BioADC's inputs. The subject was also passively connected to circuit ground through a third AgCl electrode.

6.5 Physiological Measurements

Live ECG data was acquired by connecting the differential inputs of the ADC directly to a subject's chest via purely passive Ag/AgCl electrodes (3M Red Dot). The recorded data can be seen in Fig. 6.8 along with a recording of an artificial ECG from a signal generator.

6.6 Discussion

We present a low power amplifier/ADC specifically suited for wireless and implantable biomedical devices. The biopotential acquisition circuit accepts unbuffered signals and performs both amplification and digitization using just one core OTA. Overall performance in terms of power, noise and resolution is comparable to standard bioamplifier circuits with an analog output. The BioADC provides a simple, efficient circuit to build highly integrated, multi-channel biopotential acquisition systems.

Chapter Six is an expansion of material published in the 2010 IEEE European Solid-State Circuits Conference: Y. M. Chi and G. Cauwenberghs, "Auto-ranging Incremental Delta Sigma ADC," *IEEE European Solid State Circuits Conference*, September 2010. The author is the primary author and investigator of this work.

Table 6.1: BioADC Chip Specifications

Process	0.5 mum CMOS
Full-scale Input Range	$\pm$ 1 mV to $\pm$ 30 mV
Sampling Rate	128 Hz to 2.048 kHz, f_s = 523.776 kHz
Frequency Response	1 Hz to Nyquist
Resolution	8 b (2.048 kHz) to 12 b (128 Hz)
Distortion	9.5 ENOB and .11 % THD, OSR=1023
CMRR	$\geq$ 80 dB
Input Referred Noise	2.65 μV at I_{bias} =1 μA, OSR=1023
NEF	3.1 at I_{bias}=1 μA, OSR=1023
OTA Bias	.5 μA to 8 μA
Power (1 ch, static)	6.6 μW, I_{bias}=1 μA
Power (1 ch, dynamic)	<20 μW, I_{bias}=1 μA, OSR=1023
Power (Chip)	150 μW

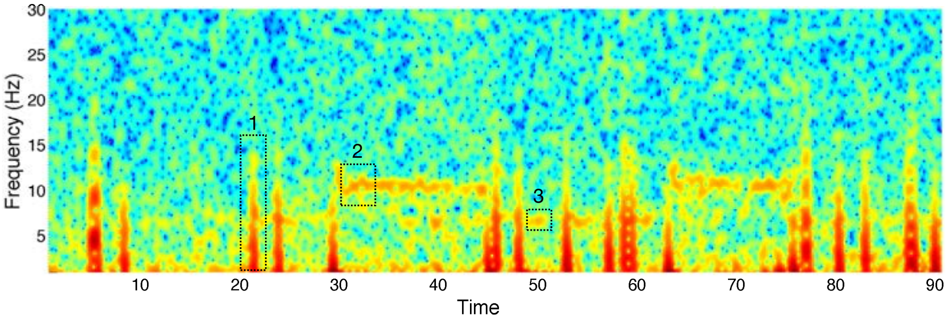

Figure 6.9: Artificial (top) and live ECG (bottom) signals acquired by the BioADC. Passive AgCl clinical adhesive electrodes on the subject's were connected directly to the BioADC's inputs. The subject was also passively connected to circuit ground through a third AgCl electrode.

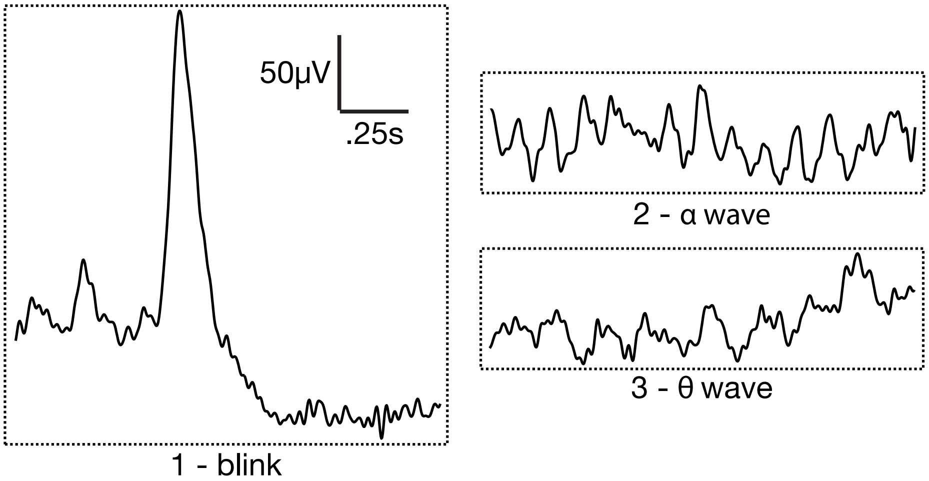

Figure 6.10: Artificial (top) and live ECG (bottom) signals acquired by the BioADC. Passive AgCl clinical adhesive electrodes on the subject's were connected directly to the BioADC's inputs. The subject was also passively connected to circuit ground through a third AgCl electrode.

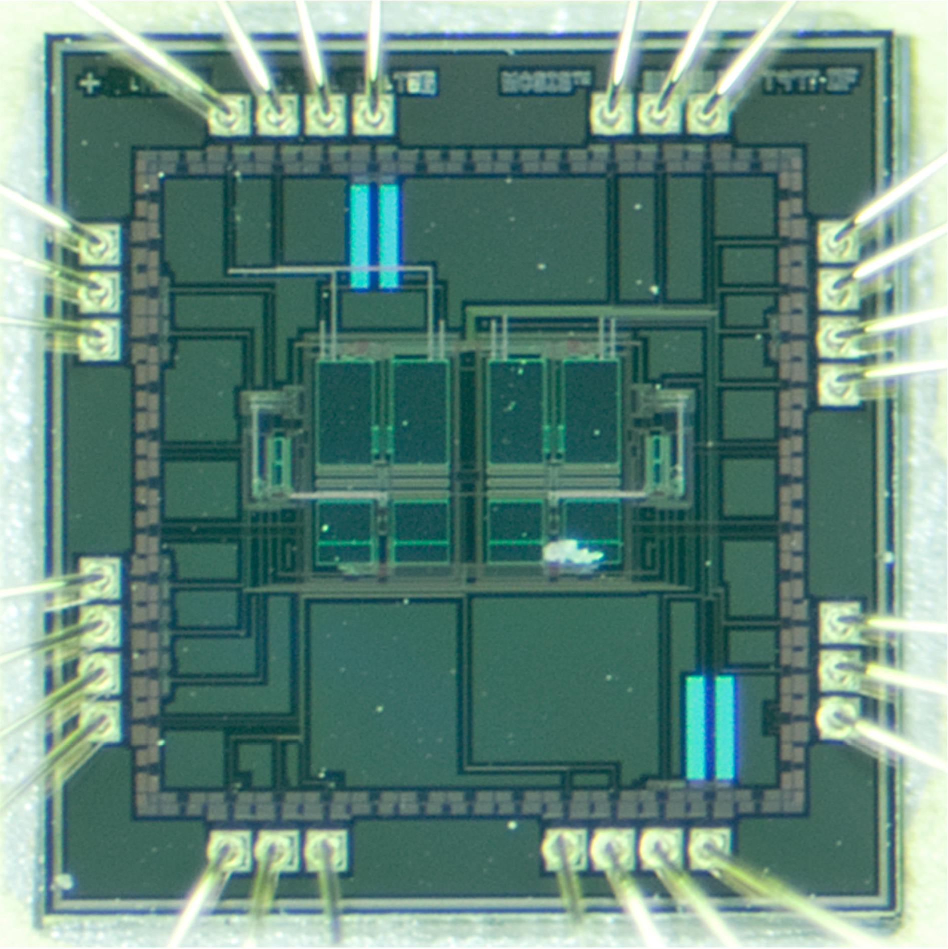

Figure 6.11: Micrograph of the fabricated 1.5mm × 1.5mm chip containing two channels.

Chapter 7

EOG Eye Tracking

7.1 Introduction

The complexity of modern health care introduces many confounding elements that may be associated with medical error and health care acquired harm [89, 90]. Although todayŠs clinicians have a multitude of electronic devices designed to promote safe medication practices, little has been done to determine which visual stimuli distract clinicians during performance, or to design effective visual cues to reduce error. Indeed, it is the multiplicity of equipment itself that can lead to delay or distraction when attempting to provide care [91, 92]. A key obstacle to determining the object of attention, or inattention, is the lack of tracking devices able to compute visual attention in space and time.

Here we report on the development of a unique human-machine interface that both records and responds to physiological and behavioral measures of subjects or patients immersed in virtual reality simulations of health care scenarios. The system is embedded in the StarCAVE, a fully immersive 3-D visualization VR environment in the California Institute of Telecommunications and Information Technology (CalIT^2) [93]. CAVE-CAD, computer aided design software developed by our interdisciplinary team for use within the StarCAVE, maps user responses in 4-D (3-D space plus time). A real-time 'bio-cursor' uses electrooculography (EOG) synchronized with VR head tracking to reveal attention to specific elements in the virtual environment. The bio-cursor is programmed to detect visual attention, and is further capable of detecting muscle and neural responses

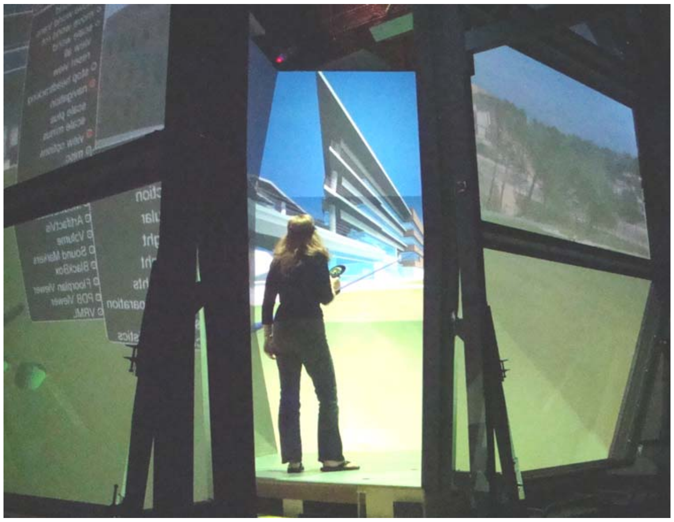

Figure 7.1: CalIT2 StarCAVE immersive visualization virtual reality environment [94] for controlled human experiments in interactive health care and architecture [93].

from electromyogenic (EMG) and electroenphalographic (EEG) biopotentials. The system provides real-time feedback of each eyeŠs location, providing a means to indicate the object of focus within models projected in the StarCAVE. The bio-cursor's ocular coordinate signals can be harnessed to enable hands-free control of the VR display, react to simulations, and to drive the interactive CAVE-CAD modeling software that allows clinicians and architects to assay the function of health care environments during the design process. Ultimately, we envision that the wireless bio-tracker will be used to assay visual attention during real clinical procedures, in real health care environments.

7.2 Immersive 3-D Visualization and Virtual Health Care

7.2.1 StarCAVE

The StarCAVE at CalIT^2, a five-sided virtual reality room with stereo projections on 360-degree screens surrounding the viewer [94], provides a central resource to this project and serves as an immersive visualization virtual environment for controlled experiments in interactive health care [93]. The StarCAVE offers 3-D stereo, 20/40 vision in a fully horizontally enclosed space with a diameter of 3 m and height of 3.5 m. A combined resolution of over 68 million pixels–34 million per eye, distributed over 15 rear-projected walls and two floor screens. Each of the five sides of the room has three stacked screen tiles, with the bottom and top screens titled inward by 15 degrees to increase the immersive experience, while reducing stereo ghosting. Each screen tile is served by a polarized pair of projectors, powered by a high-end, quad-core PC running on Linux, with dual nVIDIA graphics processing units (GPUs) to generate highly complex stereo images, and with dual network cards to achieve gigabit Ethernet/10GigE networking.

The StarCAVE environment is fully immersive, and interacts with the subject through a 3-D joystick as well as a head tracking sensor system. The head tracking system installed on a hat worn by the subject registers the subject's location and orientation in space and projects 3-D visual fields accordingly. Both the joystick and the head tracking system use four infra-red cameras that detect infra-red reflective balls to map position and orientation. The actual 3-D position for the viewerŠs head as well as the joystick are calculated and logged over time so that the viewer position and interactions are dynamically tracked in the virtual setting.

7.2.2 CAVE-CAD

A major advantage of the StarCAVE VR environment for fully immersive virtual health care is the capability to dynamically alter the environment while logging subject responses in the design of controlled experiments. Our team has developed novel interactive computer-aided design software (CAVE-CAD) that enables experimenters to change the visual configuration of scenarios while they are immersed in the StarCAVE. This approach eliminates the traditional step of creating a 3-D model at a desktop computer, before bringing it into a virtual environment, thus allowing for much shorter turnaround times when changes to the model are to be made and immediately visualized in VR. The user is immersed in the CAD “drawing”, and has the ability to directly interact in 3D with the geometry, and immediately respond to changing geometries, materials and lighting. An example of a user navigating in virtual space in the StarCAVE emulating an architectural environment is depicted in Fig. 7.1.

The immersive and interactive capabilities of the StarCAVE VR environment are further augmented with simultaneous physiological and neurological monitoring of the subject responses to enable a new class of controlled experiments in virtual health care.

7.3 Physiological and Neurological Monitoring

We have developed and tested a customized non-contact biopotential sensing and logging device that can detect and collect electroencephalogram (EEG), electromyogram (EMG), electrooculogram (EOG), and electrocardiogram (ECG) signals from the body and transmit the digitized waveforms over a Bluetooth wireless link [95]. The unobtrusive sensor operates without conductive contact to the skin, and can be mounted over hair or over clothing without conductive gel or other skin preparation. Other versions of the sensor make use of dry-contact sensors as well as conductive fabric to integrate sensing into apparel worn by the user. These advances contribute to the mobility and simplicity of the subject experience during continuous brain and ocular activity monitoring in the StarCAVE VR environment. The EEG/EOG system directly interfaces with the StarCAVE computing platform through a Bluetooth communication link.

7.3.1 Wireless Integrated Biopotential Sensors

The recording system consists of a chain of active electrodes connected along a single common wire. While the system is designed to operate with non-contact electrodes for EEG and ECG use [12, 95] as shown in Fig. 7.2, it also operates with dry-contact or standard gel-based wet-contact electrodes, and for other signal modalities such as EOG and EMG. The sensors can be either in direct contact with the skin or embedded within fabric and clothing. A small base unit powers the entire system and contains a wireless transmitter to send data to a computer or other external device. Near the base unit, a single adhesive or dry contact sensor placed anywhere convenient is used to establish the ground reference for the system.

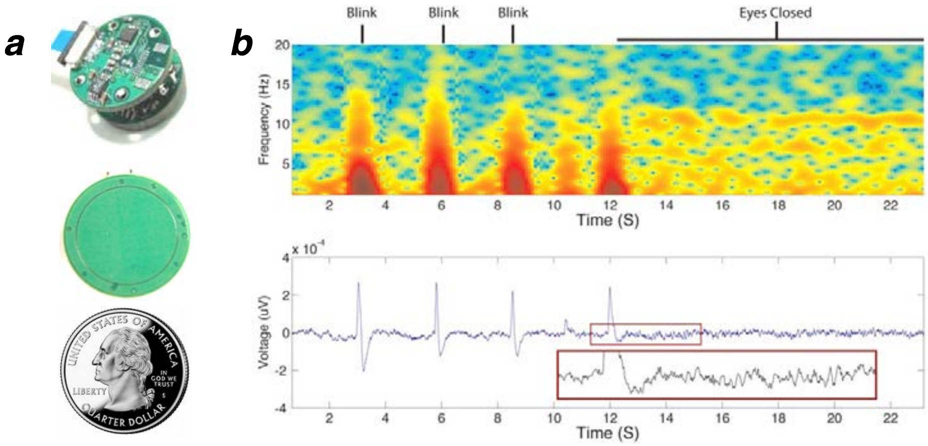

Figure 7.2: Non-contact EEG/ECG biopotential recording [95]. (a) Integrated biopotential acquisition, filtering and decimation unit operating at 600μW power. (b) EEG alpha wave and eye blink activity, recorded from the occipital lobe over haired skull.

Figure 7.3: Bio-cursor head-mask with six EOG electrodes.

7.3.2 Wireless EOG 3-D Eye Tracking Bio-Cursor

Although EOG signals have found widespread use as biomedical sensors mostly for monitoring of REM activity during sleep, only recently EOG has revealed a consistent measure of eye gaze direction for tracking visual attention in human-computer interfaces [96]. Here we report the first use of EOG for tracking of visual attention in 3-D, as a ‘bio-cursor’ user interface embedded in the StarCAVE VR environment.

We have adapted the wireless integrated biopotential array for EOG use in the prototype 3-D eye tracking bio-cursor. The system uses DC-coupled gel-based wet-contact active electrodes rather than intrinsically AC-coupled capacitive non-contact sensors [12, 95] to capture low-frequency components in the EOG signal that are required for continuous eye tracking.

The EOG head-mask is depicted in Figure 7.3. Six electrodes are positioned on the facial skin symmetrically around both eyes, to record both horizontal and vertical differential components in the EOG signal. These EOG signals relay the dipole moments of both eyeballs and are sufficient to register azimuth, elevation, and vergence of visual attention through calibration as outlined in Section 7.4.

Software embedded in the CAVE-CAD environment simultaneously logs stimulus, head position and EOG/EEG analog data converted at a rate of 400 samples/s to 2 byte-digits, sent via Bluetooth to a Linux system. The system is designed to record and log the EOG/EEG signals synchronously with the userŠs position and interactions in the virtual world, cueing analysis based on physiological/neurological events of interest and virtual stimuli of interest.

A calibration procedure to quantify and optimize the capacity of the EOG system to identify visual attention in the 3-D VR field of view is presented next.

7.4 Calibration of 3-D Ocular Movements

The EOG bio-cursor serves to dynamically track in 3-D the visual attention of the subject interacting with the VR health care environment. It is therefore critical to the performance of the system to calibrate the mapping from EOG signals to a reliable and reproducible estimate of 3-D ocular focus in the VR field of view. Since currently existing eye tracking systems are limited to 2-D for use with standard flat displays, we developed a novel calibration method to perform the mapping.

The calibration procedure correlates eye position with EOG within the 3-D field of view, linked to the viewerŠs head location, in the StarCAVE. A dynamic calibration stimulus is presented in the form of a yellow ball moving through virtual 3-D space. The position of the ball is modulated by three independent periodic wave functions, which each independently scan the space uniformly in the azimuth, elevation, and vergence dimensions. This modulation of the ball position in 3-D virtual space relative to the

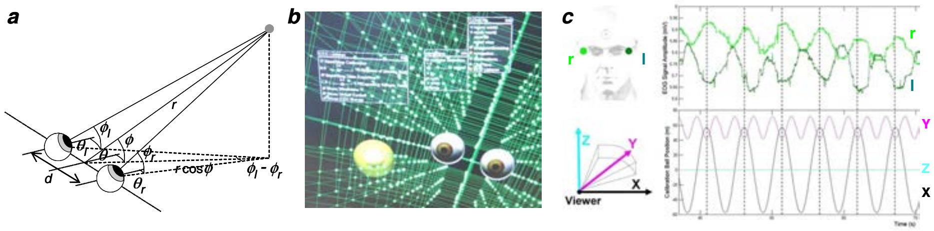

Figure 7.4: 3-D Eye tracking ‘bio-cursor’. (a) Ocular angular deflection geometry. (b) Graphical user interface for calibration visual stimulus. The virtual eyes are aligned with the subjectŠs eyes during the calibration procedure. (c) Segment of recorded EOG data, and corresponding calibration visual stimulus, for horizontal ocular angular deflection.

head coordinates of the subject guarantees a uniform spread in coverage of the angular deflections of the eye ball tracking stimulus across the field of view.

7.4.1 EOG Model of Ocular Angular Deflection

Differentials between horizontally positioned EOG electrodes measure horizontal ocular deflection (azimuth), and differentials between vertically positioned EOG electrodes measure vertical ocular deflection (elevation) [96]. Furthermore, a simple geometric model accounting for the EOG signals in response to 3-D visual focus in stereo vision shows that vergence in stereo vision can be obtained by differencing the azimuth estimates of both eyes. The geometry of the model is illustrated in Figure 7.4 (a), and yields approximate expressions for the spherical coordinates (r, θ, ϕ) of the visual target (focus of visual attention) in terms of the azimuthal and elevation angular deflections (θ_l, ϕ_l) and (θ_r, ϕ_r) of the left and right eyeballs, in the limit where the distance r (or ‘vergence’ between the target and the center of the eyes is significantly larger than the distance d between the eyes:

$$\begin{aligned}
\theta &\approx \frac{\theta_l + \theta_r}{2} \\
\phi &\approx \frac{\phi_l + \phi_r}{2} \\
r &\approx \frac{d \cos\theta}{\cos\phi \, (\theta_l - \theta_r)}
\end{aligned} \tag{7.1}$$

These expressions show that while the azimuth θ and elevation ϕ of the visual focus directly correspond to the average azimuth and elevation of the ocular angular deflections, the vergence is inversely proportional to the difference between the two ocular azimuth angles $\theta_l - \theta_r$. The challenge in accurately estimating vergence is to resolve small azimuth differences in already small differential EOG signals.

For small angular deflections θ and ϕ, the EOG electrode voltages V_i $(i = 1, \ldots 6)$ are approximately linear in θ and ϕ, and furthermore $\cos(\theta) \approx 1$ and $\cos(\phi) \approx 1$ in (7.1) so that an approximate linear relationship can be assumed between the vergence coordinates and EOG electrode voltages:

$$\begin{pmatrix} \theta \\ \phi \\ \frac{d}{r} \end{pmatrix} = W \begin{pmatrix} V_1 \\ \vdots \\ V_6 \end{pmatrix} \tag{7.2}$$

where W is a matrix of parameters that depend on the geometry of EOG sensor placements relative to the ocular frame of reference, and where constant DC offsets have been subtracted out. Note the choice of the inverse vergence parameter d/r for linearity and for a dimensionless representation. The linear relationship (7.2) is the basis of the calibration procedure.

7.4.2 Calibration Stimulus

Rather than computing W from the geometry, we calibrate the parameters in W from measurements by regressing the model (7.2) under a known calibration visual stimulus. For effective calibration under noisy EOG measurement conditions, it is important to choose a calibration visual stimulus that most uniformly excites the dynamic range of the variables under regression. We chose a triple-harmonic stimulus

$$\begin{aligned} \theta &= A_1 \cos(\omega_1 t) \\ \phi &= A_2 \cos(\omega_2 t) \\ \frac{d}{r} &= A_3 \cos(\omega_3 t) \end{aligned} \tag{7.3}$$

with angular frequencies ω_1, ω_2 and ω_3 randomly in the [0.8 Hz, 1.2 Hz] interval, and suitably small amplitudes A_1, A_2 and A_3. The length of the calibration interval is chosen much larger than $1/\min_{i \neq j} |\omega_i - \omega_j|$, and is 15 minutes in this pilot study.

7.5 Results

The above calibration procedure was performed off-line on time-stamped EOG data recorded simultaneously with the sequence of the dynamic calibration stimulus presented to the subject in StarCAVE. A screenshot of the graphical user interface for EOG data collection, integrated in the CAVE-CAD software environment, is shown in 7.4 (b). The grid (green dots) super-imposed on the calibration stimulus (yellow ball) serves as a reference for head fixation throughout the data collection. Eye blinks and involuntary saccades during the recording, as well as sources of impulse noise in the EOG measurement, are detected as abrupt changes in the EOG signals, and masked as invalid data during the calibration. The linear regression for calibration is performed on and averaged over continuous segments of valid data. The data analyzed here covers 15 minutes of continuous EOG data collected from a single session on a male subject.

A representable fragment of collected EOG data, along with the corresponding 3-D coordinates of the calibration stimulus ball, is shown in Figure 7.4 (c). The horizontal differential EOG signal, indicative of horizontal (azimuth) eye movement, clearly responds to the horizontal component of ball movement. Vertical deflections are also likewise registered by the vertical differential EOG components. The vergence component is present in the signal, however is subject to noise present in the EOG recordings due to the sensitivity in registering the difference between left and right eye azimuth components in the EOG signals.

Future extensions of the EOG bio-cursor technology will perform calibration continuously in the background to dynamically correct for drift and low-frequency noise in the EOG signal. Such dynamic corrections are possible since the subject may provide feedback on cursor drift through directed saccades.

7.6 Discussion

We presented and reported first results on a system for physiological/neurological monitoring and ocular tracking of a subject freely interacting in a 3-D virtual health care environment. The technology enables, for the first time, tracking of 3-D visual attention in a fully immersive VR environment.

We envision multiple applications and opportunities in e-Health and remote care. The wireless monitoring systems developed in the controlled laboratory of the StarCAVE may be applied to test healthcare outcomes in emulated medical environments, to yield answers to clinical questions such as where a surgeon looks for information in the midst of an operation, what attracts the attention of care-givers attending in urgent situations, or which conditions are correlated with a healing environment.

Chapter Seven is largely a reprint of material published in the 2010 IEEE Engineering in Medicine and Biology Conference: L. Zhang, Y.M. Chi, E. Edelstein, J. Schulze, K. Gramann, A. Velasquez, G. Cauwenberghs, and E. Macagno, "Wireless Physiological Monitoring and Ocular Tracking: 3D Calibration in a Fully-Immersive Virtual Health Care Environment," *IEEE Int. Engineering in Medicine and Biology Conference*, 2010. The author is one of the primary investigators of this work.

Chapter 8

Non-contact Brain-Computer Interfaces

8.1 Introduction

Brain Computer Interfaces (BCI) have been an area of intense study both as a means to rehabilitate injured patients and to simply augment the standard tactile, mechanical user interfaces ubiquitous today. Despite remarkable advancements in both neuroscience, signal processing algorithms and portable computing devices [97], the promise of a practical, user-friendly, non-invasive and mobile EEG-based BCI platform has remained elusive. Conventional BCI systems have always relied on laboratory bound instrumentation [98, 99, 100, 101, 102] and often require extensive subject preparation, including scalp abrasion, gels and a multitude of wired electrodes. Thus, the unassisted use of EEG-based BCI systems, outside the laboratory, is still a difficult proposition. For truly mobile BCI systems to become a reality, significant improvements in the sensor hardware are still needed.

In light of these limitations with the actual physical sensor interface, extensive research has focused on building dry electrodes [12, 77, 59, 103, 104, 105, 106] to enable unconstrained acquisition of EEG data. The number of dry electrode designs known in the literature is vast [59] and several commercial dry electrode systems have appeared on the market. Despite the multitude of options, however, detailed knowledge regarding the performance of dry electrodes for BCI is sparse. In particular, there exists no objective metrics and only a few studies exist directly comparing dry versus wet electrodes [103, 107, 108].

With aim to advance the understanding and use of dry and non-contact electrodes specifically for BCI, this paper focuses on quantifying the performance of three electrode types. The first is a simple active electrode built from standard off-the-shelf electronic components. Spring loaded fingers [25] provide for electrical connection to the scalp by pushing through the strands of hair. High contact impedances from the absence of gel and the small contact surface are mitigated with the use of an onboard buffer. The second design is a novel, high-impedance, non-contact electrode design based on a custom integrated analog front-end. Non-contact electrodes have been explored for ECG use and more rarely, EEG as well [109, 77]. However, the signal quality requirements are far more stringent for EEG than ECG, and the prototype sensors built from standard off-the-shelf components have been, to date, limited by noise and usability issues [59]. In contrast, our recent work has demonstrated a fully custom sensor front-end that is able to bypass many of the input impedance, noise and biasing issues encountered thus far. Detailed characterization of the this new integrated sensor can be found in the literature [71].

A mobile, wireless SSVEP BCI framework [97] serves as the basis for our experiments in this study. Visual evoked potential measurements serve as a convenient measure of different electrodes since SSVEP signals are well-defined and repeatable. Data taken with the three types of electrodes (wet, dry and non-contact) show the potential for dry electrodes to be fully usable for wireless BCI applications. While the signal quality from the integrated non-contact electrode still shows degradation as compared to its wet and dry counterparts, the experiments in this paper further suggest the possibility of realizing a mobile, non-contact through hair BCI system

8.2 Wireless Dry/Non-contact EEG System Design

8.2.1 Discrete Dry Sensor

The dry sensor consists of two sections. A lower plate contains a set of spring-loaded pin contacts which can easily penetrate hair without the need for any preparation.

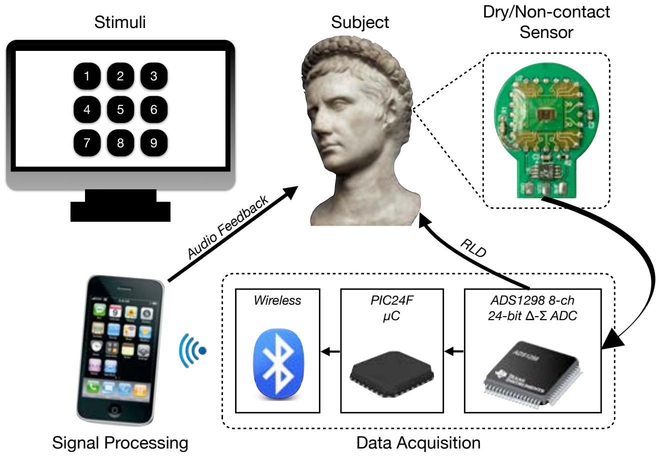

Figure 8.1: Wireless dry/non-contact BCI system concept. The BCI interface consists of a computer based visual stimulus program. SSVEP/EEG signals are acquired using dry/non-contact electrodes embedded within a headband over the hair in the occipital region. A high-resolution data acquisition system relays EEG telemetry to a cellular phone which decodes the SSVEP signals.

The gold plated "fingers" achieve direct electrical connection to the scalp. A male snap connector (identical to the one used for ECG electrodes) on the top side of the plate mates with it's female counterpart on a second PCB which contains the active electrode circuitry.

Relatively high impedance signals offered by the dry contact are buffered with an off-the-shelf CMOS-input opamp (National Semiconductor LMP7702). The unity gain amplifier, along with the shielded cabling, greatly reduces the effects of external interference.

As will be shown, the signal quality from this very simple dry electrode is excellent, and does not require any preparation. Compared to the wet electrode, a significantly greater amount of low-frequency drift was present, likely due the high contact impedance and the less stable electrochemical interface of the Au pins versus the normal Ag/AgCl electrode. Nevertheless, these effects were easily removed and far below SSVEP frequencies of interest. No discomfort was observed during usage. It is worthwhile to note, however, that the fingers may present an injury hazard in cases

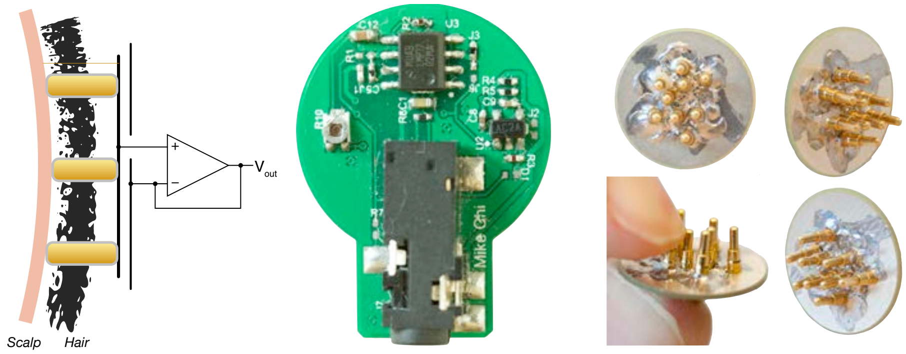

Dry Electrode Concept Active Electrode Circuitry Spring-loaded Dry Contact Pins

Figure 8.2: The implemented dry contact electrode used in the experiments. Spring-loaded pins push through the subject's hair and make contact with the scalp. The plate embedding the pins snaps into a buffer circuitry which provides a low-impedance output to the data acquisition box.

of direct head trauma, inspiring the development of the non-contact sensors described below.

8.2.2 Integrated Non-contact Sensor

As previously mentioned, non-contact electrodes which operate primarily via capacitive coupling have been studied for various applications, including EEG. Although dry scalp based electrodes are still relatively easy to handle with active electrode technology, the extremely high contact impedance ($>10\,\mathrm{G\Omega}||30\,\mathrm{pF}$), in the same order of magnitude as even the best CMOS-input amplifiers, of through-hair coupling has been a significant challenge in acquiring acceptable EEG signals. The attenuation due to source-input impedance division significantly degrades the CMRR of the front-end amplifiers. In addition, the high impedance interface can also, in many cases, generate significant amounts of intrinsic noise and is susceptible to various movement artifacts and microphonics [59].

The new integrated sensor achieves it's high input impedance through careful design and control of the sensitive input node, made possible by the custom VLSI circuit implementation. Previous attempts at building non-contact sensors have always relied on

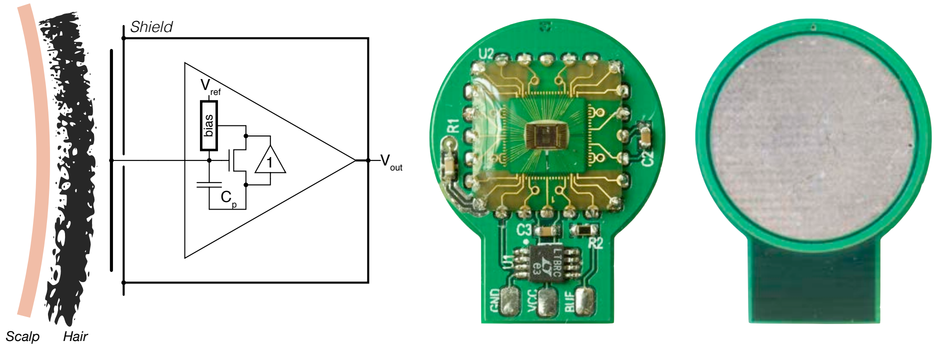

Integrated Non-contact Electrode Concept

Custom IC Sensor Package

Bottom Sensing Plate

Figure 8.3: Diagram and picture of the integrated non-contact electrode [71], which operates on top of hair. The integrated electrode achieves input impedances much greater than what has been possible with discrete designs through careful shielding and custom packaging made possible with an fully custom IC design.

active shielding to minimize noise and interference, but the shield's effectiveness was necessarily constrained to just the PCB-level due to the lack of access to the internal nodes of the off-the-shelf amplifiers used in the front-end. Any parasitic capacitances internal to the amplifier (≈2-20 pF) still had to be eliminated via manually tuned neutralization networks. Not only is this calibration process imperfect, it also precludes the mass production of these sensors. In contrast, we were able to fully bootstrap and shield the input node, starting from the active transistor, extending out to the bondpads and out to a specially constructed chip package. The ability to fully shield the input node eliminates the need for carefully tuned input capacitance neutralization, as with other designs [109], and achieves an input capacitance of just 60 fF. Moreover, the integrated approach made it possible to implement low-leakage, low-noise (0.5 $\mathrm{fA/Hz^{1/2}}$) bias structures that simultaneously enable fast input overload recovery and stable low frequency response (<0.05 Hz).

Testing of the integrated non-contact sensor demonstrated significant performance improvements compared to conventional non-contact electrodes built with discrete components [59, 27, 109]. Direct comparison against older non-contact sensors, even with careful neutralization, showed that the new integrated sensor achieved a much closer signal correlation ($r = 0.953$ versus $r = 0.918$ and $r = 0.715$) to the signals obtained with clinical wet Ag/AgCl electrodes [71]. Although the signal quality of this integrated non-contact sensor is still noisier and less robust than the dry and wet contact electrodes, we will demonstrate that this new integrated non-contact sensor can acquire SSVEP signals at much finer gradations than was possible before [77].

8.2.3 Reference Wet Electrode

A set of standard passive hydrogel ECG electrodes were used as a control in the experiments. The adhesive sections of the electrodes were removed, leaving only the hydrogel which was placed on top of the subject's hair. Additional conductive gel was dispensed to ensure a good electrical connection to the scalp. No special preparation of the skin, such as abrasion, was required. The low-impedance of the wet electrode, even without any active buffering circuitry, exhibited the best signal quality in terms of noise and drift.

8.2.4 Wireless Data Acquisition

Each of the sensors are connected directly to an octal, simultaneous sampling 24-bit $\Delta\Sigma$ ADCs (TI ADS1298). The ADC is controlled by a PIC24F low-power microcontroller which acquires samples and dispatches the data to an onboard Bluetooth module (Fig. 8.1). The portable data acquisition box is powered by two AAA batteries, good for approximately 10 hours of continuous wireless telemetry.

8.2.5 Mobile Signal Processing

Signal processing of the EEG telemetry was accomplished on a Nokia N97 cellular phone. A sample plot of alpha wave activity, displayed on the phone's 640×360 pixel 3.5 in touchscreen LCD, from 3 non-contact electrodes is shown in Figure 8.4. The BCI application was written in J2ME (Java 2 Micro Edition) using JBuilder 2005.

The phone establishes a Bluetooth serial port connection with the data acquisition box and initially presents the user with raw telemetry. After the EEG signal quality has been verified by the user, the application can switch to canonical correlation analysis

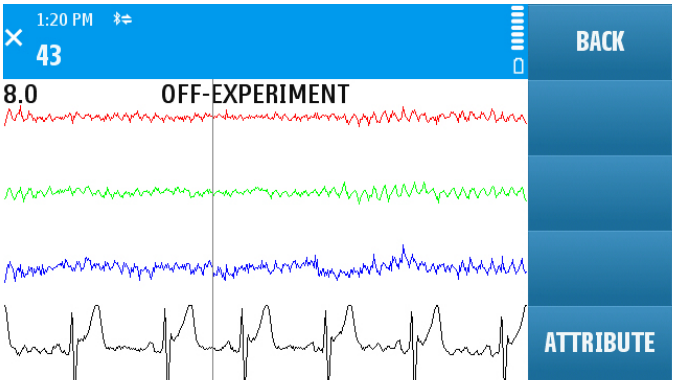

Figure 8.4: Sample data (0-50 Hz BW) from three non-contact electrodes, over hair, transmitted for display on a cellular phone. A reference ECG signal, taken with a standard wet electrode on the chest, is also displayed. Data processing occurs in real-time on the mobile device.

(CCA) mode for actual BCI experimentation. In the analysis mode, a band-pass filter is applied to the signal to remove frequencies that are outside the SSVEP band (9-12 Hz).

The CCA analysis algorithm [97] attempts to obtain the maximum correlation between the signal from the three recording electrodes with a matrix of sine/cosine templates that correspond to the 12 possible stimulus frequencies. For the experiments involving wet and dry electrodes, decisions are made on a four second sliding window that advances in one second increments. Two consecutive decisions are construed as a successful input and trigger an audio feedback to notify the subject. To allow for the subject time for rest and blinks, a one second blackout is enforced after each input. During the tests, it was found that the 4 s window, 2 consecutive decisions was not reliable for the non-contact electrodes due to degraded SNR. Increasing the window to 6 s with four consecutive decisions allowed for sufficient rejection of the extra noise.

8.3 Comparative SSVEP Sensor Benchmark

To first validate the signal being acquired by the dry and non-contact sensors compared to the standard wet Ag/AgCl electrode, a comparative experiment was devised and performed on ten different subjects. The experiment consisted of having each subject

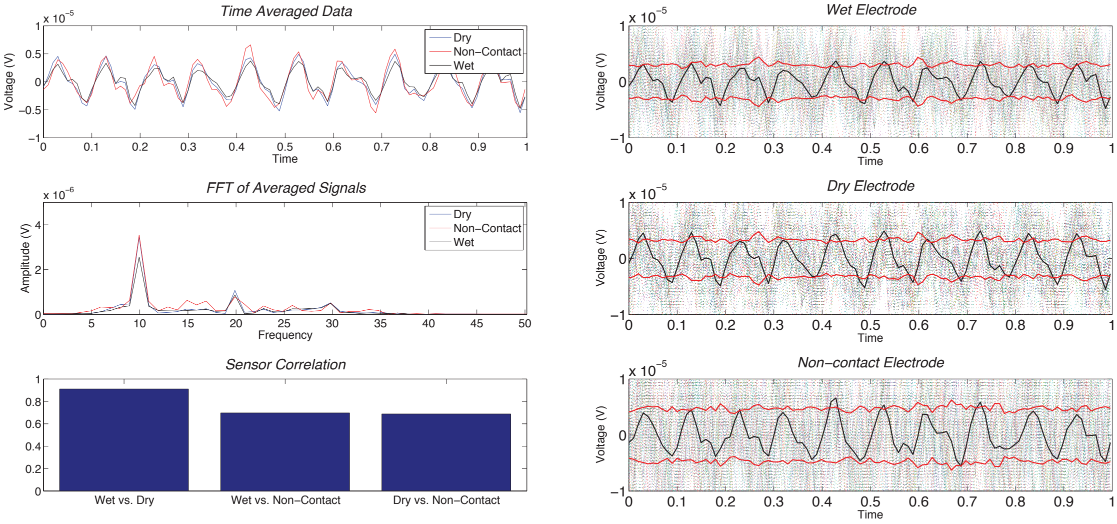

Figure 8.5: (Left) Sample time averaged SSVEP signals from the wet, dry and non-contact electrodes for one subject during a 6 s trial along with the FFT and correlation. Averaging was performed over a 1 s period using a 0.5 s sliding window. (Right) Detailed signals from each electrodes with the average in black, the standard deviation in red along with the raw signals.

gaze at a single SSVEP target stimulus, displayed on a CRT monitor, at 10 Hz for a one minute duration. During the experiment, the SSVEP signal was decoded, in real-time, to verify the presence of the 10 Hz stimulus signal, but no feedback was presented to the subject. Each subject repeated this task three times, and the best dataset was used for analysis. None of the subjects had shaved heads and in all cases, the non-contact sensor was on top of several layers of hair.

Directly benchmarking several EEG sensors on a live subject can be problematic. Unlike ECG where there exists large areas at an equipotential (eg. limbs), closely spaced EEG electrodes can observe different signals. In this experiment the three sensors (wet, dry and non-contact), were arrayed in a triad over the occipital region as closely together as possible. The relative placement of the electrodes was consistent between different subjects. Care was taken to prevent gel from the wet electrode seep into the neighboring dry and non-contact electrodes. A sample plot of the raw and time averaged SSVEP signal for one subject is shown in Figure 8.5.

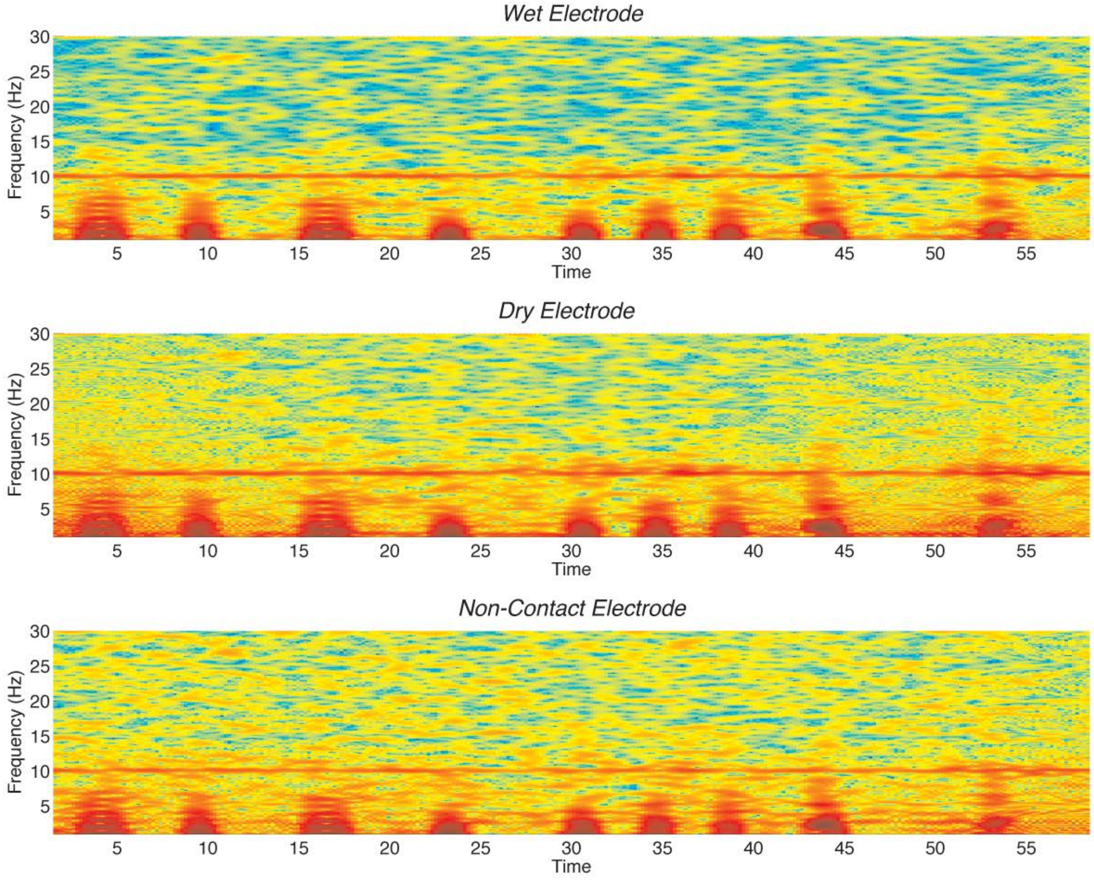

Figure 8.6: Spectrogram of one 60 s trial for subject two. The 10 Hz SSVEP stimulus tone is visible in the spectra of the signals from every electrode. Blink artifacts are also visible.

8.3.1 Comparative Benchmark Results

The PSD of the signal from each sensor during the 60 s second trial of four of the subjects is shown in Figure 8.7. In all cases, the 10 Hz stimulus is clearly visible, although the amplitude of the SSVEP and amount of the background 'noise' varies considerably between subjects. From first glance, the PSD from the wet electrode almost perfectly matches that from the dry electrode, consistent from our observations that aside from larger amounts of drift, the signal quality from the dry electrode was excellent. The PSD of the non-contact electrode's signal also clearly shows the 10 Hz stimulus, verifying that it is indeed capable of acquiring EEG signals through hair. Unlike the dry electrode, the non-contact sensor can exhibit a greater amount of both low-frequency drift as well as broad-band noise due to the extremely high coupling impedance and sensitivity to movement artifacts. In one subject (Fig. 8.7 bottom left) a pulse artifact can be seen in the spectra due to poor coupling of the non-contact electrode.

For quantitative analysis of of the signal quality from the various electrode types, a few key parameters are desired. First, it is useful to obtain a metric that conveys how close the signal from dry and non-contact electrodes matches the signal from a 'gold standard' wet electrode. Secondly, it is also useful to know the ratio, or SNR, provided by each electrode showing the amount of useful signal, in this case SSVEP, versus the background noise.

Table 8.1: Measured SSVEP Amplitude, Sensor Correlation and SNR for Wet, Dry and Non-contact Electrodes

Subject	SSVEP Amplitude (μV)			Sensor Correlation			SNR (dB)		
	Wet	Dry	NC	Wet vs. Dry	Wet vs. NC	Dry vs. NC	Wet	Dry	NC
1	1.1	1.7	2.2	0.882	0.846	0.739	-15.2	-11.0	-10.4
2	3.7	3.7	3.2	0.978	0.875	0.852	-6.5	-7.0	-8.5
3	1.9	2.0	2.1	0.898	0.780	0.702	-11.7	-12.2	-13.0
4	2.2	2.2	2.4	0.967	0.795	0.782	-7.7	-8.1	-8.2
5	1.1	1.1	1.0	0.975	0.957	0.937	-12.2	-11.9	-13.0
6	1.6	1.2	1.4	0.747	0.712	0.551	-6.6	-10.5	-9.7
7	1.6	1.1	1.8	0.905	0.860	0.880	-14.3	-13.6	-10.7
8	2.5	3.4	3.5	0.931	0.727	0.700	-6.8	-5.2	-7.5
9	1.4	0.8	0.8	0.887	0.851	0.850	-13.1	-17.4	-17.6
10	1.4	1.8	1.4	0.949	0.571	0.594	-15.6	-13.3	-18.2

Specifically for this experiment, the three sensor was first band-pass filtered around 8-13 Hz to remove all frequencies not relevant to the SSVEP stimulus. Since the SSVEP signal is small, this removes the majority of noise in the signal and enables a correlation comparison between the three sensors specifically for the SSVEP. To account for phase shifts of the SSVEP signal due to differences in electrode placement, the cross correlation (MATLAB *xcorr*) was used, and the maximum value was extracted for three comparsions: wet vs. dry, wet vs. non-contact and dry vs. non-contact. A summary of the computed correlations can be found in Table 8.1.

For the dry electrode, over half the subjects had a correlation of greater than 0.9 between the wet and dry electrodes, with three subjects achieving almost perfect

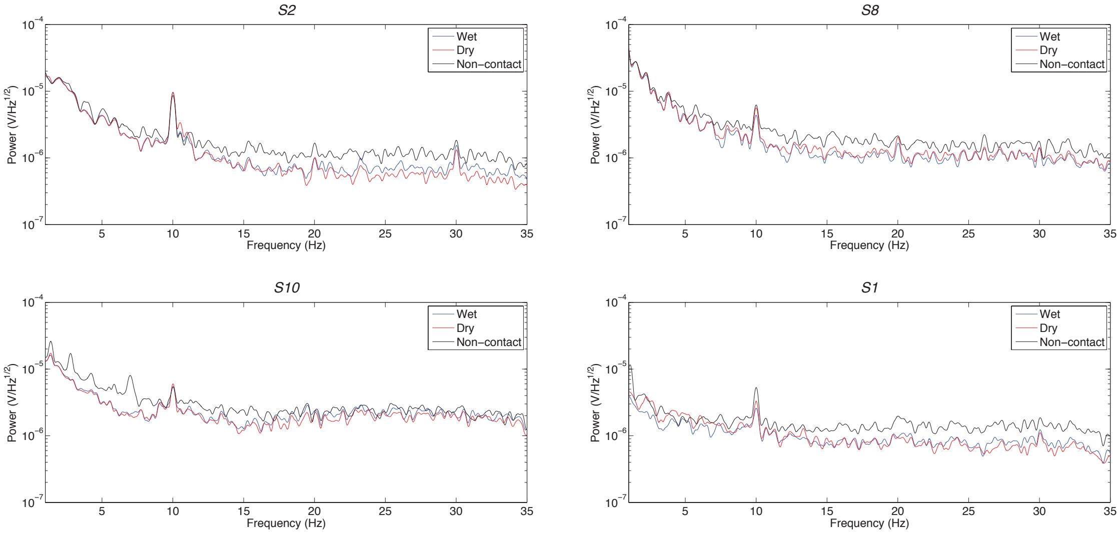

Figure 8.7: Power spectral density of the simultaneously acquired EEG signal with the wet, dry and non-contact electrodes as the subject was asked to gaze at the 10Hz stimulus target. The PSD was computed over a continuous 60 second period.

correlation (0.978, 0.967, 0.975). Only one subject exhibited a wet vs. dry electrode correlation of less than 0.8. Correlation values of the wet versus non-contact electrode were lower, which was not surprising. Nevertheless, half the subjects had correlation values of above 0.8. Only one subject had a correlation value of less than 0.7.

Previous studies [107, 103] of dry electrodes typically found correlation values of approximately 0.8 between neighboring wet and dry electrodes. It is important to note, however, that the experiments in this paper are narrow band in nature (8-13 Hz), whereas previous studies were focused on more general EEG experiments with larger signal bandwidths. This discrepancy in bandwidth makes an direct, objective comparison difficult. As an example, decreasing the high pass corner from 8 Hz to 0.5 Hz, would introduce drift noise, which typically has a large amplitude, into the correlation comparison. If the two electrodes were drifting independently, then then the correlation value would decrease towards zero. On the other hand, if the common reference electrode was in poor contact and noisy, causing the two recording electrodes to drift synchronously, then the correlation value will increase towards one. Either process would likely dominate the low amplitude SSVEP signal. Thus for the experiments in this study, which focuses on the SSVEP paradigm, a narrowband approach that preserves only the signals of interest is justified.

The second metric, SNR, was computed by examining the root-mean square amplitude of the fundamental 10 Hz tone, obtained via an FFT on the time averaged data ($\bar{X}$), versus the background noise within the 8-13 Hz SSVEP band,

$$\mathrm{SNR} = 10\log_{10}\frac{\bar{X}(10\,\mathrm{Hz})^2_{rms}}{var(x) - \bar{X}(10\,\mathrm{Hz})^2_{rms}}. \tag{8.1}$$

The background noise was approximated by subtracting out the contribution from the SSVEP tone from the standard deviation of the 8-13 Hz band-passed EEG (x) signal during the 60 s trial. This allows for a direct comparison of the signal strength versus noise for each electrode. This number, provided in Table 8.1, represents the instantaneous SNR and is always well below 0 dB due to the small amplitude of the SSVEP signal relative to the background EEG and noise. Reliable detection of the stimulus, however, is made possible by the processing gain from FFT or CCA analysis of the signal over a time window.

8.4 Real-time Decoding of Non-contact SSVEP Signals

Offline analysis of benchmark data shows that SSVEP signals can be reliably extracted from dry and even non-contact electrodes. To demonstrate their use in real-time BCI applications, subjects 1, 2 and 4 were recalled to perform a SSVEP phone dialing task using the mobile signal processing platform as previously described. Additional details regarding this SSVEP paradigm can be found in a previous publication [97] .

The online task consisted of entering a predetermined 12-digit sequence. The time to complete the task along with the error rate was recorded and used to calculate the ITR. Signal decoding was performed using CCA analysis on data streamed across the wireless link. A full suite of tests was conducted on subjects 1 and 2 which consisted of using all three of the electrode types in multiple separate trials. Data from the tests is shown in Table 8.2.

Both subjects were able to achieve control of the BCI system using any electrode type. As expected, the wet and dry electrodes were could both be successfully used

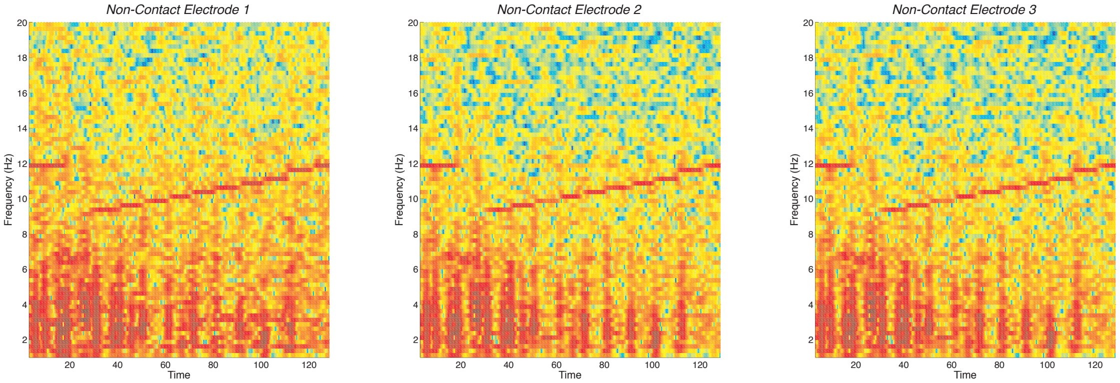

Figure 8.8: Spectrogram of data taken during a real-time SSVEP decoding task using non-contact electrodes. The SSVEP sweep across different frequencies is clearly visible in all of the channels. Data is taken over a 6 s sliding window.

for BCI, although with a minor error rate, typically 1 or 2 errors out of 12. Although the ITR rates in this experiment do not quite match the best of previous reports in the literature, it does provide for a baseline in this comparative study. It is possible that higher ITR rates could be achieved if more electrodes were available - in the current experiment, only three electrodes are used at a time. It is interesting to note that the dry electrode trials actually achieved superior performance to the wet electrode trials. This is likely attributed to the fact that the wet electrode was always tested last (to avoid gel contamination on the dry and non-contact sensors). Subject fatigue and variability may have a significant performance impact over time. Nevertheless, this establishes the feasibility of dry electrodes for SSVEP BCI use.

With the non contact electrodes, one of the subjects (1) was able to consistently achieve 100%. Although a longer detection window was required to compensate for the increased noise with non-contact electrodes, we were able to achieve an ITR rate of over 20 bits/min. To our knowledge, this level of performance with non-contact electrodes has never been demonstrated before. The only previous study of true non-contact, capacitive BCI achieved an ITR of 12.5 bits/min [77], which required both a training session and the use of significantly less selection choices (3 vs. the 12 in our study). Even though additional study is clearly warranted, this is strong indicator that not only do the new integrated non-contact electrodes do indeed acquire useful EEG, the signal quality is of sufficient quality for BCI.

Table 8.2: Online BCI Test Results

		Accuracy			Time/Selection (s)			ITR (bits/min)		
		Wet	Dry	NC	Wet	Dry	NC	Wet	Dry	NC
Subject 1	Trial 1	0.83	0.92	1.00	6.2	5.7	10.3	23.0	28.1	19.3
	Trial 2	0.83	0.83	1.00	5.9	5.8	9.7	23.9	22.6	20.5
	Trial 3	0.83	1.00	1.00	6.4	5.6	9.4	20.5	34.4	21.0
Subject 2	Trial 1	0.83	0.83	0.50	6.2	5.9	12.8	23.0	23.9	4.0
	Trial 2	0.83	0.92	0.75	5.9	6.3	9.7	23.9	27.3	11.9
	Trial 3	0.92	0.83	0.75	5.7	6.3	11.0	29.2	22.6	10.4
	Mean	**0.85**	**0.89**	**0.83**	**6.0**	**5.9**	**10.5**	**23.9**	**26.5**	**14.5**

Subject 2 had more difficulty with utilizing the non-contact electrodes, probably a result of thicker hair which increased the probably decreased the SNR and made the sensors more susceptible to motion artifacts. Movement induced errors were a challenge in subject 2's trial since the SSVEP paradigm requires a stable signal over a time window (4 to 6 s). Transient artifacts appear as a large 1/f disturbance in the frequency domain and can cause either decoding errors and/or excessively long decision times.

An interesting dichotomy was noted during the experiments. Whereas wet electrodes typically perform well shortly after application (allowing for a short time to stabilize the electrochemical interface), the dry and non-contact electrodes take much longer to achieve a stable trace. On the other hand, wet electrodes are susceptible to drying of the electrogel over time, but the signals from dry and non-contact electrodes do not degrade with time. This is likely due to sweat and other effects moisturizing the hair and skin under the electrode, achieving improved coupling. While this phenomenon with dry and non-contact electrodes is disadvantageous in time constrained laboratory applications, it is definitely useful for long-term, mobile use.

8.5 Discussion

As further improvements in both neuroscience and signal processing better enable BCI systems, there exists a need for sensor arrays that do not require time and labor intensive preparation to truly transition laboratory innovations into general practice..

With that goal in mind, dry and non-contact electrodes offer a potential solution that alleviate many of usability shortcomings inherent with wet Ag/AgCl electrodes.

Quantitative benchmarking show that dry and non-contact electrodes are fully capable of resolving SSVEP signals. In many cases, the dry electrode only shows a slight amount of signal degradation, except for increased drift, compared to the standard wet Ag/AgCl electrode. The non-contact electrode, through hair, shows somewhat more degradation, but the signal quality still remains useful. The online experiments in this study demonstrate that both electrodes are feasible for BCI applications.

In general, movement artifacts and electrode placement remain an unresolved challenge with both dry electrodes and especially non-contact electrodes. For the purposes of this study, we utilized a simple, tight, elastic band around the subject's head. The sensors were tucked underneath the band during experimentation. Achieving acceptable signals still required a degree of finesse and manual intervention. For future arrays that are more user-friendly, a more reliable and comfortable construction needs to be developed.

Towards that end, It is expected that improved signal processing algorithms for artifact rejection in conjunction with the electrode technologies presented here and further characterization will significantly advance the field of mobile BCI systems.

Chapter Eight is largely a reprint of material submitted to the IEEE Transactions on Neural Systems and Rehabilitation Engineering Journal. The author is the primary author and investigator of this work. Y. M. Chi, Y.T. Wang, Y. Wang, C. Maier, T.P. Jung and G. Cauwenberghs, "Dry and Non-contact EEG Sensors for Mobile Brain-Computer Interfaces," *IEEE Transactions on Neural Systems and Rehabilitation Engineering* (Submitted).

Chapter 9

Conclusion

Advancements in wireless communications and mobile technology have increased the importance of personalized healthcare. The process of transmitting and analyzing health data has become simple and inexpensive with even the most inexpensive devices of today. However, the sensing key physiological parameters, from heart rate, nutritional intake to physical activity, remains a challenge, limited by both technology and user behavioral compliance. For wireless health to reach it's full potential, improvements in unobtrusive sensor technology are still required..

This thesis has focused on addressing the sensory limitation primarily within a cardiac and neural framework. Physiological data from ECGs and EEGs potentially offer insight into a variety of coronary and neurological disorders, especially information can be aggregated over both long time periods and across large populations. Traditional outpatient cardiac monitors devices, however, are typically constrained to just a day or two for high-resolution acquisition and just two weeks for basic rhythm detection. Outpatient EEG monitoring, for applications such as sleep or epilepsy diagnosis, has yet to become practical due to the difficulty in applying and maintaing gel electrodes.

Non-contact biopotential sensing offers a superior user experience by dispensing with the traditional need for adhesives, gels and even skin-contact making it suitable for mobile, long-term home use. Previous efforts have demonstrated proof-of-concept non-contact sensors using discrete, off-the-shelf components for both ECG and EEG. However critical details on the construction and performance of non-contact sensors have remained generally proprietary and in the literature. As part of this work, we have developed and show the full schematics and design considerations for building high-quality, discrete-component non-contact sensors, contributing to knowledge that is publicly available.

Detailed characterization of the discrete component sensors, however, revealed that it could not reliably achieve the performance specifications for clinical applications. In addition, it was found that maintaining critical specifications, such as high-input impedance, required considerable manual tuning, precluding the manufacture of non-contact sensors at price points viable for consumer use.

To eliminate the need for manual tuning and resolve the input impedance difficulties with discrete components, a custom integrated solution was explored. By fully controlling the parasitics associated with the input node, made possible with the integrated design, input impedances far beyond what was previously possible were achieved. Benchmarking of the new sensor against clinical adhesive Ag/AgCl electrodes as well as the older discrete designs showed a considerable improvement in the accuracy in signal accuracy. Nevertheless, unresolved problems with noise and motion artifacts remain a difficulty. The signal from the non-contact sensor, while much more accurate than before, were still much more noisy despite the significant improvements in the noise specifications of the integrated sensor.

Previous attempts at modeling the noise sources in a non-contact sensor in the literature have always considered the insulation gap between body and sensor to be an ideal capacitor leading to the erroneous conclusion that decreasing the noise floor was simply a matter of better amplifier components. Closer examination of the all the noise contributors, in this work, showed that the non-contact interface between the body and input sensor was actually the largest contributor of noise. Although disappointing that much of the noise with non-contact sensors are intrinsic to the interface and irreducible, this revelation nevertheless is a important new piece of knowledge in this field.

The techniques and knowledge introduced represent the state-of-the-art in non-contact sensor design. High-resolution, near clinical-grade, ECG sensing, through clothing, have been demonstrated. Additional exemplary applications also include a EOG based eye tracking system as well as a non-contact, through-hair, brain-computer interface all as part of this thesis. With the electronic design considerations now well described and understood, it is expected that future improvements in this field will be within the mechanical construction and signal processing domain. Combining the circuit innovations in this research with new industrial design and artifact rejection algorithms will finally enable non-contact sensing as a practical tool for mobile health, fitness and brain-computer interfaces.

Appendix A

Focal-Plane Change Triggered Video Compression for Low-Power Vision Sensor Systems

A.1 Introduction

In addition to physiological sensing, image and video sensing is also an important component for healthcare and many other applications, especially within a mobile context. Conventional compression systems are limited by both the power dissipation required to operate the image sensor and DSP as well as the power required to transmit telemetry. In situations where mostly static scenes are encountered (e.g. safeguarding the elderly, security), the expenditure of energy for data transmission is kept at a minimum making the power required to operate the sensor and DSP the limiting factor on battery life. In the same philosophy as before, the possibilities of leveraging a custom integrated sensor front-end is utilized to construct a hybrid video compression system that bypasses many of the power consumption challenges typically encountered with off-the-shelf solutions.

Video compression is among the most computationally intensive tasks in current imaging technology [110] [111]. Advanced compression schemes like H.264 provide, simultaneously, high compression rates and low visual distortion. Implementation, however, is costly in both terms of power consumption and hardware complexity and is ill-suited for mobile applications. For situations requiring a low power, long term wireless vision sensor, an alternative approach is justified for two reasons. First in many sensor applications, like surveillance, scenes are predominantly static - necessitating a sensor platform that does not expend energy processing irrelevant data. Secondly, the tradeoffs between bandwidth, power and visual quality are different. The first two must be prioritized with the provision of maintaining an image sufficient to identify events and subjects of interest.

Although the use of differential coding and motion compensation minimizes the data output rate for periods in activity for conventional video encoders, the entire encoding chain including sensor, ADC and DSP must operate continuously [111]. For static, unchanging scenes, such systems inefficiently dissipate energy processing pixels that do not convey any new or meaningful information. Thus, for long term surveillance applications, it is the power usage by the sensor and DSP in monitoring the scene that will dominate the operating lifetime of the system. For a truly low power system, this energy waste must be minimized.

Our approach utilizes the possibilities afforded by focal-plane processing in CMOS image sensors. Many previous research efforts have successfully demonstrated the viability of implementing focal-plane spatial transforms [112, 113, 114, 115, 116] to facilitate highly power efficient image compression. Although such solutions are ideal for single snapshots, they do not account for the temporal redundancy in full motion visual information, and are not ideal for video rate applications. In this paper, we present compression architectures that employ focal-plane change detection as a temporal processor, rather than spatial, to selectively encoded video data to reduce the power consumption in scenarios where static scenes dominate.

Figure A.1 shows the circuits of a CMOS image sensor with focal-plane change detection [117]. The imager detects, in each pixel, changes in intensity exceeding a positive and negative threshold, and codes pixel locations of these change events, along with the intensity for any pixel on demand. This CMOS imager forms the basis for energy efficient video compression schemes in this paper that uses the gating of change events to save on the cost of data conversion and computation in the encoding of frame fragments that have insignificant change.

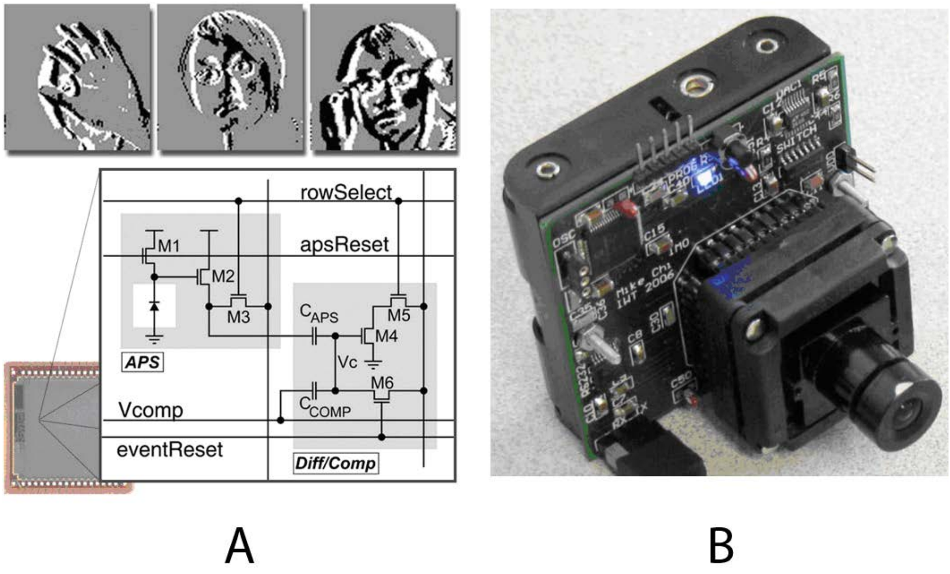

Figure A.1: (A) Motion-based imaging integrated surveillance system with CMOS image sensor that performs change detection at the pixel level. (B) Sample change detection output of the CMOS image sensor. The system operates on 4 AA batteries, and includes a 16-bit microcontroller for integrated video compression and power management.

A system integrating the CMOS image sensor [118, 119] with external supporting circuitry and microprocessor is shown in Figure A.1. The image sensor provides the temporal pixel intensity change trigger as well as analog video signals, which are digitized by an external ADC on demand. Image processing and compression operations are then undertaken by the microcontroller produce a compressed digital output for connection with a wireless communications system.

The basic operation and simple compression architecture was described in [117, 118, 119]. In this paper we expand on the compression architecture by adding an entropy encoder, along with differential encoding to further reduce the data rate. In addition, the architecture has been generalized and compared with other related change triggered encoding schemes. Finally, the distortion and power efficiency of the system is analyzed, and the performance characterized on benchmark surveillance video data.

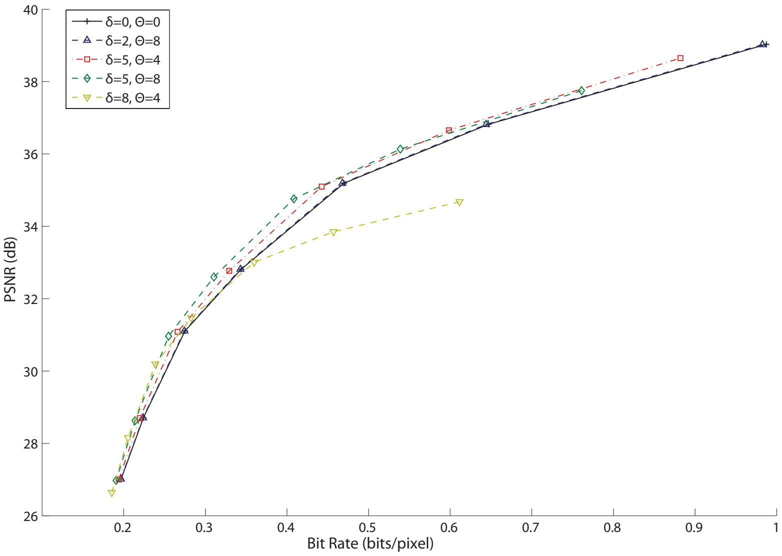

Figure A.2: Rate-Distortion curves by varying δ and Θ for the CT DCT DPCM encoder with Q ranging from 16, 24, 32, 48, 64, 96, 128. The $\delta = 0$ and $\Theta = 0$ case corresponds to the non change triggered baseline (DCT DPCM). The curve where $\delta = 5$ and $\Theta = 8$ offers the best trade-off in terms of the compression performance and introduced error.

A.2 Compression Architectures

The overall design goals for the compression architectures are targeted for operation on a power constrained platform with limited processing capabilities over a low bandwidth wireless network. Figure A.2 shows the block diagram for each of the encoders with the signal chain starting at the pixel and ending at the decoded image at the receiver with each of the operations.

A.2.1 Change-Triggered Pixel Refresh (CT Pixel Refresh

The simplest form of video compression involves sending only pixels that exceed a set intensity change threshold [120] from frame to frame after an initial keyframe (Fig. A.3). An analog threshold value, δ, sets the trigger point for the intensity change detection circuit. Pixels which have an intensity change greater than the magnitude of δ

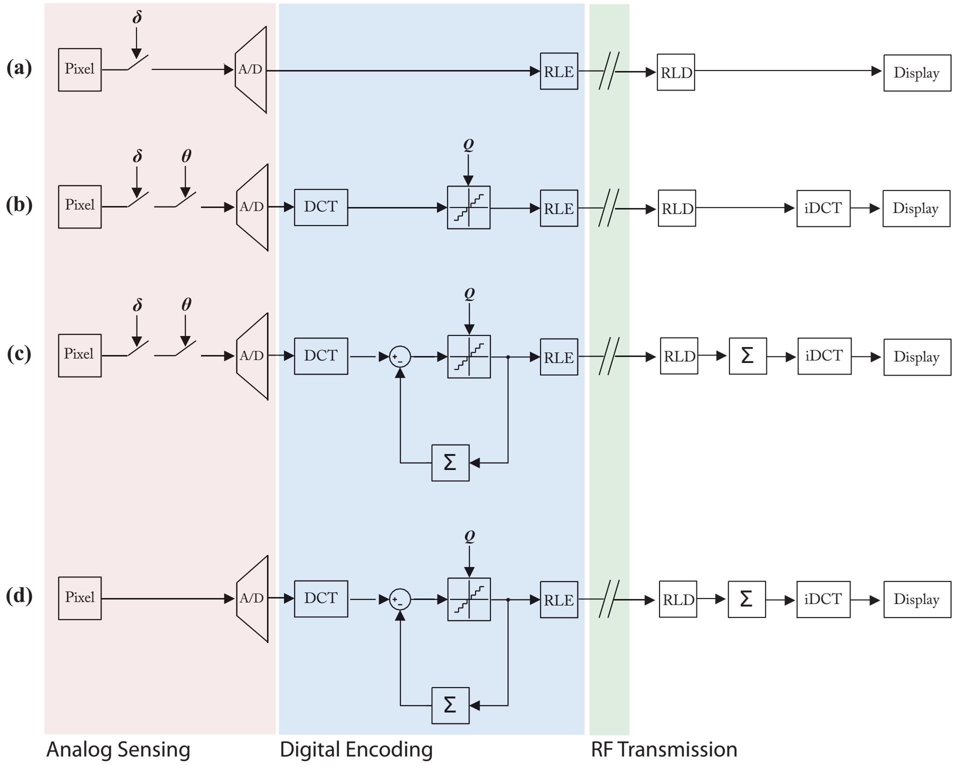

Figure A.3: Block Diagram of the four encoders analyzed. (A) Change Triggered Pixel Refresh, (B) Change Triggered DCT Refresh, (C) Change Triggered DCT DPCM and the conventional (D) DCT DPCM encoder.

are flagged as significant, digitized by the ADC and transmitted.

One immediate limitation of this coding method is the cost of transmitting pixel locations in addition to the actual updated intensity value. While conventional raster scanned image readouts implicitly embed pixel addresses in the output order, selectively sending pixels that change require an address tag for each pixel. Simply attaching the address for a pixel is unfeasible since even for a small 128x128 imager, each address tag would require 14-bits, almost twice the amount of the pixel data. In most cases, this would effectively negate any compression gain, and can very well lead to an expansion in the output data rate.

However, under the assumption that the majority of pixels from frame to frame do not change, and the assumption that pixels which do change are adjacent to each other, run-length encoding (RLE) can be used as a simple and efficient method to encode pixel positions. Here the array of pixels is treated as a 1-D vector (through a raster scan order). The data stream begins by transmitting the run length (number) of unchanged pixels before the first changed pixels. When the first changed pixel is encountered, a second run-length is computed for the number of contiguous pixels from that location that do change. Finally, the actual intensity values of these changed pixels are appended to the bit stream. Both run lengths and pixel values are coded as 8-bit values.

All of the image processing and decision making is performed inside the pixel array. Although the performance of this coding method suffers compared to the more advance DCT block based approaches, the advantage lies in the sheer simplicity of implementation. A full digital processor (microcontroller or DSP) is not needed, only a simple counter for the run-lengths followed by some basic logic for interfacing with a transmitter.

A.2.2 Change Triggered DCT Refresh (CT DCT Refresh)

The main shortcoming of the pixel refresh coding is that it does not adequately exploit the large spatial redundancy inherent in image data to further increase the compression rate. Transform coding is widely used in image and video compression to more efficiently represent image data in the frequency domain. The discrete cosine transform (DCT) is a near optimal transform for natural image data which compacts the image input into a few spectral coefficients.

Figure A.3 shows the block diagram for the CT DCT Block Refresh system. Encoding begins by treating each pixel as a member of a block rather than an independent entity in the pixel refresh case. The pixel array is partitioned into 8 by 8 pixel blocks. A new parameter, Θ, is used to set the block change threshold. If a block contains Θ number of pixels that exceed the δ change threshold, then it is flagged as significant for coding. These two parameters are used selectively gate which blocks to process. Blocks deemed inactive are wholly ignored in the subsequent signal chain.

Significant blocks are digitized followed with the DCT to produce a matrix of 8 by 8 DCT coefficients. A uniform quantization factor, Q, is used to scale and truncate the transformed image. Higher values of Q result a heavier quantization, which sets more of the DCT coefficients to zero. Coefficients are vectorized in the standard zigzag fashion which ranks coefficients in order of increasing frequency. Each non-zero coefficient has a 4-bit value indicating the number of preceding zeros followed by the actual value. Since the DCT transform outputs 12-bit values from the 8-bit pixel data, the actual number of bits to required to represent a coefficient is simply,, for the value plus the 4-bit run length.

The DCT coding architecture generally performs much better than single pixel coding, since it compacts a whole block of pixels into a relatively small number of coefficients and is scalable by setting Q. It is important to note that this and the pixel update refresh scheme require no frame buffer, just as in the CT Pixel Refresh case. For the DCT Block Refresh, only the memory required to code one 8x8 block of pixels is needed.

A.2.3 Change Triggered DCT Differential Pulse Code Modulation (CT DCT DPCM)

More compression gain can be realized by sending not just the transforms of the raw block data, but by transmitting the difference of the transforms using differential pulse code modulation (DPCM), although at a cost of now requiring a frame buffer. Typically values inside a block exhibit a large correlation from frame to frame, even as they undergo change. Sending a differentially coded update, rather than the raw value takes advantage of this correlation to reduce the amount of data that is needed to be transmitted.

The coding scheme operates as follows. An incoming block is flagged as significant and DCT coded if Θ number of pixels exceed the δ threshold, in the exact same manner as before. However, instead of quantization as before, the transformed coefficients are subtracted with the previous frames coefficients to produce a differential value. It is this value that is quantized by Q and run length coded (Fig. A.3).

In addition to sending the differential coefficient update, the encoder also takes the quantized differential coefficients and uses it update the frame buffer so that the encoder always has the same compressed (distorted) copy of the previous frameÕs image. This enables the encoder to operate as a closed look DPCM, which eliminates the accumulation of error arising from quantization and small drifts over time.

The differential encoder will usually produce a significantly reduced data rate for the same visual quality (Q) since it de-correlates the pixel data in both space and time, resulting in more zeros in the DCT coefficient matrix. However, it comes at a cost of a frame buffer, which may or may not be a significant penalty. For low resolution imaging, the frame buffer could very well fit in the internal memory provided by the digital processor.

4. Conventional Closed Loop DCT Differential Pulse Code Modulation (DCT DPCM) As a reference, a conventional DCT DPCM encoder [121] was implemented to provide a benchmark against the other three coding architectures. The encoder operates in the same fashion as the CT DCT DPCM, except without the change triggered block processing. Each block is continuously processed, irrespective of the change detection circuitry. This serves as a baseline to show the power and bandwidth savings of the CT encoders while assessing the impact on distortion and image quality.

A.2.4 Computation and Energy Efficiency

The power consumption of the video encoding system can be divided into three parts - the energy consumed by the pixel array and ADC to acquire the image, the energy consumed by the digital processor to process and compress the data, and finally the energy required to transmit the resulting bit stream,

$$E_{frame} = E_{sensor} + N_{pixels}E_{ADC} + N_{ops}E_{DSP} + N_{bits}E_{TX} \tag{A.1}$$

Conventional video coding systems are very successful in reducing the power required at the transmission channel by compressing the image data, hence reducing the total number of bits that are sent. While all modern coding architectures transmit a minimal of data during periods of low activity, the sensor and digital processor must still be operated continuously at full power in order to make that determination, even if the scene does not vary. Therefore, in scenarios where only intermittent visual activity is observed, the static power dissipation of the sensor, ADC and processor will limit the lifetime of the sensor.

The pixel-level change detection framework addresses the power consumption problem by enabling the system to not only efficiently control the power consumption of the transmitter, but also the ADC and digital processor by detecting activity at the focal-plane. Here all operations are gated by the presence of intensity changes (motion). This reduces the static power dissipation of the system to only the amount required to operate the pixel array, which is typically orders of magnitude less than the external processor.

For the simple pixel refresh encoder power consumption is directly related to the number of pixels that change. The energy required to code one frame is the static energy consumed by the sensor array, the energy required to digitize changed pixels and the energy required the transmit the zero run-length and pixel values (R_{bits}),

$$E_{frame} = E_{sensor} + \sum_{k=1}^{N} a_k E_{ADC} + R_{bits} E_{TX}. \tag{A.2}$$

Here a_k represents a gating variable for each pixel indicating whether or not it has crossed the change threshold. The energy consumed by the digital processing for this architecture can be considered negligible since only a simple counter is required to tabulate the zero change run lengths.

Switching over to the CT DCT based encoders adds an additional factor that accounts for the energy used to perform the DCT on a block.

$$E_{frame} = E_{sensor} + 64 \sum_{k=1}^{M} b_k E_{ADC} + \sum_{k=1}^{M} b_k E_{DCT} + R_{bits} E_{TX}. \tag{A.3}$$

The variable b_k gates the M 8×8 blocks to only perform the ADC and DCT (E_{DCT})operations over blocks that exhibit change.

For the baseline DPCM encoder, power consumption is simply the constant cost of operating the sensor, ADC and performing the DCT on each block plus the energy cost of transmitting the output bit stream,

$$E_{frame} = E_{sensor} + 64 M E_{ADC} + 64 M E_{DCT} + R_{bits} E_{TX}. \tag{A.4}$$

It should be observed that the two last encoding methods also require a frame buffer, but depending on image size and memory type (on-die SRAM in the processor), may only incur a negligible increase in amount of power dissipation.

A.3 Implementation Example

Actual power consumption figures are heavily dependent on hardware implementation. However, an approximate model for the power efficiencies of each architecture can be modeled using known figures from available components. For this paper, the hardware used in [118] was used as a model for the sensor and digital signal processing energy costs.

The energy consumed by the sensor was derived from [117] which shows that the change detection sensor requires 4 mW to power a 90×90 pixel array at 30 frames/second, corresponding to an energy expenditure of 16.5 nJ/pixel. The ADC used was a 1 MSPS model with a power consumption figure of 3.9 mW. Since each pixel is one sample, the energy to digitize a pixel is 3.9 nJ.

For the power consumption of the digital processor, the PIC32 on the board requires 77.6 mW at the operating frequency of 20 MHz. A fast, integer only DCT implementation [122] can be performed with 2450 operations. This amounts to 9.5 μJ to transform one 8×8 block.

The transmitter was based on a commonly available, low power 2.4 GHz ZigBee modules. From the parameters on the datasheet, the equivalent energy to transmit a single bit of data is 224 nJ. It is worth noting that different figures can be easily obtained by varying the implementation. For example an improved sensor or custom logic for the DCT would significantly reduce the power consumption at each of those stages. However, the figures here serve to provide not only an estimate of real world power efficiency, but to also illustrate the tradeoffs and gains in using the focal-plane CT circuits to manage the power usage of the video encoder.

A.4 Results

Example output from the fabricated 90x90 pixel CMOS imager and video compression scheme is shown in Figure A.1, and the performance of the CT Pixel Refresh compression scheme is fully characterized in [117]. To fully evaluate the performance of the focal-plane change detection based video coding architectures, computer models were used to simulate the operation of the sensor and video coder. This allowed the architectures to operate on a fixed data set consisting of well-known video test sequences as well as to fully characterize the effects on distortion, compression rate and power consumption of each encoding parameter (δ ,Θ and Q).

The test sequence hall.cif is a commonly used surveillance type reference video to evaluate video coding architectures. The 200 frame CIF (352×288) resolution file contains imagery similar to raw video output of the sensor in Figure A.1. The compressed outputs of this sequence were used to generate the data for each of the compression architectures.

A rate-distortion (RD) plot is a useful tool to compare the performance of each encoding architecture by plotting the distortion introduced by the encoder versus the compression rate. Figure A.2, shows the basic rate-distortion curves for each of the encoding architectures. Distortion is expressed using the peak signal-to-noise ratio (PSNR) of the maximum pixel value versus the mean-square-error (MSE) of the encoded video data from the original source.

$$\mathrm{PSNR} = 10\log_{10}\frac{255^2}{\mathrm{MSE}} \tag{A.5}$$

Compression rate is normalized to bits per pixel which is obtained by taking the size of the compressed bit stream divided the total number of pixels encoded. Hence a rate of 1 bit/pixel corresponds to a compression ratio of 8:1, since the original pixel data contains 8 bits. Lower numbers indicated a higher compression ratio and smaller output data rate.

Before a full comparison of each architecture could be conducted, it was necessary to determine the optimal parameters for δ and Θ for the CT DCT encoders. Figure A.2 shows the rate-distortion curve for both the baseline DCT DPCM encoder and the CT DCT DPCM encoder with δ's of 2 to 8 and Θ's of 4 and 8 pixels. Each of the points was generated by varying the parameter, Q which was varied from 16, 24, 32, 48, 64, 96, 128 to set the distortion level and output data rate. Performance of the encoder matches closely to the non-change triggered encoder except for the case where δ=8, Θ=4 curve when the distortion rapidly increases due to insensitivity to actual change events. The maximum value for δ and Θ before significant features are dropped is then δ=5, Θ=8. This sets the optimal parameters which is sufficient to reject low level noise, but not

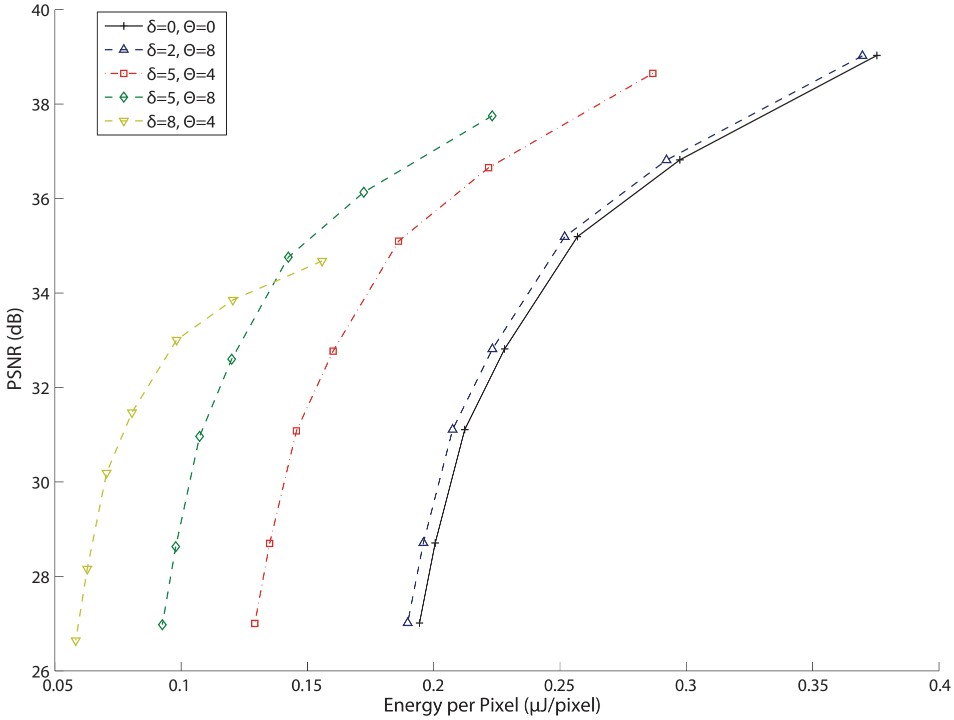

Figure A.4: Energy-Distortion curves by varying δ and Θ for the CT DCT DPCM encoder under the same conditions as Fig. 3. Again, the $\delta = 5$ and $\Theta = 8$ case is optimal in using the least amount of energy per pixel while maintaining distortion levels similar to the conventional DCT DPCM encoder. Increasing the thresholds to $\delta = 8$ and $\Theta = 4$ for further energy savings introduces distortions significantly limiting the achievable PSNR.

actual events of interest.

Interestingly, in all of the cases where the CT is active, the CT DPCM encoder actually performs better from a rate-distortion standpoint Ð the gain in bandwidth reduction due to the CT is greater than the increase in distortion due to discarding inactive blocks.

Figure A.4 shows a second related graph that compares the energy expenditure versus distortion (ED), where the energy per pixel was calculated using the numbers described in the previous section. As expected, for low values of δ and Θ, the energy and distortion curves match closely to the conventional DCT DPCM encoder, since simple noise was enough to trigger the encoding of a block resulting in very few rejected blocks.

Increasing the thresholds shifts the curve leftward, corresponding to a reduction in energy expenditure, while largely maintaining constant PSNR values until the (8,4) case.

For the previously found optimal values of δ=5 and Θ=8, the reduction in the amount of blocks processed was 67%, leading to an overall 51% reduction in power consumption at a minimal impact in PSNR. Increasing the thresholds beyond this point further reduces the power consumption, but distorts the ED graph, indicating data loss.

This case illustrates the advantages of going from simple conventional DCT DPCM to using a CT DCT DPCM encoder. Significant power savings can be achieved by incorporating the power management as upstream in the signal chain as possible. For this sequence with moving events, the reduction in power was roughly one half by using the CT to gate the processing of blocks.

A.5 Comparison of Each Encoder

The next step was to evaluate the performance of each architecture type. Rate-distortion curves(Fig. A.5) were generated by varying the Q, used to quantize the DCT coefficients and by varying δ for the simple CT Pixel Refresh encoder. As expected, the DCT based compression architectures all performed similarly in terms of distortion, which is largely dependent on the quantization factor Q. However, the DCT Refresh architecture trails the two DPCM architectures in compression ratio at an equivalent PSNR since more data is needed to transmit an entire block rather than just a differential update. The CT Pixel Refresh encoder is generally suboptimal and cannot achieve low distortion levels even at a high bit rate, but it is important to keep in mind the simplicity of implementation. In general the CT DCT DPCM encoder has the best rate-distortion tradeoff, but with a slightly higher overall distortion level than the conventional DCT DPCM encoder.

Similarly, an ED graph (Figure A.6) was generated for each separate architecture in the same manner. The ED graph shows that the CT DCT DPCM encoder has the best visual quality to energy expenditure ratio - achieving the low distortion levels of the DCT DPCM encoder while minimizing the energy usage by discarding irrelevant blocks. The CT DCT Block coder has good performance at high levels of Q, but is hampered by the

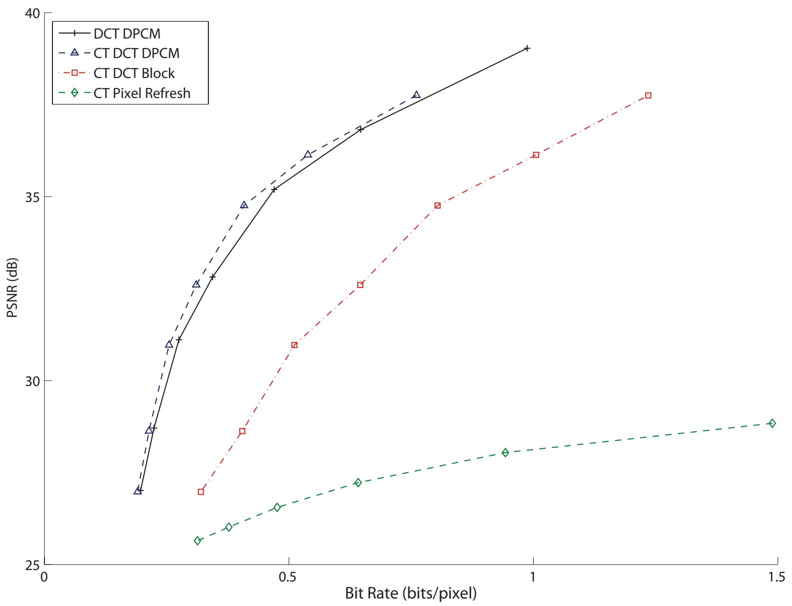

Figure A.5: The DCT encoders were set to δ = 5 and Θ = 8, with Q ranging from 16 to 128, and d for the CT Pixel Refresh encoder ranged from 2 to 15. As shown previously, the CT DCT DPCM encoder has the best rate-distortion.

energy needed to transmit more data at less aggressive DCT quantization levels due to the inefficiency in sending full block refreshes rather than differential updates. Again, the CT Pixel Refresh encoder is generally suboptimal because of the high data rates generated by sending pixel updates rather than the more efficient method of sending DCT block coefficients, resulting in increased energy used at the transmitter. It is worth noting, however, that at very high levels of distortion, the CT Pixel Refresh coder expends very little energy, albeit with a significantly impaired visual quality.

Figure A.7 shows the dynamic compression performance of the encoder over time at the point Q=96, δ=5 and Θ=8 for the DCT encoders and δ=7 for the CT Pixel Refresh. The compression rate in bits/pixel for a single frame is plotted for all 200 frames in the sequence. This illustrates that the DCT based encoders generally have much better control over the data rate (through setting Q) than the pixel refresh encoder, which is much more sensitive to both noise and actual observed change. In addition, the DCT

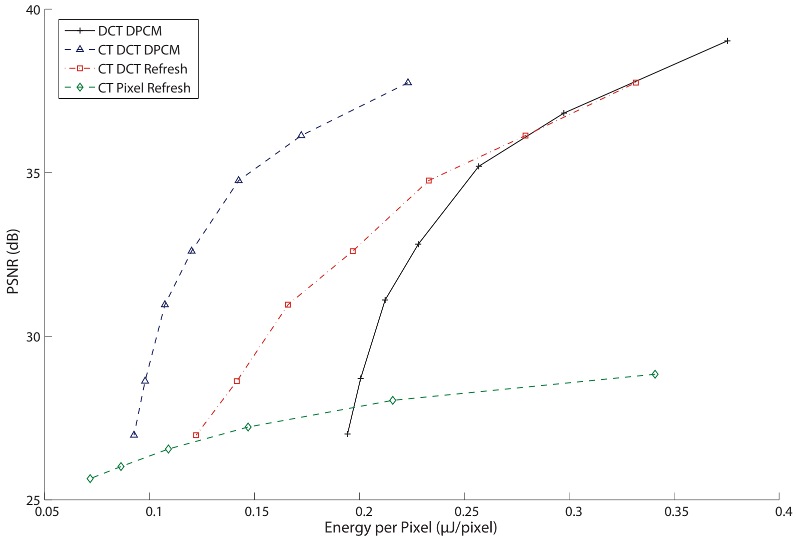

Figure A.6: Energy-Distortion curves for each encoding algorithm, under same conditions as in Figure 5. The CT DCT DPCM encoder has the greatest efficiency in achieving a distortion level with the least amount of energy required to process and transmit the video.

DPCM encoders are about twice as efficient as the DCT refresh encoder. Note that the CT Pixel Refresh encoder requires a full uncompressed encoding of the initial frames at 8 bits/pixel, incurring an initial coding and transmission cost significantly higher than the block based methods.

Next, the dynamic distortion rate of the encoder output is shown by plotting the MSE of a single frame over the entire sequence (A.8). As expected, due to the single pixel nature of the CT Pixel Refresh, the distortion varies widely and is heavily dependent on scene content. In contrast, all of the DCT encoders were able to maintain a nearly constant and similar distortion level (set by Q). Significantly, despite the lack of feedback inherent in the design of the CT mechanism at the focal-plane, the drift between the reference fully closed loop DPCM encoder and the CT encoders was minimal suggesting that aggregating the change detection over a block of pixels simultaneously minimized the effect of noise (a few pixels reporting change) while preserving sensitivity to actual change events (many pixels reporting change).

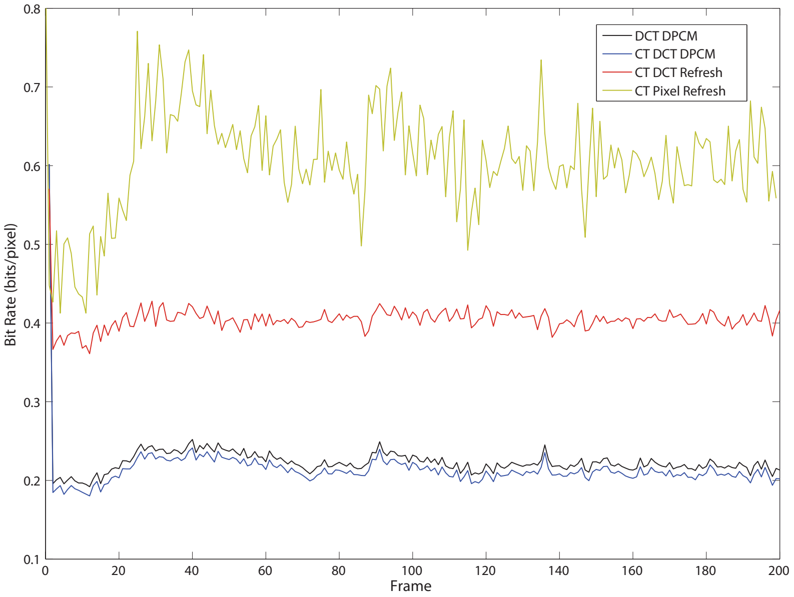

Figure A.7: A chart of the compression rate for each frame in the hall.cif test sequence. The parameters used were $\delta = 5$, $\Theta = 8$ and Q = 96 for the DCT based encoders and $\delta = 7$ for the CT Pixel Refresh encoder. The CT Pixel Refresh encoder is least optimal, and incurs a large initial transmission cost of 8 bits per pixel (keyframe, no compression).

A breakdown of the power usage by component is shown in Figure A.9 at the same operating points as Figure A.7 and A.8 and shows the tradeoffs in using each encoding scheme. Power consumption of the imager and ADC is largely dominated by the sensor in all cases and is essential constant and smaller than the other two components in all cases. DPCM encoding incurred the least energy cost in transmission due to the compression efficiency of sending differential DCT coefficient updates. However, the baseline DCT DPCM encoder has large processing cost, since each block in every frame was continuously processed. Moving to the CT Block Refresh saved on processing energy, since only significant blocks were transformed, but at a cost of decreased compression efficiency and increased bandwidth and transmitter energy. The CT DCT DPCM encoder, on the other hand, can be viewed as the optimal solution since it had both the compression efficiency of the baseline as well as the processing efficiency as a result of using the CT to

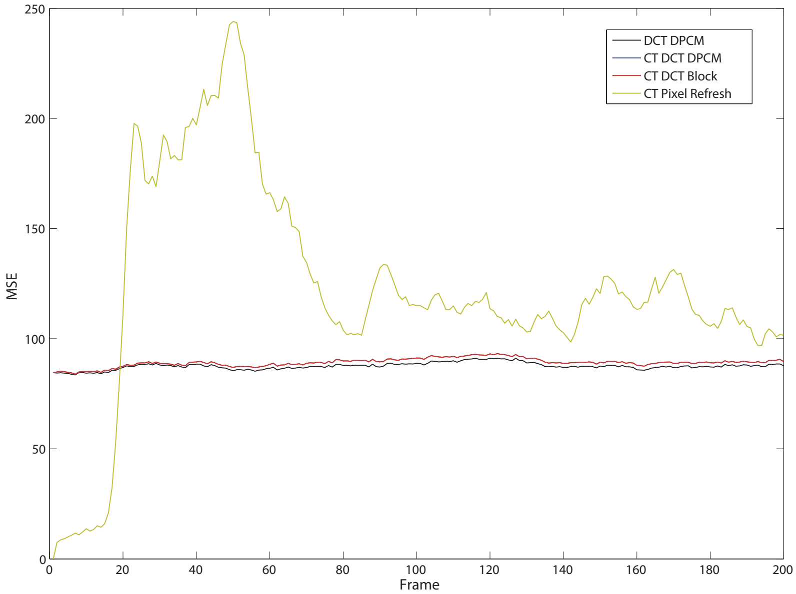

Figure A.8: A chart of the distortion level (MSE) for each frame in the hall.cif test sequence. The parameters used were δ = 5, Θ = 8 and Q = 96 for the DCT based encoders and δ = 7 for the CT Pixel Refresh encoder as in Figure 7. The two CT DCT encoders have nearly identical distortion levels to each other and do not appear as distinct lines.

selectively code blocks. In the case of the pixel refresh, while the digital signal processing cost was minimal, the cost of transmission was significant, because of compression inefficiencies.

Finally sample outputs of each encoder are shown in Figure A.10 for the first frame, the 20th frame and the final 200th frame of the sequence to visually illustrate the compression related distortion. As expected, each of the DCT based encoders look very similar with the typical blocking artifacts from DCT coefficient quantization. The CT Pixel Encoder was the only one to suffer from artifacts from using the focal-plane change detection. Incomplete change detection manifests itself as missing and trailing pixels necessitating the use of a periodic frame fresh to obtain a clear image and reduce error accumulation. As mentioned previously, the use of CT over a whole block largely

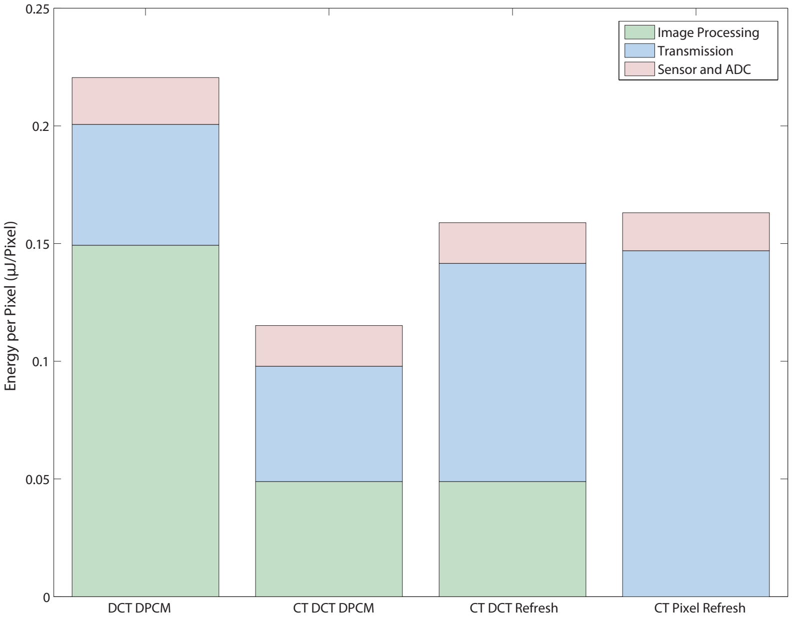

Figure A.9: Energy allocation for each encoder using the same operating parameters as Figures 7 and 8. The use of the CT significantly decreases the amount of energy necessary for image processing since only a fraction of the blocks are transformed. Sensor and ADC energy costs are nearly equal, with the constant sensor energy usage as main factor. Although the CT Pixel Refresh Coder requires a minimal of computation cost, this is offset by the decrease in compression efficiency and higher energy usage at the transmitter.

mitigates this issue since change detection over multiple pixels is much more effective at preserving significant updates while rejecting noise. Consequently, the visual impact of using CT DCT encoding was minimal, compared to the fully closed loop DCT DPCM encoder.

A.6 Discussion

We show that the use of focal-plane change triggering (CT) as a gating method to intelligently manage the operation of a video encoding system resulted in significant power reduction at a minimal cost in compression performance and increased distortion. Using the energy consumption figures from systems parameters extracted from measurements on the system of Figure A.3, a simple 128x128 pixel video sensor operating at 10fps will consume on the order of only 20mW including RF transmission of the compressed data stream. Future systems that optimize the design of the sensor, perhaps by integrating portions of the spatial transform onto the focal plane [112, 113, 114, 115, 116], will further reduce this number. The techniques presented here provide the framework for building highly power efficient video sensor systems suitable for battery powered, wireless operation.

Appendix A is largely a reprint of material published in the 2009 Public Library of Science PLoS One Journal: Y. M. Chi, R. Etienne-Cummings and G. Cauwenberghs, "Focal-Plane Change Triggered Video Compression for Low-Power Vision Sensor Systems," *PLoS One*, 2009. The author was the primary author and investigator of this work.

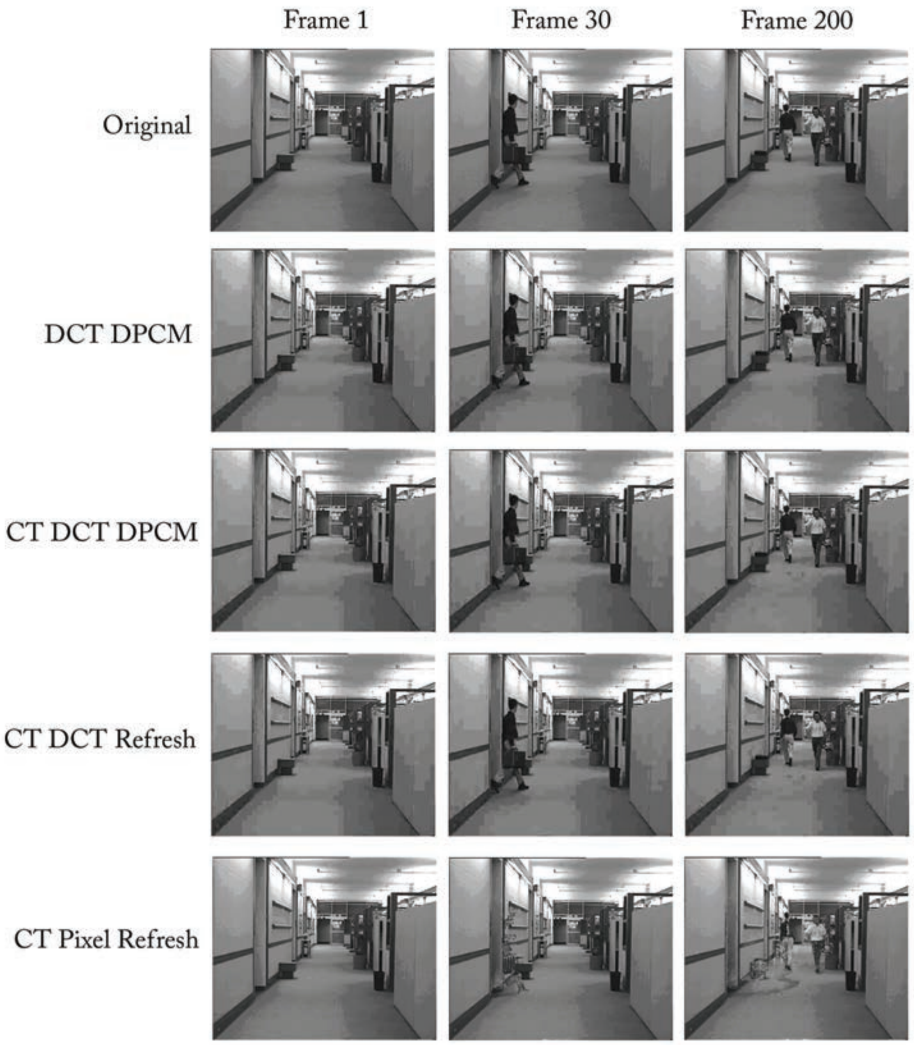

Figure A.10: Sample frames from the original video test sequence and the compressed output from each encoder using the parameter Q = 48, $\delta = 5$ and $\Theta = 8$ for the DCT encoders and $\delta = 10$ for the CT Pixel Refresh. Frame 1 is the start of the sequence, Frame 30 is where a man begins to enter the scene and Frame 200 is the final image in the video. All of the DCT encoders have similar compression artifacts, mainly a result of heavy DCT quantization. The CT Pixel Refresh coder does not have blocking artifacts, but missing and trailing pixels.

Appendix B

High-Speed Histogram Image Sensor

B.1 Introduction

Adaptive optical systems are highly useful for correcting for the distortions introduced by atmospheric turbulence in a wide class of applications including high speed laser communications and ground based astronomy [123]. One class of algorithms, stochastic gradient descent [124] [125] has been shown to be effective for correcting optical aberrations.

One challenge, in particular, is generating the quality metric used in a closed loop adaptive system. Image quality metrics that measure the sharpness or focus of the image are critical for adaptively optimizing the system. Producing metrics at high frame rates using conventional image sensor technologies becomes highly demanding due to the need to acquire and process a large number of pixels. As an example, one effective metric, the J_2, is defined as the squared value of each pixel, summed globally. For a sensor size of 128×128 pixels running in a closed loop control application at 10,000 frames/sec, a pixel clock of 164 MHz is required to digitize all the pixels alongside a suitable high speed digital processor. In addition, acquisition and processing must occur after frame exposure, introducing additional lag into the control loop. To date, most high speed control systems have relied on the use of desktop PCs and expensive, scientific grade image sensors [123].

As an alternative, previous works have demonstrated the use of focal-plane processing to produce image/beam metrics directly at the sensor [125]. In this paper, we

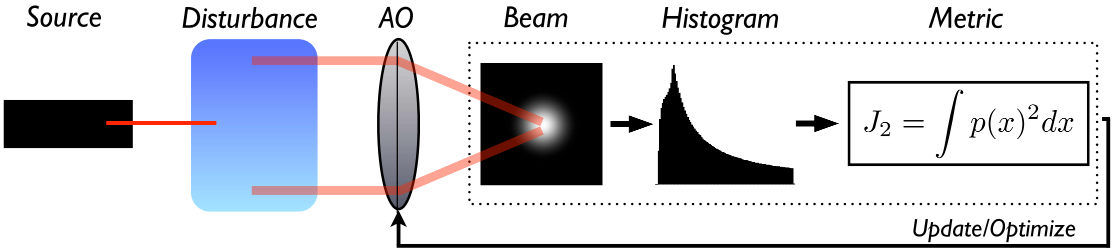

Figure B.1: Intended real-time optical control application. The sensor computes histogram based beam quality metrics which are used to adaptively optimize the optical system at a very high frame rate.

present a high speed image sensor (excess of 10,000 frames/sec) designed for real-time closed loop optical control systems (Fig. B.1). The sensor directly outputs image statistics in the form of the image histogram without the need to scan and read out pixels in the array. Computing the metrics used in adaptive optics, such as the J_2, in the histogram domain is much more computationally efficient since the number of data points processed is set only by the bit depth of the pixel (typically only 256 to 1024) and is independent of the array resolution.

The scope of this paper focuses on the core functionality of the CMOS image sensor, describing the operation of the pixel-level histogram circuit and the 10-bit column-parallel ADC.

B.2 Chip Description

A micrograph of the sensor is shown in Figure B.2. The core of the chip is an 128 by 128 pixel array containing the circuits for focal-plane histogram circuit. Row and column registers at the periphery facilitate timing and optional windowing operations. The ADC is located at the end of each column of pixels.

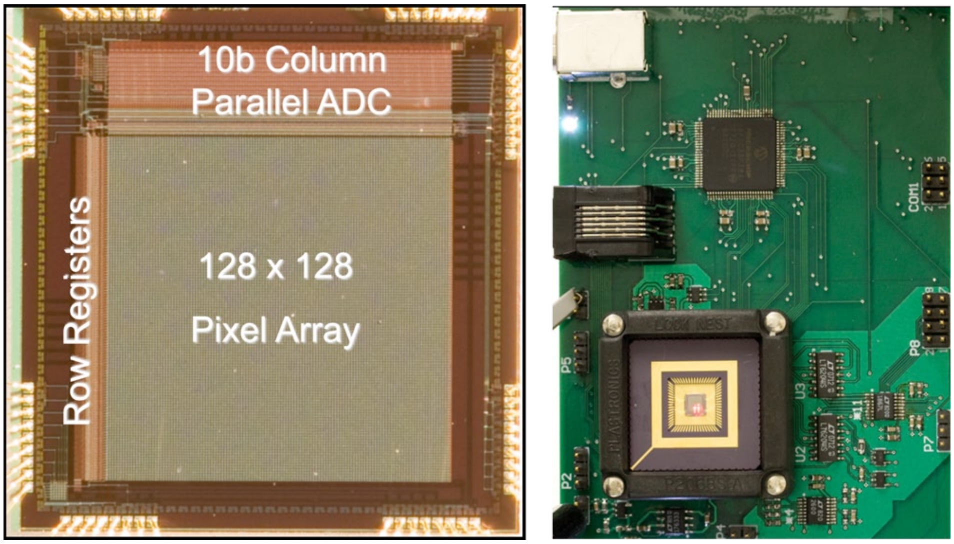

Figure B.2: Micrograph of the histogram image sensor and sensor integrated as part of a test system.

B.2.1 APS with Focal-Plane Histogram Computation

The pixel design (Fig. B.4) is based on the standard 3-T APS [126] (M1-M3), but with the addition of just a single extra transistor (M4). In histogram mode, transistors M2 and M3 operate as a differential pair with M4 providing the tail bias current. The devices are biased in sub-threshold for low power operation. The drain of M3 is the pixel's output and is joined together globally to sum the currents from all pixel into an output pin. Since the histogram circuit incurs only a single additional transistor at the pixel (Fig. B.3), impact on fill-factor and image quality is minimal. For high-speed imaging, it is especially important to minimize the impact on the sensor's sensitivity.

Histogram computation operates in tandem with photocurrent integration and begins immediately after reset. The differential pair in the pixel can be thought of, roughly, as a comparator between the discharging photodiode voltage, V_{pd}, at the input of M2 and a global threshold, V_{th}, at the input of M3. For simplicity, the circuit is first analyzed with V_{th} as a fixed value, although different wave forms can be used to obtain different histogram responses (a ramp is illustrated in Fig. B.4).

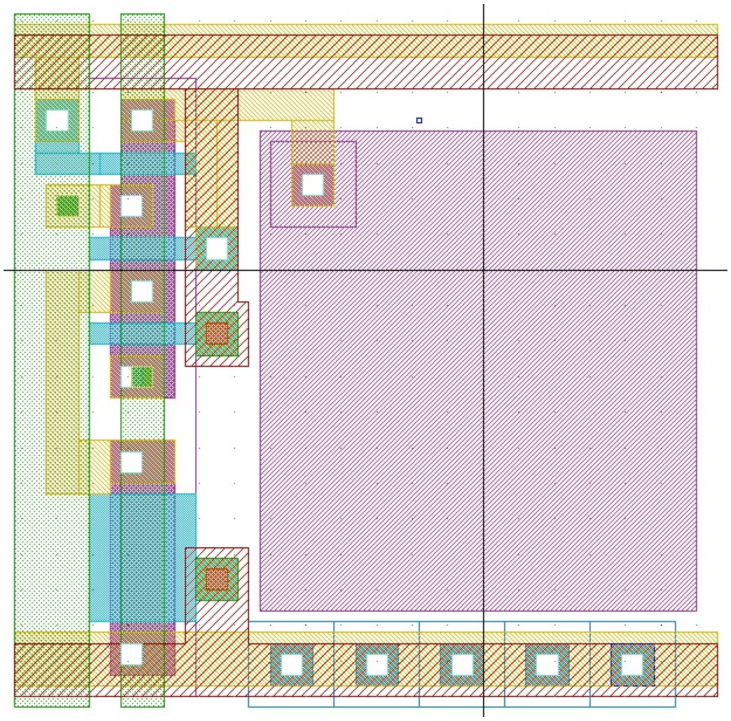

Figure B.3: Layout of the 19.5μm by 19.5μm pixel.

The photodiode voltage, V_{pd} during the frame can be written as,

$$V_{pd} = V_{rst} - \frac{i_{pd}}{C_{pd}} t \tag{B.1}$$

where V_{rst} is the reset voltage, i_{pd} is the photocurrent, C_{pd} is the integrating capacitance and t is the time into the current integration cycle. The time it takes to cross the threshold V_{th} is then,

$$t_{cross} = \frac{C_{pd}(V_{rst} - V_{th})}{i_{pd}}. \tag{B.2}$$

Thus, brighter pixels (those with larger i_{pd}) drop below the threshold faster than dimmer ones. At point, t_{cross} the pixel outputs its bias current, I_{bias} to the global summing line at the drain of M3 for the remainder of the integration period.

The aggregate effect of all the pixels in the array operating in this fashion results in a global current, I_{cdf}, which represents a time encoded, cumulative histogram (CDF) of the image. The current, I_{cdf}, at time t is the sum of all pixels, I_{cdf}/I_{bias}, with a photocurrent greater than,

$$i_{pd} > \frac{C_{pd}(V_{rst} - V_{th})}{t}. \tag{B.3}$$

In contrast to a conventional histogram, the index bins are reversed and displayed in decreasing, rather than increasing order. However, simply differentiating and then reversing all the samples of I_{cdf} results in a conventional histogram.

Devos et al. [127] implemented a video frame rate histogram sensor using a broadly similar architecture for exposure correction. In their version, the differential pair was configured as a full CMOS comparator, including the complementary active load. By removing the active load, the histogram becomes smoothed at lower light intensities due to the $tanh$ response of the differential pair. However, the simplification of the circuit allows this implementation to maintain a high pixel fill factor and image quality. At the same time, response to the bright intensities that contain the useful metric information remains unaffected.

As mentioned previously, different waveforms can be used for V_{th} to change the mapping between the time index and pixel intensity value. In practice, a simple fixed value or linear ramp produces good results without introducing additional circuit complexity.

Power consumption for this circuit is dominated the need for each pixel to be actively biased with a current source, approximately 50 nA, and scales directly with array size. The amount of power consumed does not vary significantly with frame rate. Only a simple medium speed amplifier and ADC are required to process the CDF data from the sensor. Since the number of samples/bins is relatively small (256 for 8-bits), a simple microcontroller can handle all the data processing operations.

B.2.2 10-bit Column-Parallel ADC

Aside from the histogram mode, the imager can also function as a conventional APS with the on-chip 10-bit column-parallel ADC for characterization and image acquisition purposes. In imaging mode, transistor M4 is turned off and M3 functions as a row-select switch, connecting the source follower M2 to a column bias current, reverting the pixel to a standard 3-T APS [126].

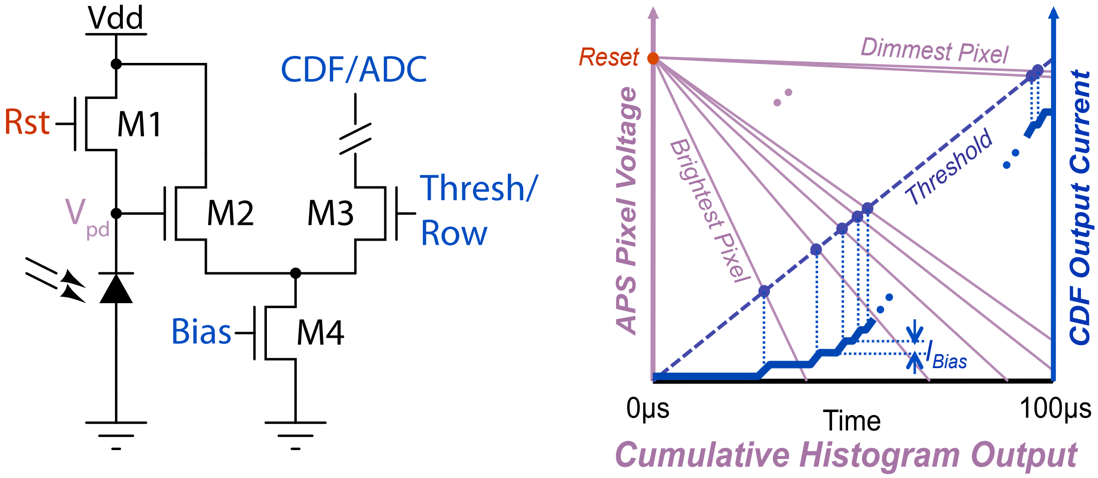

Figure B.4: Schematic of the histogram APS circuit along with an illustration showing the generation of a cumulative histogram by summing the currents from all the pixels in the array.

Figure B.5 shows the block diagram of the ADC along with its timing diagram. The integrated photodiode voltage from reset, ΔV_{pd} is stored on C_{sample} by asserting the feedback switch around the opamp at the end of the frame cycle. After sampling, the opamp now functions without feedback as a comparator and the pixel is reset, pulling the inverting input of the opamp, V_n, up by ΔV_{pd} and forces the output low. While the pixel is held in reset, a global ramp signal, V_{ramp} connected to the non-inverting input begins to increase alongside with a count signal. As the ramp increases by amount ΔV_{pd} from its initial state, the comparator's output goes high, triggering the ADC's latch circuit to store the count, which is the digital representation of ΔV_{pd}.

The ADC, in the described mode, performs delta difference sampling (DDS) by subtracting the pixel voltage from the next frame's reset voltage rather than correlated double sampling (CDS). While this doubles the amount of $\frac{kT}{C}$ reset noise, the operation still effectively removes offset fixed pattern noise (FPN), producing clean images.

The concept and implementation of the ADC circuit is similar to previous work [128] [129] but with one main difference - the ramp is coupled to non-inverting input of the opamp/comparator rather than through a capacitor network that connects both the APS signal and ramp both to the inverting input. This reduces the number of

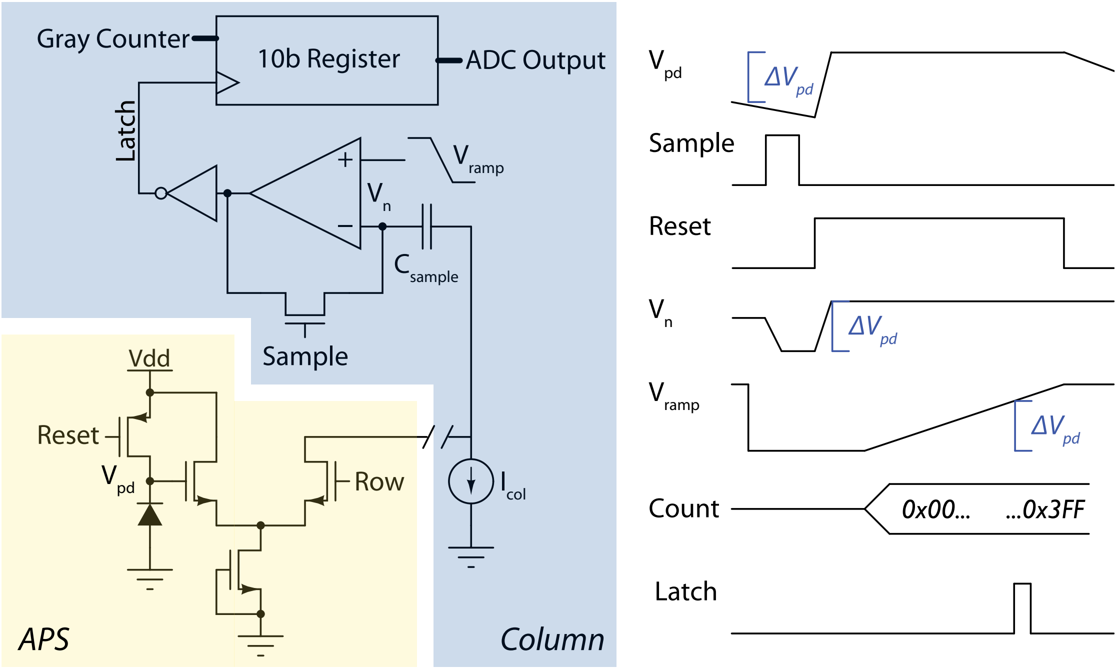

Figure B.5: Schematic of the column-parallel ADC and timing signals.

switches required as well as the need for two matched capacitors.

B.3 Results

The image histogram sensor was integrated on to a test board (Fig. B.2) containing a transimpedance amplifier and ADC to digitize the CDF current along with a USB data acquisition system.

To test the functionality of the histogram circuit, the sensor was illuminated by a laser beam of constant intensity but at varying degrees of focus. Figure B.6 shows the oscilloscope traces of the CDF current for two different extremes of focus along with the reset timing signal for 10,000 frame/sec operation.

In the upper trace, the beam was completely unfocused across the array. Accordingly, the CDF output exhibited a large step towards the end of the integration period corresponding indicating a large distribution of relatively dim pixels in the image. In the lower plot, the beam was projected so that it was focused on the center of the array.

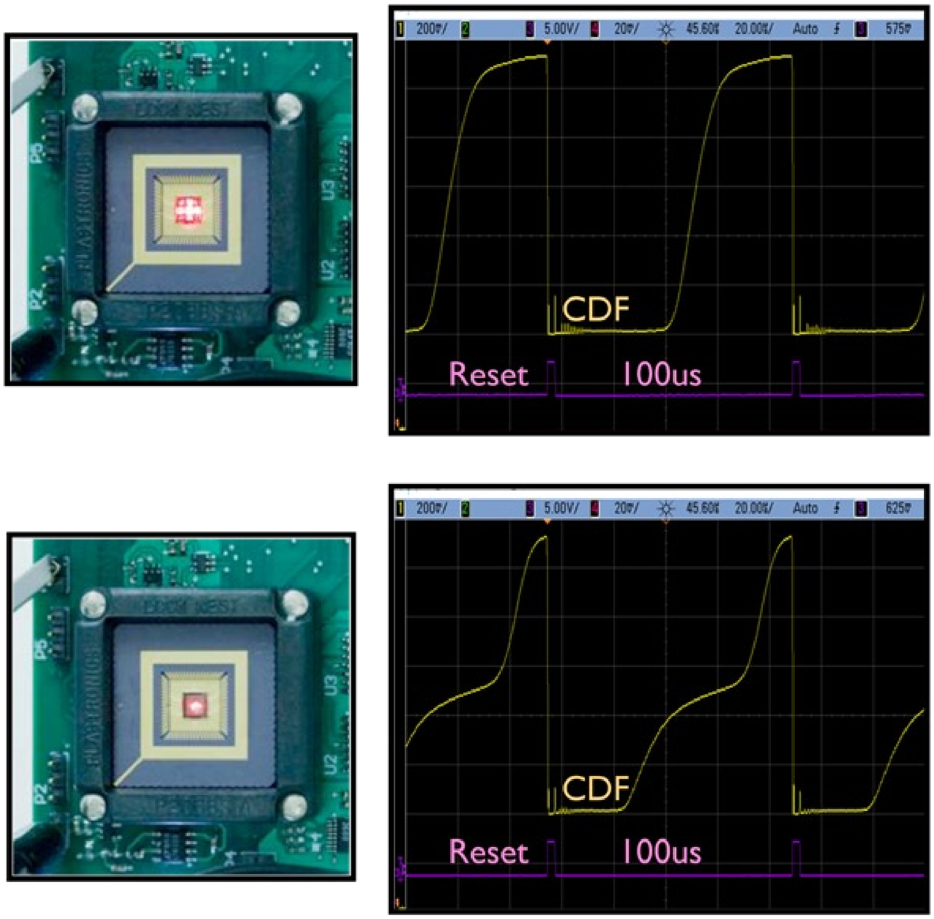

Figure B.6: Oscilloscope traces of the CDF output is shown for two beam profiles along with reset timing for 10,000fps frame rate.

The CDF output showed two steps – one near the start of the frame corresponding to the bright pixels illuminated by the beam and a step at the very end corresponding to the pixels at the periphery.

A more detailed plot of the CDF, digitized and acquired into the computer, is shown in Figure B.7. For comparison, a digitally generated version CDF of the same beam images was made from the sensor's ADC output. The beam image from the ADC is also shown on the side. As expected, the cumulative histogram directly from the pixel's analog circuit matches closely with the one from sampling each pixel and computing it digitally. The only deviation is a slight offset, along with a smoothing at lower light intensity bins due to the *tanh* response of the differential pair.

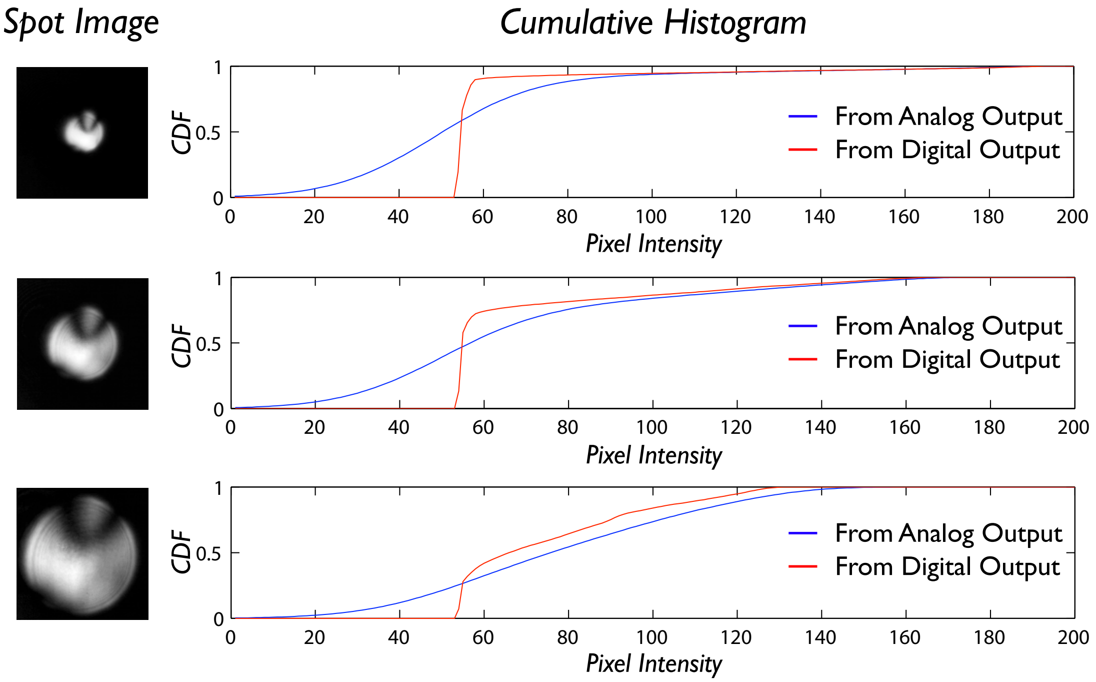

Figure B.7: Cumulative histogram of three beam profiles along with the image, acquired through the on-chip ADC. The analog CDF computed directly on the focal plane is compared with the digitally generated CDF from the ADC output.

To characterize the response pixel and ADC, the image sensor was illuminated by a diffuse, uniform light source at various intensity levels. At each light step, the temporal noise variation and mean ADC code was recorded to obtain the photon transfer curve (PTC), shown in Figure B.8. From this plot, the dynamic range and resolution of the sensor is 9.4-bits matching well with the column-parallel ADC design. Fixed pattern noise was measured to be negligible.

Figure B.9 shows two sample images taken from the sensor under indoor room illumination at standard video rates. The pictures are both qualitatively clean and free of noise, showing the image quality of the sensor even with the addition of the pixel-level histogram circuit.

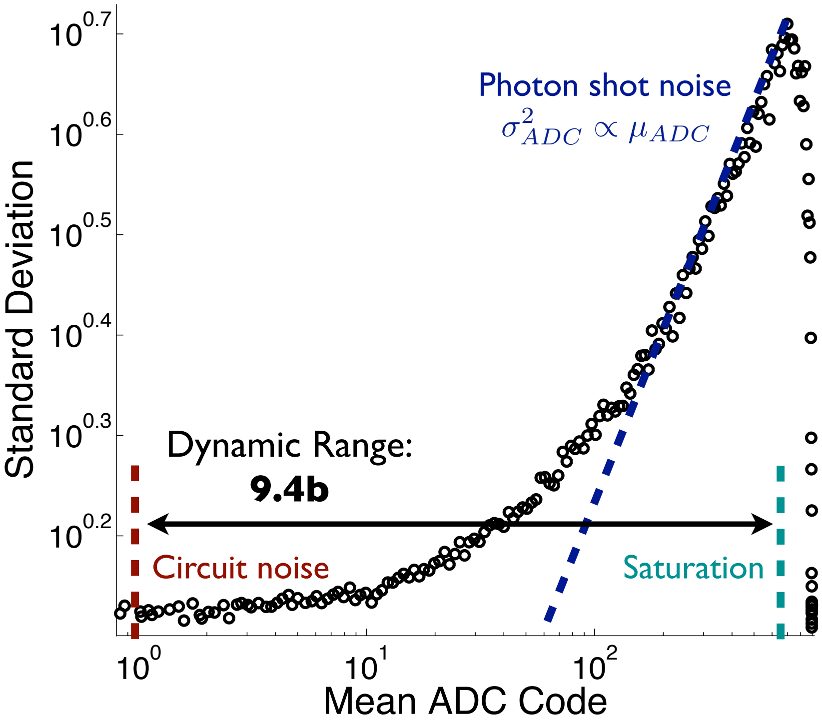

Figure B.8: Photon transfer curve of the pixel and ADC characterizing the dynamic range of the image sensor.

B.4 Discussion

We present a CMOS image sensor with high-speed, low complexity, focal-plane histogram computation. A summary of the sensor's specifications can be found in Table I. The 128 by 128 array directly produces a cumulative histogram output, without the need for external processing at rates beyond 10,000 frames per second while consuming only 4.3mW. Future work will address the use of the sensor as part of a closed loop, adaptive optics, control system.

Appendix B is largely a reprint of material published in the 2010 IEEE International Symposium on Circuits and Systems Conference: Y. M. Chi, G. Carhart, M.A. Voronstov and G. Cauwenberghs, "Intensity Histogram Imager for Adaptive Optics," *IEEE International Symposium on Circuits and Systems*, 2010. The author was the primary author and investigator of this work.

Figure B.9: Two sample images from the sensor.

Table B.1: HistImager Specifications

Process	0.5 μm CMOS
Chip Area	13.4mm^2
Resolution	128×128
Pixel Size	19.5 μm^2
Fill Factor	43 %
Full Well Capacity	23,000 e^-
Read Noise	34.8 e^-
ADC ENOB	9.4 b
Power Consumption	4.6 mW (CDF), 1.5 mW (ADC)
Voltage Supply	3.3 V

Bibliography

[1] Xiao-Fei Teng, Yuan-Ting Zhang, C.C.Y. Poon, and P. Bonato. Wearable medical systems for p-health. *Biomedical Engineering, IEEE Reviews in*, 1:62 –74, 2008.

[2] A. Lymberis. Smart wearable systems for personalised health management: current r d and future challenges. In *Engineering in Medicine and Biology Society, 2003. Proceedings of the 25th Annual International Conference of the IEEE*, volume 4, pages 3716 – 3719 Vol.4, 17-21 2003.

[3] A Searle and L Kirkup. A direct comparison of wet, dry and insulating bioelectric recording electrodes. *Physiological Measurement*, 21(2):271, 2000.

[4] E. Huigen, A. Peper, and C. A. Grimbergen. Investigation into the origin of the noise of surface electrodes. *MEDICAL AND BIOLOGICAL ENGINEERING AND COMPUTING*, 40(3):332–338, 2002.

[5] M. Spach, R. Barr, J. Havstad, and E. Long. Skin-electrode impedance and its effect on recording cardiac potentials. *Circulation*, 34:649–656, 1966.

[6] A. Baba and M.J. Burke. Measurement of the electrical properties of ungelled ecg electrodes. *International Journal of Biology and Biomedical Engineering*, 2(3):89–97, 2008.

[7] J.D. Bourland, L.A. Geddes, G. Sewell, R. Baker, and J. Kruer. Active cables for use with dry electrodes for electrocardiography. *Journal of Electrocardiology*, 11(1):71 – 74, 1978.

[8] Alfredo Lopez and Philip C. Richardson. Capacitive electrocardiographic and bioelectric electrodes. *Biomedical Engineering, IEEE Transactions on*, BME-16(1):99 –99, jan. 1969.

[9] Babak A. Taheri, Robert T. Knight, and Rosemary L. Smith. A dry electrode for eeg recording. *Electroencephalography and Clinical Neurophysiology*, 90(5):376 – 383, 1994.

[10] Tadayuki Matsuo, Kazuhiro Iinuma, and Masayoshi Esashi. A barium-titanate-ceramics capacitive-type eeg electrode. *Biomedical Engineering, IEEE Transactions on*, BME-20(4):299 –300, july 1973.

[11] C J Harland, T D Clark, and R J Prance. Electric potential probes - new directions in the remote sensing of the human body. *Measurement Science and Technology*, 13(2):163, 2002.

[12] T.J. Sullivan, S.R. Deiss, and G. Cauwenberghs. A low-noise, non-contact eeg/ecg sensor. In *Biomedical Circuits and Systems Conference, 2007. BIOCAS 2007. IEEE*, pages 154 –157, 27-30 2007.

[13] R. Matthews, N.J. McDonald, P. Hervieux, P.J. Turner, and M.A. Steindorf. A wearable physiological sensor suite for unobtrusive monitoring of physiological and cognitive state. In *Engineering in Medicine and Biology Society, 2007. EMBS 2007. 29th Annual International Conference of the IEEE*, pages 5276 –5281, 22-26 2007.

[14] Y.M. Chi, P Ng, E Kang, J Kang, J Fang, and Gert Cauwenberghs. Wireless non-contact cardiac and brain monitoring. In *Wireless Health*, October 2010.

[15] Robert Matthews, Neil J. McDonald, Harini Anumula, Jamison Woodward, Peter J. Turner, Martin A. Steindorf, Kaichun Chang, and Joseph M. Pendleton. Novel hybrid bioelectrodes for ambulatory zero-prep eeg measurements using multi-channel wireless eeg system. In *FAC'07: Proceedings of the 3rd international conference on Foundations of augmented cognition*, pages 137–146, Berlin, Heidelberg, 2007. Springer-Verlag.

[16] L. Geddes and M. Valentinuzzi. Temporal changes in electrode impedance while recording the electrocardiogram with “dry” electrodes. *Annals of Biomedical Engineering*, 1:356–367, 1973. 10.1007/BF02407675.

[17] Emil Valchinov and Nicolas Pallikarakis. An active electrode for biopotential recording from small localized bio-sources. *BioMedical Engineering OnLine*, 3(1):25, 2004.

[18] G. Gargiulo, P. Bifulco, R.A. Calvo, M. Cesarelli, C. Jin, and A. van Schaik. Mobile biomedical sensing with dry electrodes. In *Intelligent Sensors, Sensor Networks and Information Processing, 2008. ISSNIP 2008. International Conference on*, pages 261 –266, 15-18 2008.

[19] M.A. Mestrovic, R.J.N. Helmer, L. Kyratzis, and D. Kumar. Preliminary study of dry knitted fabric electrodes for physiological monitoring. In *Intelligent Sensors, Sensor Networks and Information, 2007. ISSNIP 2007. 3rd International Conference on*, pages 601 –606, 3-6 2007.

[20] J. Yoo, Long Yan, Seulki Lee, Hyejung Kim, Binhee Kim, and Hoi-Jun Yoo. An attachable ecg sensor bandage with planar-fashionable circuit board. In *Wearable Computers, 2009. ISWC '09. International Symposium on*, pages 145 –146, 4-7 2009.

[21] M. Ishijima. Monitoring of electrocardiograms in bed without utilizing body surface electrodes. *Biomedical Engineering, IEEE Transactions on*, 40(6):593 –594, june 1993.

[22] Anna Gruetzmann, Stefan Hansen, and JâĹŽâĹĆrg MâĹŽÂžller. Novel dry electrodes for ecg monitoring. *Physiological Measurement*, 28(11):1375, 2007.

[23] P. Griss, P. Enoksson, H. Tolvanen-Laakso, P. Merilainen, S. Ollmar, and G. Stemme. Spiked biopotential electrodes. In *Micro Electro Mechanical Systems, 2000. MEMS 2000. The Thirteenth Annual International Conference on*, pages 323 –328, 23-27 2000.

[24] C.W. Chang and J.C. Chiou. Surface-mounted dry electrode and analog-front-end systems for physiological signal measurements. In *Life Science Systems and Applications Workshop, 2009. LiSSA 2009. IEEE/NIH*, pages 108 –111, 9-10 2009.

[25] Alan S. Gevins, Donald Durousseau, and Joel Libove. Dry electrode brain wave recording system, October 1990.

[26] Babak Alizadeh-Taheri, Rosemary L Smith, and Robert T Knight. An active, microfabricated, scalp electrode array for eeg recording. *Sensors and Actuators A: Physical*, 54(1-3):606 – 611, 1996.

[27] Yu.M. Chi and G. Cauwenberghs. Micropower non-contact eeg electrode with active common-mode noise suppression and input capacitance cancellation. In *Engineering in Medicine and Biology Society, 2009. EMBC 2009. Annual International Conference of the IEEE*, pages 4218 –4221, 3-6 2009.

[28] A. Ueno, Y. Akabane, T. Kato, H. Hoshino, S. Kataoka, and Y. Ishiyama. Capacitive sensing of electrocardiographic potential through cloth from the dorsal surface of the body in a supine position: A preliminary study. *Biomedical Engineering, IEEE Transactions on*, 54(4):759 –766, april 2007.

[29] A.J. Clippingdale, R. J. Clark, and C Watkins. Ultrahigh impedance capacitively coupled heart imaging array. *Review of Scientific Instruments*, 65(1):269–270, 1994.

[30] R J Prance, A Debray, T D Clark, H Prance, M Nock, C J Harland, and A J Clippingdale. An ultra-low-noise electrical-potential probe for human-body scanning. *Measurement Science and Technology*, 11(3):291, 2000.

[31] W. Gebrial, R. J. Prance, C. J. Harland, and T. D. Clark. Noninvasive imaging using an array of electric potential sensors. *Review of Scientific Instruments*, 77(6):063708, 2006.

[32] A. Saab and R. White. Achieve femtoampere leakage in surface-mount op-amp layouts. *Electronics Design, Strategy, News*, July 2008.

[33] C. Guld. Cathode follower and negative capacitance as high input impedance circuits. *Proceedings of the IRE*, 50(9):1912 –1927, sept. 1962.

[34] A. Aleksandrowicz and S. Leonhardt. Wireless and non-contact ECG measurement system– the Aachen SmartChair. *ActaPolytechnica*, 2:68–71, June 2007.

[35] Ko Keun Kim, Yong Kyu Lim, and Kwang Suk Park. The electrically noncontacting ecg measurement on the toilet seat using the capacitively-coupled insulated electrodes. In *Engineering in Medicine and Biology Society, 2004. IEMBS '04. 26th Annual International Conference of the IEEE*, volume 1, pages 2375 –2378, 1-5 2004.

[36] Ko Keun Kim and Kwang Suk Park. Effective coupling impedance for power line interference in capacitive-coupled ecg measurement system. In *Information Technology and Applications in Biomedicine, 2008. ITAB 2008. International Conference on*, pages 256 –258, 30-31 2008.

[37] Yu M. Chi and Gert Cauwenberghs. Wireless non-contact eeg/ecg electrodes for body sensor networks. In *Body Sensor Networks (BSN), 2010 International Conference on*, pages 297 –301, 7-9 2010.

[38] Yu.M. Chi, S.R. Deiss, and G. Cauwenberghs. Non-contact low power eeg/ecg electrode for high density wearable biopotential sensor networks. In *Wearable and Implantable Body Sensor Networks, 2009. BSN 2009. Sixth International Workshop on*, pages 246 –250, 3-5 2009.

[39] J. Ottenbacher and S. Heuer2. Motion artefacts in capacitively coupled ecg electrodes. *IFMBE Proceedings*, 25(4):1059–1062, 2009.

[40] S. Fuhrhop, S. Lamparth, and S. Heuer. A textile integrated long-term ecg monitor with capacitively coupled electrodes. In *Biomedical Circuits and Systems Conference, 2009. BioCAS 2009. IEEE*, pages 21 –24, 26-28 2009.

[41] M. Steffen, A. Aleksandrowicz, and S. Leonhardt. Mobile noncontact monitoring of heart and lung activity. *Biomedical Circuits and Systems, IEEE Transactions on*, 1(4):250 –257, dec. 2007.

[42] Ko Keun Kim, Yong Kyu Lim, and Kwang Suk Park. Common mode noise cancellation for electrically non-contact ecg measurement system on a chair. In *Engineering in Medicine and Biology Society, 2005. IEEE-EMBS 2005. 27th Annual International Conference of the*, pages 5881 –5883, 17-18 2005.

[43] T.J. Sullivan, S.R. Deiss, Tzyy-Ping Jung, and G. Cauwenberghs. A brain-machine interface using dry-contact, low-noise eeg sensors. In *Circuits and Systems, 2008. ISCAS 2008. IEEE International Symposium on*, pages 1986 –1989, 18-21 2008.

[44] Pai-Yuan Tsai, Weichih Hu, T.B.J. Kuo, and Liang-Yu Shyu. A portable device for real time drowsiness detection using novel active dry electrode system. In *Engineering in Medicine and Biology Society, 2009. EMBC 2009. Annual International Conference of the IEEE*, pages 3775 –3778, 3-6 2009.

[45] M.E. Griffith, W.M. Portnoy, L.J. Stotts, and J.L. Day. Improved capacitive electrocardiogram electrodes for burn applications. *Med Biol Eng Comput.*, 17(5):641 – 646, 1979.

[46] S. Bouwstra, L. Feijs, Wei Chen, and S.B. Oetomo. Smart jacket design for neonatal monitoring with wearable sensors. In *Wearable and Implantable Body Sensor Networks, 2009. BSN 2009. Sixth International Workshop on*, pages 162 –167, 3-5 2009.

[47] T. Kato, A. Ueno, S. Kataoka, H. Hoshino, and Y. Ishiyama. An application of capacitive electrode for detecting electrocardiogram of neonates and infants. In *Engineering in Medicine and Biology Society, 2006. EMBS '06. 28th Annual International Conference of the IEEE*, pages 916 –919, aug. 2006.

[48] J. Yoo, Long Yan, Seulki Lee, Hyejung Kim, and Hoi-Jun Yoo. A wearable ecg acquisition system with compact planar-fashionable circuit board-based shirt. *Information Technology in Biomedicine, IEEE Transactions on*, 13(6):897 –902, nov. 2009.

[49] J. Yoo, Long Yan, Seulki Lee, Yongsang Kim, and Hoi-Jun Yoo. A 5.2 mw self-configured wearable body sensor network controller and a 12 w wirelessly powered sensor for a continuous health monitoring system. *Solid-State Circuits, IEEE Journal of*, 45(1):178 –188, jan. 2010.

[50] M Oehler, V Ling, K Melhorn, and M Schilling. A multichannel portable ecg system with capacitive sensors. *Physiological Measurement*, 29(7):783, 2008.

[51] Yong Gyu Lim, Ko Keun Kim, and Suk Park. Ecg measurement on a chair without conductive contact. *Biomedical Engineering, IEEE Transactions on*, 53(5):956 –959, may 2006.

[52] Yong Kyu Lim, Ko Keun Kim, and Kwang Suk Park. The ecg measurement in the bathtub using the insulated electrodes. In *Engineering in Medicine and Biology Society, 2004. IEMBS '04. 26th Annual International Conference of the IEEE*, volume 1, pages 2383 –2385, 1-5 2004.

[53] R. J. Prance, S. T. Beardsmore-Rust, P. Watson, C. J. Harland, and H. Prance. Remote detection of human electrophysiological signals using electric potential sensors. *Applied Physics Letters*, 93(3):033906, 2008.

[54] G. Ruffini, S. Dunne, E. Farres, P.C.P. Watts, E. Mendoza, S.R.P. Silva, C. Grau, J. Marco-Pallares, L. Fuentemilla, and B. Vandecasteele. Enobio - first tests of a dry electrophysiology electrode using carbon nanotubes. In *Engineering in Medicine and Biology Society, 2006. EMBS '06. 28th Annual International Conference of the IEEE*, pages 1826 –1829, aug. 2006.

[55] Ju-Yeoul Baek, Jin-Hee An, Jong-Min Choi, Kwang-Suk Park, and Sang-Hoon Lee. Flexible polymeric dry electrodes for the long-term monitoring of ecg. *Sensors and Actuators A: Physical*, 143(2):423 – 429, 2008.

[56] B. Eilebrecht, M. Czaplik, M. Walter, T. Wartzek, R. Rossaint, and S. Leonhardt. Implementation of a capacitive ecg measurement system in clinical practice: an interim report. *World Congress on Medical Physics and Biomedical Engineering, September 7 - 12, 2009, Munich, Germany*, 25/7:370–372, 2009.

[57] Arjang Hassibi, Reza Navid, Robert W. Dutton, and Thomas H. Lee. Comprehensive study of noise processes in electrode electrolyte interfaces. *Journal of Applied Physics*, 96(2):1074–1082, 2004.

[58] B. Eggins. Skin-electrode impedance and its effect on recording cardiac potentials. *Analyst*, 118:439–442, 1993.

[59] Y.M. Chi, Tzyy-Ping Jung, and G. Cauwenberghs. Dry-contact and noncontact biopotential electrodes: Methodological review. *Biomedical Engineering, IEEE Reviews in*, 3:106 –119, 2010.

[60] R J Prance, T D Clark, H Prance, and A Clippingdale. Non-contact vlsi imaging using a scanning electric potential microscope. *Measurement Science and Technology*, 9(8):1229, 1998.

[61] Chulsung Park, P.H. Chou, Ying Bai, R. Matthews, and A. Hibbs. An ultra-wearable, wireless, low power ecg monitoring system. In *Biomedical Circuits and Systems Conference, 2006. BioCAS 2006. IEEE*, pages 241 –244, nov. 2006.

[62] T. Maruyama, M. Makikawa, N. Shiozawa, and Y. Fujiwara. Ecg measurement using capacitive coupling electrodes for man-machine emotional communication. In *Complex Medical Engineering, 2007. CME 2007. IEEE/ICME International Conference on*, pages 378 –383, 23-27 2007.

[63] J.M. Lee, F. Pearce, C. Morrissette, A.D. Hibbs, and R. Matthews. Evaluating a capacitively coupled, noncontact electrode for ecg monitoring. *Sensors Magazine*, 2005.

[64] A. Peper A.C. MettingVanRijn and C.A. Grimbergen. Amplifiers for bioelectric events: A design with a minimal number of parts. *Medical and Biological Engineering and Computing*, 1994.

[65] Bruce B. Winter and John G. Webster. Driven-right-leg circuit design. *Biomedical Engineering, IEEE Transactions on*, BME-30(1):62 –66, jan. 1983.

[66] Dirk Q. Feild, Charles L. Feldman, and B. Milan Hor[aacute][ccaron]ek. Improved easi coefficients: Their derivation, values, and performance. *Journal of Electrocardiology*, 35(4, Part 2):23 – 33, 2002.

[67] B. He and R.J. Cohen. Body surface laplacian ecg mapping. *Biomedical Engineering, IEEE Transactions on*, 39(11):1179 –1191, nov. 1992.

[68] Nils-Gunnar Holmer. An electrometer amplifier for electrophysiology with low input capacitance. *Medical and Biological Engineering and Computing*, 8:509–511, 1970. 10.1007/BF02477188.

[69] H. DeMan and W. Fluit. An integrated impedance converter for biomedical measurements. In *Solid-State Circuits Conference. Digest of Technical Papers. 1973 IEEE International*, volume XVI, pages 150 – 151, February 1973.

[70] Enrique Spinelli and Marcelo Haberman. Insulating electrodes: a review on biopotential front ends for dielectric skin–electrode interfaces. *Physiological Measurement*, 31(10):S183, 2010.

[71] Yu.M. Chi, C. Maier, and G. Cauwenberghs. An integrated, low-noise, high-input impedance front-end for non-contact bci and bsn physiological monitoring systems. In *IEEE CAS-FEST: The 2011 Forum on Emerging and Selected Topics*, 2011.

[72] T. Delbruck and C.A. Mead. Adaptive photoreceptor with wide dynamic range. In *Circuits and Systems, 1994. ISCAS '94., 1994 IEEE International Symposium on*, volume 4, pages 339 –342 vol.4, may-2 jun 1994.

[73] R.R. Harrison and C. Charles. A low-power low-noise cmos amplifier for neural recording applications. *Solid-State Circuits, IEEE Journal of*, 38(6):958 – 965, june 2003.

[74] D. Aebischer and H.J. Oguey. Cmos current reference without resistance. In *Solid-State Circuits, IEEE Journal of,*, volume 38, pages 958–965, 1997.

[75] T. Delbruck and A. Van Schaik. Bias current generators with wide dynamic range. In *Analog Integrated Circuits and Signal Processing*, volume 43, page 247:268, 2005.

[76] Texas Instruments. Ina116 datasheet.

[77] Martin Oehler, Peter Neumann, Matthias Becker, Gabriel Curio, and Meinhard Schilling. Extraction of ssvep signals of a capacitive eeg helmet for human machine interface. In *Engineering in Medicine and Biology Society, 2008. EMBS 2008. 30th Annual International Conference of the IEEE*, pages 4495 –4498, aug. 2008.

[78] Long Yan, Namjun Cho, J. Yoo, Binhee Kim, and Hoi-Jun Yoo. A two-electrode $2.88nJ/conversion$ biopotential acquisition system for portable healthcare device. In *Solid-State Circuits Conference, 2008. A-SSCC '08. IEEE Asian*, pages 329 –332, nov. 2008.

[79] M. Mollazadeh, K. Murari, G. Cauwenberghs, and N. Thakor. Micropower cmos integrated low-noise amplification, filtering, and digitization of multimodal neuropotentials. *Biomedical Circuits and Systems, IEEE Transactions on*, 3(1):1 –10, feb. 2009.

[80] J. Holleman and B. Otis. A sub-microwatt low-noise amplifier for neural recording. In *Engineering in Medicine and Biology Society, 2007. EMBS 2007. 29th Annual International Conference of the IEEE*, pages 3930 –3933, aug. 2007.

[81] R.F. Yazicioglu, P. Merken, R. Puers, and C. Van Hoof. A $60\mu W 60nV/Hz$ readout front-end for portable biopotential acquisition systems. In *Solid-State Circuits Conference, 2006. ISSCC 2006. Digest of Technical Papers. IEEE International*, pages 109 –118, feb. 2006.

[82] W. Wattanapanitch, M. Fee, and R. Sarpeshkar. An energy-efficient micropower neural recording amplifier. *Biomedical Circuits and Systems, IEEE Transactions on*, 1(2):136 –147, june 2007.

[83] R. R. Harrison, P. T. Watkins, R. J. Kier, R. O. Lovejoy, D. J. Black, B. Greger, and F. Solzbacher. A low-power integrated circuit for a wireless 100-electrode neural recording system. *Solid-State Circuits, IEEE Journal of*, 42(1):123 –133, jan. 2007.

[84] Texas Instruments. *ADS1298 8-Channel, 24-bit Analog-to-Digital Converter with Integrated ECG Front End Datasheet*. 2010.

[85] Du Chen, J.G. Harris, and J.C. Principe. A bio-amplifier with pulse output. In *Engineering in Medicine and Biology Society, 2004. IEMBS '04. 26th Annual International Conference of the IEEE*, volume 2, pages 4071 –4074, sept. 2004.

[86] G. Cauwenberghs and A. Yariv. Fault-tolerant dynamic multilevel storage in analog vlsi. *Circuits and Systems II: Analog and Digital Signal Processing, IEEE Transactions on*, 41(12):827 –829, dec 1994.

[87] R. Jacob Baker. *CMOS Circuit Design, Layout, and Simulation*. Wiley-IEEE Press, 1997.

[88] T.C. Caldwell and D.A. Johns. An incremental data converter with an oversampling ratio of 3. *Research in Microelectronics and Electronics 2006, Ph. D.*, pages 125 –128, 2006.

[89] M.L. Donaldson L.T. Kohn, J.M. Corrigan. To err is human. *Washington, DC: National Academy Press*, 2000.

[90] Institute of Medicin. Crossing the quality chasm: A new health crossing the quality chasm: A new health system for the 21st century. *Washington, DC: National Academy Press*, 2001.

[91] Agency for Healthcare Research and M Quality, Rockville. The hospital built environment: What role might funders of health services research play? *AHRQ Publication, no. 05-0106-EF*, 2005.

[92] E.A. Edelstein. Building health. *Health Environments Research and Design Journal*, 2008.

[93] E.A. Edelstein et al. Neural responses during navigation and wayfinding in the virtual aided design laboratory brain dynamics of re-orientation in architecturally ambiguous space. *SFB/TR 8 Report No. 015-05/2008*, 2008.

[94] T.A. DeFanti et al. The starcave, a third-generation cave and virtual reality optiportal. *Future Generation Computer Systems*, 25(2):169–178, 2009.

[95] Y.M. Chi and G. Cauwenberghs. Micropower non-contact eeg electrode with active common-mode noise suppression and input capacitance cancellation. In *Engineering in Medicine and Biology Society, 2009. EMBC 2009. Annual International Conference of the IEEE*, pages 4218 –4221, 3-6 2009.

[96] G. TrÂÍoste A. Bulling, D. Roggen. Wearable eog goggles: Seamless sensing and context-awareness in everyday environments. *J. Ambient Intelligence and Smart Environments*, 1(2):157–171, 2009.

[97] Yu-Te Wang, Yijun Wang, and Tzyy-Ping Jung. A cell-phone-based brain–computer interface for communication in daily life. *Journal of Neural Engineering*, 8(2):025018, 2011.

[98] U. Hoffmann, E.J. Fimbel, and T. Keller. Brain-computer interface based on high frequency steady-state visual evoked potentials: A feasibility study. In *Neural Engineering, 2009. NER '09. 4th International IEEE/EMBS Conference on*, pages 466 –469, 29 2009-may 2 2009.

[99] Wang Yijun, Wang Ruiping, Gao Xiaorong, and Gao Shangkai. Brain-computer interface based on the high-frequency steady-state visual evoked potential. In *Neural Interface and Control, 2005. Proceedings. 2005 First International Conference on*, pages 37 – 39, may 2005.

[100] Yijun Wang, Xiaorong Gao, Bo Hong, Chuan Jia, and Shangkai Gao. Brain-computer interfaces based on visual evoked potentials. *Engineering in Medicine and Biology Magazine, IEEE*, 27(5):64 –71, september-october 2008.

[101] Yijun Wang, Ruiping Wang, Xiaorong Gao, Bo Hong, and Shangkai Gao. A practical vep-based brain-computer interface. *Neural Systems and Rehabilitation Engineering, IEEE Transactions on*, 14(2):234 –240, june 2006.

[102] Guangyu Bin, Xiaorong Gao, Zheng Yan, Bo Hong, and Shangkai Gao. An online multi-channel ssvep-based brain–computer interface using a canonical correlation analysis method. *Journal of Neural Engineering*, 6(4):046002, 2009.

[103] G. Gargiulo, P. Bifulco, R.A. Calvo, M. Cesarelli, C. Jin, and A. van Schaik. A mobile eeg system with dry electrodes. In *Biomedical Circuits and Systems Conference, 2008. BioCAS 2008. IEEE*, pages 273 –276, nov. 2008.

[104] Jin-Chern Chiou, Li-Wei Ko, Chin-Teng Lin, Chao-Ting Hong, Tzyy-Ping Jung, Sheng-Fu Liang, and Jong-Liang Jeng. Using novel mems eeg sensors in detecting drowsiness application. In *Biomedical Circuits and Systems Conference, 2006. BioCAS 2006. IEEE*, pages 33 –36, nov. 2006.

[105] Lun-De Liao, P.C.-P. Chao, Yu-Han Chen, Chin-Teng Lin, Li-Wei Ko, Hsing-Hung Lin, and Wei-Hsuan Hsu. A novel hybrid bioelectrode module for the zero-prep eeg measurements. In *Sensors, 2009 IEEE*, pages 939 –942, oct. 2009.

[106] C.-T. Lin, L.-D. Liao, Y.-H. Liu, I.-J. Wang, B.-S. Lin, and J.-Y. Chang. Novel dry polymer foam electrodes for long-term eeg measurement. *Biomedical Engineering, IEEE Transactions on*, 58(5):1200 –1207, may 2011.

[107] Justin R. Estepp, James C. Christensen, Jason W. Monnin, Iris M. Davis, and Glenn F. Wilson. Validation of a Dry Electrode System for EEG. *Human Factors and Ergonomics Society Annual Meeting Proceedings*, pages 1171–1175, 2009.

[108] Thorsten Oliver Zander, Moritz Lehne, Klas Ihme, Sabine Jatzev, Joao Correia, Christian Kothe, Bernd Picht, and Femke Nijboer. A dry eeg-system for scientific research and brain-computer interfaces. In *Frontiers in Neuroscience*, 2011.

[109] C. J. Harland, T. D. Clark, and R. J. Prance. Remote detection of human electroencephalograms using ultrahigh input impedance electric potential sensors. *Applied Physics Letters*, 81(17):3284–3286, 2002.

[110] R. Puri, A. Majumdar, P. Ishwar, and K. Ramchandran. Distributed video coding in wireless sensor networks. *Signal Processing Magazine, IEEE*, 23(4):94 –106, july 2006.

[111] Wu-Chi Feng, Ed Kaiser, Wu Chang Feng, and Mikael Le Baillif. Panoptes: scalable low-power video sensor networking technologies. *ACM Trans. Multimedia Comput. Commun. Appl.*, 1:151–167, May 2005.

[112] Ashkan Olyaei and Roman Genov. Focal-plane spatially oversampling cmos image compression sensor. *Circuits and Systems I: Regular Papers, IEEE Transactions on*, 54(1):26 –34, jan. 2007.

[113] A. Bandyopadhyay, J. Lee, R. Robucci, and P. Hasler. A 80 mu;w/frame 104 times;128 cmos imager front end for jpeg compression. In *Circuits and Systems, 2005. ISCAS 2005. IEEE International Symposium on*, pages 5318 – 5321 Vol. 5, may 2005.

[114] Qiang Luo and J.G. Harris. A novel integration of on-sensor wavelet compression for a cmos imager. In *Circuits and Systems, 2002. ISCAS 2002. IEEE International Symposium on*, volume 3, pages III–325 – III–328 vol.3, 2002.

[115] W.D. Leon-Salas, S. Balkir, K. Sayood, N. Schemm, and M.W. Hoffman. A cmos imager with focal plane compression using predictive coding. *Solid-State Circuits, IEEE Journal of*, 42(11):2555 –2572, nov. 2007.

[116] S. Kawahito, M. Yoshida, M. Sasaki, K. Umehara, D. Miyazaki, Y. Tadokoro, K. Murata, S. Doushou, and A. Matsuzawa. A cmos image sensor with analog two-dimensional dct-based compression circuits for one-chip cameras. *Solid-State Circuits, IEEE Journal of*, 32(12):2030 –2041, dec 1997.

[117] Y.M. Chi, U. Mallik, M.A. Clapp, E. Choi, G. Cauwenberghs, and R. Etienne-Cummings. Cmos camera with in-pixel temporal change detection and adc. *Solid-State Circuits, IEEE Journal of*, 42(10):2187 –2196, oct. 2007.

[118] Y.M. Chi, R. Etienne-Cummings, G. Cauwenberghs, P. Carpenter, and K. Colling. Video sensor node for low-power ad-hoc wireless networks. In *Information Sciences and Systems, 2007. CISS '07. 41st Annual Conference on*, pages 244 –247, march 2007.

[119] Yu.M. Chi, R. Elienne-Cummings, and G. Cauwenherghs. Image sensor with focal plane change event driven video compression. In *Circuits and Systems, 2008. ISCAS 2008. IEEE International Symposium on*, pages 1862 –1865, may 2008.

[120] Yi-Jen Chin and T. Berger. A software-only videocodec using pixelwise conditional differential replenishment and perceptual enhancements. *Circuits and Systems for Video Technology, IEEE Transactions on*, 9(3):438 –450, apr 1999.

[121] *Digital Video Processing*. Prentice Hall Signal Processing Series, 1995.

[122] Jie Liang and T.D. Tran. Fast multiplierless approximations of the dct with the lifting scheme. *Signal Processing, IEEE Transactions on*, 49(12):3032 –3044, dec 2001.

[123] Mikhail Vorontsov, Jim Riker, Gary Carhart, V. S. Rao Gudimetla, Leonid Beresnev, Thomas Weyrauch, and Jr. Lewis C. Roberts. Deep turbulence effects compensation experiments with a cascaded adaptive optics system using a 3.63 m telescope. *Appl. Opt.*, 48(1):A47–A57, Jan 2009.

[124] M. A. Vorontsov, G. W. Carhart, and J. C. Ricklin. Adaptive phase-distortion correction based on parallel gradient-descent optimization. *Opt. Lett.*, 22(12):907–909, Jun 1997.

[125] M. Cohen, G. Cauwenberghs, and M.A. Vorontsov. Image sharpness and beam focus vlsi sensors for adaptive optics. *Sensors Journal, IEEE*, 2(6):680 – 690, dec 2002.

[126] S.K. Mendis, S.E. Kemeny, R.C. Gee, B. Pain, C.O. Staller, Quiesup Kim, and E.R. Fossum. Cmos active pixel image sensors for highly integrated imaging systems. *Solid-State Circuits, IEEE Journal of*, 32(2):187 –197, feb 1997.

[127] Yang Ni, F. Devos, M. Boujrad, and Jian Hong Guan. Histogram-equalization-based adaptive image sensor for real-time vision. *Solid-State Circuits, IEEE Journal of*, 32(7):1027 –1036, jul 1997.

[128] T. Sugiki, S. Ohsawa, H. Miura, M. Sasaki, N. Nakamura, I. Inoue, M. Hoshino, Y. Tomizawa, and T. Arakawa. A 60 mw 10 b cmos image sensor with column-to-column fpn reduction. In *Solid-State Circuits Conference, 2000. Digest of Technical Papers. ISSCC. 2000 IEEE International*, pages 108 –109, 450, 2000.

[129] M.F. Snoeij, A.J.P. Theuwissen, K.A.A. Makinwa, and J.H. Huijsing. Multiple-ramp column-parallel adc architectures for cmos image sensors. *Solid-State Circuits, IEEE Journal of*, 42(12):2968 –2977, dec. 2007.

[130] Eugenio Culurciello and Andreas G. Andreou. Cmos image sensors for sensor networks. *Analog Integr. Circuits Signal Process.*, 49:39–51, October 2006.

[131] P. Lichtsteiner, C. Posch, and T. Delbruck. A 128 x 128 120db 15us latency asynchronous temporal contrast vision sensor. *Solid-State Circuits, IEEE Journal of*, 43(2):566 –576, feb. 2008.

[132] V. Gruev and R. Etienne-Cummings. A pipelined temporal difference imager. In *Circuits and Systems, 2002. ISCAS 2002. IEEE International Symposium on*, volume 3, pages 683 –686, 2002.

[133] S.K. Mendis, S.E. Kemeny, R.C. Gee, B. Pain, C.O. Staller, Quiesup Kim, and E.R. Fossum. Cmos active pixel image sensors for highly integrated imaging systems. *Solid-State Circuits, IEEE Journal of*, 32(2):187 –197, feb 1997.

[134] Turicchia L et al. A low-power imager and compression algorithms for a brain-machine visual prosthesis for the blind. *Proceedings of SPIE BiOS*, 2009.

[135] Emily S. Kappenman and Steven J. Luck. The effects of electrode impedance on data quality and statistical significance in erp recordings. *Psychophysiology*, 47(5):888–904, 2010.

[136] Jonathan R. Wolpaw, Niels Birbaumer, Dennis J. McFarland, Gert Pfurtscheller, and Theresa M. Vaughan. Brain-computer interfaces for communication and control. *Clinical Neurophysiology*, 113(6):767 – 791, 2002.

[137] An Luo and Thomas J Sullivan. A user-friendly ssvep-based brain–computer interface using a time-domain classifier. *Journal of Neural Engineering*, 7(2):026010, 2010.

[138] Chin-Teng Lin, Li-Wei Ko, Jin-Chern Chiou, Jeng-Ren Duann, Ruey-Song Huang, Sheng-Fu Liang, Tzai-Wen Chiu, and Tzyy-Ping Jung. Noninvasive neural prostheses using mobile and wireless eeg. *Proceedings of the IEEE*, 96(7):1167 –1183, july 2008.

[139] Yu M. Chi, Patrick Ng, Eric Kang, Joseph Kang, Jennifer Fang, and Gert Cauwenberghs. Wireless non-contact cardiac and neural monitoring. In *Wireless Health 2010*, WH '10, pages 15–23, New York, NY, USA, 2010. ACM.

[140] G. Ruffini, S. Dunne, E. Farres, I. Cester, P.C.P. Watts, S. Ravi, P. Silva, C. Grau, L. Fuentemilla, J. Marco-Pallares, and B. Vandecasteele. Enobio dry electrophysiology electrode; first human trial plus wireless electrode system. In *Engineering in Medicine and Biology Society, 2007. EMBS 2007. 29th Annual International Conference of the IEEE*, pages 6689 –6693, 22-26 2007.

[141] P. Griss, H.K. Tolvanen-Laakso, P. Merilainen, and G. Stemme. Characterization of micromachined spiked biopotential electrodes. *Biomedical Engineering, IEEE Transactions on*, 49(6):597 –604, june 2002.

[142] Ming Yin and M. Ghovanloo. A low-noise preamplifier with adjustable gain and bandwidth for biopotential recording applications. In *Circuits and Systems, 2007. ISCAS 2007. IEEE International Symposium on*, pages 321 –324, may 2007.

[143] Xiaoyuan Xu, Xiaodan Zou, Libin Yao, and Yong Lian. A 1-v 450-nw fully integrated biomedical sensor interface system. In *VLSI Circuits, 2008 IEEE Symposium on*, pages 78 –79, 18-20 2008.

[144] B. Gosselin, A.E. Ayoub, J.-F. Roy, M. Sawan, F. Lepore, A. Chaudhuri, and D. Guitton. A mixed-signal multichip neural recording interface with bandwidth reduction. *Biomedical Circuits and Systems, IEEE Transactions on*, 3(3):129 –141, june 2009.

[145] C J Harland, T D Clark, N S Peters, M J Everitt, and P B Stiffell. A compact electric potential sensor array for the acquisition and reconstruction of the 7-lead

electrocardiogram without electrical charge contact with the skin. *Physiological Measurement*, 26(6):939, 2005.

[146] K.-i. Yamakoshi. In the spotlight: Bioinstrumentation. *Biomedical Engineering, IEEE Reviews in*, 2:2 –5, 2009.

[147] J. Rosell, J. Colominas, P. Riu, R. Pallas-Areny, and J.G. Webster. Skin impedance from 1 hz to 1 mhz. *Biomedical Engineering, IEEE Transactions on*, 35(8):649 –651, aug. 1988.

[148] Hans J Scheer, Tilmann Sander, and Lutz Trahms. The influence of amplifier, interface and biological noise on signal quality in high-resolution eeg recordings. *Physiological Measurement*, 27(2):109, 2006.

[149] M. Puurtinen, J. Viik, and J. Hyttinen. Best electrode locations for a small bipolar ecg device: Signal strength analysis of clinical data. *ANNALS OF BIOMEDICAL ENGINEERING*, 37(2):331–336, 2009.

[150] Thomas C Ferree, Phan Luu, Gerald S Russell, and Don M Tucker. Scalp electrode impedance, infection risk, and eeg data quality. *Clinical neurophysiology : official journal of the International Federation of Clinical Neurophysiology*, 112(3):536–544, 03 2001/03/01.

[151] J. Muhlsteff, O. Such, R. Schmidt, M. Perkuhn, H. Reiter, J. Lauter, J. Thijs, G. Musch, and M. Harris. Wearable approach for continuous ecg - and activity patient-monitoring. In *Engineering in Medicine and Biology Society, 2004. IEMBS '04. 26th Annual International Conference of the IEEE*, volume 1, pages 2184 –2187, 1-5 2004.

[152] P. Fiedler, S. Bordkorb, C. Fonseca, F. Vaz, F. Zanow, and J. Haueisen. Novel TiN-based dry eeg electrodes; influence of electrode shape and number on contact impedance and signal quality. In *IFMBE Proceedings*, volume 29, pages 418–421, May 2010.

[153] P. Tallgren, S. Vanhatalo, K. Kaila, and J. Voipio. Evaluation of commercially available electrodes and gels for recording of slow eeg potentials. *Clinical Neurophysiology*, 116(4):799 – 806, 2005.

[154] C. Fonseca, J.P.S. Cunha, R.E. Martins, V.M. Ferreira, J.P.M. de Sa, M.A. Barbosa, and A.M. da Silva. A novel dry active electrode for eeg recording. *Biomedical Engineering, IEEE Transactions on*, 54(1):162 –165, jan. 2007.

[155] C. Assambo and M.J. Burke. Amplifier input impedance in dry electrode ecg recording. In *Engineering in Medicine and Biology Society, 2009. EMBC 2009. Annual International Conference of the IEEE*, pages 1774 –1777, 3-6 2009.

[156] K.-P. Hoffmann and R. Ruff. Flexible dry surface-electrodes for ecg long-term monitoring. In *Engineering in Medicine and Biology Society, 2007. EMBS 2007. 29th Annual International Conference of the IEEE*, pages 5739 –5742, 22-26 2007.

[157] N. Verma, A. Shoeb, J. Bohorquez, J. Dawson, J. Guttag, and A.P. Chandrakasan. A micro-power eeg acquisition soc with integrated feature extraction processor for a chronic seizure detection system. *Solid-State Circuits, IEEE Journal of*, 45(4):804 –816, april 2010.

[158] Ottenbacher, L. Jatoba, U. Großmann, W. Stork, and K. Müller-Glaser. Ecg electrodes for a context-aware cardiac permanent monitoring system. *IFMBE Proceedings*, 14(7):672–675, 2007.

[159] L. Fay, V. Misra, and R. Sarpeshkar. A micropower electrocardiogram amplifier. *Biomedical Circuits and Systems, IEEE Transactions on*, 3(5):312 –320, oct. 2009.